AD-A256 019

‖‖‖‖‖‖‖‖‖‖‖‖‖‖‖‖

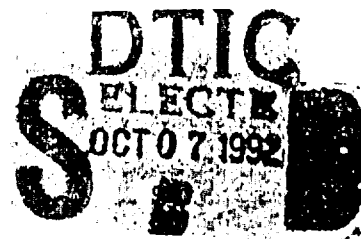## Quarterly Technical Report

Solid State Research

1991:4

Lincoln Laboratory

MASSACHUSETTS INSTITUTE OF TECHNOLOGY

LEXINGTON, MASSACHUSETTS

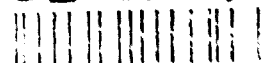92 10 6 013

92-26525

‖‖‖‖‖‖‖‖‖‖‖‖‖‖

The ESD Public Affairs Office has reviewed this report, and it is releasable to the National Technical Information Service, where it will be available to the general public, including foreign nationals.

This technical report has been reviewed and is approved for publication.

FOR THE COMMANDER

Hugh L. Southall

Hugh L. Southall, Lt. Col., USAF
Chief, ESD Lincoln Laboratory Project Office

MASSACHUSETTS INSTITUTE OF TECHNOLOGY
LINCOLN LABORATORY

SOLID STATE RESEARCH

QUARTERLY TECHNICAL REPORT

1 AUGUST — 31 OCTOBER 1991

ISSUED 28 MAY 1992

LEXINGTON   MASSACHUSETTS

ABSTRACT

This report covers in detail the research work of the Solid State Division at Lincoln Laboratory for the period 1 August through 31 October 1991. The topics covered are Electrooptical Devices, Quantum Electronics, Materials Research, Submicrometer Technology, High Speed Electronics, Microelectronics, and Analog Device Technology. Funding is provided primarily by the Air Force, with additional support provided by the Army, DARPA, Navy, SDIO, NASA, and DOE.

iii

Accession For		
NTIS GRA&I	☑	
DTIC TAB	☐	
Unannounced	☐	
Justification		
By		
Distribution/		
Availability Codes		
Dist	Avail and/or Special	
A-1		

TABLE OF CONTENTS

LIST OF ILLUSTRATIONS

LIST OF ILLUSTRATIONS (Continued)

ix

LIST OF ILLUSTRATIONS (Continued)

LIST OF ILLUSTRATIONS (Continued)

LIST OF TABLES

INTRODUCTION

1. ELECTROOPTICAL DEVICES

A tapered amplifier using strained-layer InGaAs/AlGaAs material in a master-oscillator/power-amplifier configuration has been demonstrated. This device is capable of high-power CW operation at a wavelength suitable for pumping erbium-doped fiber amplifiers and lasers.

Two-dimensional arrays of surface-emitting AlGaAs diode lasers with etched facets and external parabolic deflecting mirrors have been fabricated. Threshold current densities as low as 230 A/cm^2, comparable to broad-area lasers in the same material, and differential quantum efficiencies as high as 56% have been obtained in small arrays, representing a significant improvement in performance.

Organometallic vapor phase epitaxy (OMVPE) growth of GaInAsP alloys as confinement layers in a GaAs-based structure with GaInP cladding and an InGaAs strained-layer quantum well has been successfully demonstrated for the first time. High-quality structures have been obtained, as determined by surface morphology and by x-ray and photoluminescence characterization.

2. QUANTUM ELECTRONICS

A 640-μm-long 1.064-μm microchip laser has been operated CW at output powers up to 2 W, with nearly diffraction-limited performance up to 1 W. The output power of the device was limited by thermally induced optical aberrations.

A Nd:YAG microchip laser has been electrooptically Q switched to produce a train of 1.064-μm single-frequency pulses with a full width at half-maximum of < 2 ns, at repetition rates up to 140 kHz. These pulses were frequency doubled to produce 4 mW of green radiation.

Arrays of microchip lasers with one curved mirror and one flat mirror have been characterized by comparison with conventional arrays having two flat mirrors. The use of a curved mirror relaxes the tolerance on mirror misalignment, allows the use of a gain medium having a decrease in optical length with increasing temperature, reduces the radius of the oscillating mode, and lowers the threshold of the laser.

Active mode locking of a Yb:YAG laser has been used to generate 80-ps pulses in a spectral bandwidth of 7 GHz. The laser cavity without an acoustooptic mode locker generated 1.56 W of output power with 2.9 W of incident power.

A pumping model of Q-switched Yb:YAG lasers has been developed to show that the optical efficiency should be comparable to that of diode-pumped Nd:YAG lasers. The model gives design rules that relate the pump intensity, the length of the gain medium, and the net pump quantum efficiency.

Samples of Yb:YAG (6.5 at.% Yb) doped with 0.1 to 2 at.% erbium were evaluated for potential InGaAs-diode-pumped laser operation at 1.64 μm. The net Yb-Er transfer efficiency was found to be high, but strong upconversion due to Er-Er and Yb-Er interactions was observed.

The stresses resulting from Gaussian volumetric heat deposition in a disk geo. . y have been determined analytically. It has been found that the maximum stress at the edge of the disk differs from the stress resulting from uniform heat deposition by, at most, a factor of 2.

Improvements in a rotating-disk Nd:glass laser have resulted in nearly 2 W of output in a TEM_{00} mode, with 5.2 W of absorbed pump power from a $Ti:Al_2O_3$ laser. The slope efficiency was 47%, and the laser performance was limited only by the available pump power.

3.   MATERIALS RESEARCH

Diode lasers emitting at 4.0 μm have been fabricated from lattice-matched $InAs_{0.91}Sb_{0.09}$/ $AlAs_{0.08}Sb_{0.92}$ double heterostructures grown by molecular beam epitaxy on GaSb substrates. These devices, which have exhibited CW operation up to 80 K and pulsed operation up to 155 K, have the longest emission wavelength reported for III-V semiconductor diode lasers.

With the objective of developing an improved process for in situ etching of GaAs-based materials in OMVPE reactors, GaAs wafers and $Al_xGa_{1-x}As$ epilayers with x up to 0.7 have been etched with CH_3I vapor in a horizontal reactor operated at atmospheric pressure with H_2 or He carrier gas. Specular surfaces are maintained at temperatures below 500°C for etch depths up to 5000 Å, and the etch rate does not depend on Al content.

4.   SUBMICROMETER TECHNOLOGY

High-purity GaAs has been grown from arsine and elemental gallium in a gas-source molecular beam epitaxy system. An analysis of the dependence of GaAs purity on arsine pyrolysis temperature and a comparison with elemental arsenic growth have been made using Hall effect and photoluminescence measurements.

Improvements have been made in laser-direct-write techniques for modifying interconnect metallization in the repair of digital integrated circuits. A platinum deposition procedure has been developed, and an excimer laser has been added to the apparatus to increase the yield and reliability of the modifications.

5.   HIGH SPEED ELECTRONICS

GaAs/AlGaAs quantum wells have been successfully grown over 10-nm-thick epitaxial CoAl layers by molecular beam epitaxy and characterized with transmission electron microscopy and photoluminescence. This preliminary work indicates the feasibility of growing epitaxial quantum wells over a CoAl layer, which may lead to a variety of unique electrooptical devices incorporating buried optical mirrors, Schottky barriers, and/or ohmic electrical contacts.

6.   MICROELECTRONICS

An image processor based on a charge-coupled device (CCD) has been designed, fabricated, and tested. The device, which can be used for spatial filtering or implementation of local-connectivity neural networks, performs one billion computations per second and dissipates < 1 W when clocked at 10 MHz.

An electronic shutter integrated into a CCD has been electrically and optically characterized under back-illuminated operating conditions. Measurements show that the shuttered devices have extinction ratios $> 10^4$ at wavelengths < 540 nm and have switching times < 55 ns.

The charge-transfer inefficiency (CTI) in a buried-channel CCD imager has been measured over the temperature range from 100 to 220 K before and after proton irradiation of 20 krad at 40 MeV. The data show that the combination of a potential trough in the center of the channel and an operating temperature near 150 K minimizes the increase in CTI after irradiation, and indicate that good low-signal performance can be maintained for well over 10 years in a 900-km orbit.

7. ANALOG DEVICE TECHNOLOGY

Measurements have been made of the surface impedance Z_s of $YBa_2Cu_3O_{7-x}$ thin films using a stripline resonator. Values of Z_s were obtained as a function of frequency from 1.5 to 20 GHz, as a function of temperature from 4 K to the transition temperature ~ 90 K, and as a function of the RF magnetic field from 0 to 300 Oe.

A generic fabrication process has been developed for low-temperature superconductive integrated circuits that include both analog and digital components. The process supports a wide range of electrical components—Josephson junctions, resistors, high-Q capacitors, inductors, transformers, and delay lines—with characteristics that are well documented and highly controlled over a wafer.

REPORTS ON SOLID STATE RESEARCH

1 AUGUST THROUGH 31 OCTOBER 1991

PUBLICATIONS

A CCD Programmable Image Processor and Its Neural Network Applications	A. M. Chiang M. L. Chuang	*IEEE J. Solid-State Circuits* **26**, 1894 (1991)
Room-Temperature CW Operation at 2.2 μm of GaInAsSb/AlGaAsSb Diode Lasers Grown by Molecular Beam Epitaxy	H. K. Choi S. J. Eglash	*Appl. Phys. Lett.* **59**, 1165 (1991)
High-Efficiency High-Power GaInAsSb-AlGaAsSb Double-Heterostructure Lasers Emitting at 2.3 μm	H. K. Choi S. J. Eglash	*IEEE J. Quantum Electron.* **27**, 1555 (1991)
High-Power, High-Temperature Operation of AlInGaAs-AlGaAs Strained Single-Quantum-Well Diode Lasers	H. K. Choi C. A. Wang D. F. Kolesar R. L. Aggarwal J. N. Walpole	*IEEE Photon. Technol. Lett.* **3**, 857 (1991)
Operation of Five Individual Diode Lasers as a Coherent Ensemble by Fiber Coupling into an External Cavity	C. J. Corcoran R. H. Rediker	*Appl. Phys. Lett.* **59**, 759 (1991)
Single-Axial Mode, Intracavity Doubled Nd:YAG Laser	T. Y. Fan	*IEEE J. Quantum Electron.* **27**, 2091 (1991)
Power Scaling of End-Pumped Lasers by Geometric Multiplexing	T. Y. Fan W. E. DeFeo	*OSA Proc. Advanced Solid-State Lasers* **6**, 34 (1991)
Diamond Cold Cathode	M. W. Geis N. N. Efremow J. D. Woodhouse M. D. McAleese M. Marchywka* D. G. Socker* J. F. Hochedez*	*IEEE Electron Device Lett.* **12**, 456 (1991)

---

*Author not at Lincoln Laboratory.

Diode-Pumped, Self-Starting Additive-Pulse Mode-Locked Nd:YAG and Nd:YLF Lasers	J. Goodberlet* J. Jacobson* J. G. Fujimoto* P. A. Schulz T. Y. Fan	*OSA Proc. Advanced Solid-State Lasers* **6**, 37 (1991)
Monolithic Two-Dimensional Surface-Emitting Strained-Layer InGaAs/AlGaAs and AlInGaAs/ AlGaAs Diode Laser Arrays with over 50% Differential Quantum Efficiencies	W. D. Goodhue J. P. Donnelly C. A. Wang G. A. Lincoln K. Rauschenbach R. J. Bailey G. D. Johnson	*Appl. Phys. Lett.* **59**, 632 (1991)
5-GHz Mode Locking of a Nd:YLF Laser	P. A. Schulz S. R. Henion	*Opt. Lett.* **16**, 1502 (1991)
Development of a Mesospheric Sodium Laser Beacon for Atmospheric Adaptive Optics	T. H. Jeys	*Lincoln Lab. J.* **4**, 133 (1991)
Photo-oxidation of σ-conjugated Si-Si Network Polymers	R. R. Kunz M. W. Horn P. A. Bianconi* D. A. Smith* C. A. Freed*	*J. Vac. Sci. Technol. A* **9**, 1447 (1991)
Laser Pumping of Solid-State Amplifiers Using Random Binary-Phase Plates	P. Lacovara K. F. Wall R. L. Aggarwal M. W. Geis K. Krohn	*OSA Proc. Advanced Solid-State Lasers* **6**, 106 (1991)
Optical Phase Difference Measurement and Correction Using AlGaAs Integrated Guided-Wave Components	S. D. Lau J. P. Donnelly C. A. Wang R. B. Goodman R. H. Rediker	*IEEE Photon. Technol. Lett.* **3**, 902 (1991)

*Author not at Lincoln Laboratory.

High-Temperature Superconductive Passive Microwave Devices	W. G. Lyons R. S. Withers J. M. Hamm A. C. Anderson P. M. Mankiewich* M. L. O'Malley* R. E. Howard* R. R. Bonetti* A. E. Williams* N. Newman*	*1991 IEEE MTT-S Int. Microwave Symp. Dig.* (IEEE, New York, 1991), Vol. 3, p. 1227
High-T_c Microstrip Filters and Delay Lines	W. G. Lyons R. S. Withers	In *Superconducting Technology*, K. Fossheim, ed. (World Scientific, Teaneck, N.J., 1991), p. 113
Surface Impedance Measurements of $YBa_2Cu_3O_{7-x}$ Thin Films in Stripline Resonators	D. E. Oates A. C. Anderson	*Advances in Superconductivity III: Proc. 3rd Int. Symp. on Superconductivity*, K. Kajimura and H. Hayakawa, eds. (Springer-Verlag, Tokyo, 1991), p. 1149
Stripline Resonator Measurements of Z_S versus H_{rf} in $YBa_2Cu_3O_{7-x}$ Thin Films	D. E. Oates A. C. Anderson D. M. Sheen* S. M. Ali*	*IEEE Trans. Microwave Theory Tech.* **39**, 1522 (1991)
Superconducting Thin-Film $YBa_2Cu_3O_{7-x}$ Resonators and Filters	D. E. Oates W. G. Lyons A. C. Anderson	*Proc. 45th Annual Symp. on Frequency Control* (IEEE, New York, 1991), p. 460
Excimer-Laser-Induced Sub-0.5-μm Patterning of WO_3 Thin Films	M. Rothschild A. R. Forte	*Appl. Phys. Lett.* **59**, 1790 (1991)
Current Distribution in Superconducting Strip Transmission Lines	D. M. Sheen* S. M. Ali* D. E. Oates R. S. Withers J. A. Kong*	*1991 IEEE MTT-S Int. Microwave Symp. Dig.* (IEEE, New York, 1991), Vol. 1, p. 161

---

*Author not at Lincoln Laboratory.

Through-Wafer Optical Communication Using Monolithic InGaAs-on-Si LED's and Monolithic PtSi-Si Schottky-Barrier Detectors	G. W. Turner C. K. Chen B-Y. Tsaur A. M. Waxman	*IEEE Photon. Technol. Lett.* **3**, 761 (1991)
A Ti:Al$_2$O$_3$ Master-Oscillator Power-Amplifier System	K. F. Wall R. L. Aggarwal P. A. Schulz P. Lacovara V. Daneu A. Walther A. Sanchez	*OSA Proc. Advanced Solid-State Lasers* **6**, 121 (1991)
Optimization of Q-Switched Lasers	J. J. Zayhowski P. L. Kelley	*IEEE J. Quantum Electron.* **27**, 2220 (1991)
Thermal Guiding in Microchip Lasers	J. J. Zayhowski	*OSA Proc. Advanced Solid-State Lasers* **6**, 9 (1991)

ACCEPTED FOR PUBLICATION

A Quasioptically Stabilized Resonant-Tunneling-Diode Oscillator for the Millimeter- and Submillimeter-Wave Regions	E. R. Brown C. D. Parker K. M. Molvar K. D. Stephan*	*IEEE Trans. Microwave Theory Tech.*
GaAs-Based Diode Lasers on Si with Increased Lifetime Obtained by Using Strained InGaAs Active Layer	H. K. Choi C. A. Wang N. H. Karam*	*Appl. Phys. Lett.*
Electrical and Structural Characterization of GaAs Vertical-Sidewall Epilayers Grown by Atomic Layer Epitaxy	D. B. Gladden W. D. Goodhue C. A. Wang G. A. Lincoln	*J. Electron. Mater.*
Low-Threshold InGaAs Strained-Layer Quantum-Well Lasers (λ = 0.98 μm) with GaInP Cladding Layers and Mass-Transported Buried Heterostructure	Z. L. Liau S. C. Palmateer S. H. Groves J. N. Walpole L. J. Missaggia	*Appl. Phys. Lett.*

*Author not at Lincoln Laboratory.

PRESENTATIONS[†]

Device Applications and Characterization of Low-Temperature GaAs Grown by Molecular Beam Epitaxy	F. W. Smith A. R. Calawa	IEEE/Cornell Conference, Ithaca, New York, 5-7 August 1991
High Speed Quantum-Flux-Parametron-Based Analog-to-Digital Converters	Y. Harada* J. B. Green	University of California at Berkeley–Research and Development Corporation of Japan Joint Symposium, Berkeley, California, 15-16 August 1991
New Photoresist Processes at UV Wavelengths Less Than 200 nm	D. J. Ehrlich R. R. Kunz M. A. Hartney M. W. Horn J. Melngailis	Radiation Effects on Polymer Materials, Stanford, California, 18-23 August 1991
Effects of Thermal Noise on the Operation of Superconductive Integrated Circuits	J. B. Green	MIT–Research and Development Corporation of Japan Joint Symposium, Cambridge, Massachusetts, 19-20 August 1991
A Quantum-Flux-Parametron-Based Analog-to-Digital Converter with 18-GHz Sampling Rate and 5-GHz Bandwidth	Y. Harada* J. B. Green	
Sub-0.25-μm Resolution Using 193-nm Optical Lithography	M. A. Hartney M. W. Horn R. R. Kunz M. Rothschild D. C. Shaver	IEEE Lithography Workshop, Kauai, Hawaii, 19-23 August 1991
Diamond Transistors	M. W. Geis N. N. Efremow J. D. Woodhouse M. D. McAleese	Applied Diamond Conference '91, Auburn, Alabama, 20-22 August 1991
Device-Quality Diamond Substrates	M. W. Geis	Second European Conference on Diamond, Diamond-Like and Related Coatings, Nice, France, 2-6 September 1991

---

*Author not at Lincoln Laboratory.

[†]Titles of presentations are listed for information only. No copies are available for distribution.

Long-Wavelength Ge$_x$Si$_{1-x}$/Si Heterojunction Infrared Detectors and Focal Plane Arrays	B-Y. Tsaur	Seminar, Raytheon Research Center, Lexington, Massachusetts, 18 September 1991
High-Temperature Superconductive Delay Lines and Filters	W. G. Lyons R. S. Withers J. M. Hamm A. C. Anderson D. E. Oates P. M. Mankiewich* M. L. O'Malley* R. R. Bonetti* A. E. Williams* N. Newman*	Conference on Superconductivity and Applications, Buffalo, New York, 24-26 September 1991
Optical Lithography at Feature Sizes of 0.25 μm and Below	M. A. Hartney M. W. Horn R. R. Kunz M. Rothschild D. C. Shaver	Lincoln Laboratory Technical Seminar Series, Pennsylvania State University, University Park, Pennsylvania, 27 September 1991; University of Illinois, Champaign-Urbana, Illinois, 23 October 1991
Optical Interconnections for Digital Systems	D. Z. Tsang	Lincoln Laboratory Technical Seminar Series, University of Illinois, Champaign-Urbana, Illinois, 2 October 1991; Carnegie-Mellon University, Pittsburgh, Pennsylvania, 10 October 1991
Vertical Gradient-Freeze Growth of Rare Earth Orthoaluminate Crystals to Provide Substrates for High-Temperature Superconducting Films	R. E. Fahey A. J. Strauss A. C. Anderson	Fourth Conference on Crystal Growth, Atlantic City, New Jersey, 2-4 October 1991
Non-linear Microwave Electrodynamics of NbN and Nb Thin Films	C. C. Chin* D. E. Oates A. C. Anderson G. Dresselhaus*	International Symposium on Superconductivity, Tokyo, Japan 14-17 October 1991

*Author not at Lincoln Laboratory.

ORGANIZATION

SOLID STATE DIVISION

A. L. McWhorter, *Head*
I. Melngailis, *Associate Head*
E. Stern, *Associate Head*
D. C. Shaver, *Assistant Head*
J. F. Goodwin, *Assistant*

D. J. Ehrlich, *Senior Staff*
N. L. DeMeo, Jr., *Associate Staff*
J. W. Caunt, *Assistant Staff*
K. J. Challberg, *Administrative Staff*

SUBMICROMETER TECHNOLOGY

M. Rothschild, *Leader*
T. M. Lyszczarz, *Assistant Leader*

Astolfi, D. K.	Goodman, R. B.
Craig, D. M.	Hartney, M. A.
Dennis, C. L.	Horn, M. W.
DiNatale, W. F.	Kunz, R. R.
Doran, S. P.	Maki, P. A.
Efremow, N. N., Jr.	Melngailis, J.[†]
Forte, A. R.	Sedlacek, J. H. C.
Gajar, S. A.*	Uttaro, R. S.
Geis, M. W.	

QUANTUM ELECTRONICS

A. Mooradian, *Leader*
P. L. Kelley, *Associate Leader*
A. Sanchez-Rubio, *Assistant Leader*

Aggarwal, R. L.	Hsu, L.*
Barch, W. E.	Jeys, T. H.
Cook, C. C.	Korn, J. A.
Daneu, V.	Lacovara, P.
DeFeo, W. E.	Le, H. Q.
DiCecca, S.	Nabors, C. D.
Dill, C. D., III	Ochoa, J. R.
Fan, T. Y.	Schulz, P. A.
Hancock, R. C.	Sullivan, D. J.
Henion, S. R.	Wall, K. F.
Hotaling, T. C.	Zayhowski, J. J.

ELECTRONIC MATERIALS

A. J. Strauss, *Leader*
B-Y. Tsaur, *Associate Leader*

Anderson, C. H., Jr.	Kolesar, D. F.
Button, M. J.	Krohn, L., Jr.
Chen, C. K.	Marino, S. A.
Choi, H. K.	Mastromattei, E. L.
Clark, H. R., Jr.	McGilvary, W. L.
Connors, M. K.	Nitishin, P. M.
Eglash, S. J.	Pantano, J. V.
Fahey, R. E.	Turner, G. W.
Finn, M. C.	Wang, C. A.
Iseler, G. W.	

HIGH SPEED ELECTRONICS

R. A. Murphy, *Leader*
M. A. Hollis, *Assistant Leader*
R. W. Chick, *Senior Staff*

Actis, R.	Mathews, R. H.
Bergeron, N. J.	Mattia, J. P.*
Bozler, C. O.	McIntosh, K. A.
Brown, E. R.	McMorran, R. A.
Calawa, A. R.	McNamara, M. J.
Chen, C. L.	Nichols, K. B.
Clifton, B. J.[‡]	Parker, C. D.
Goodhue, W. D.	Rabe, S.
Gray, R. V.	Rathman, D. D.
Lincoln, G. A., Jr.	Smith, F. W., III
Mahoney, L. J.	Vera, A.
Manfra, M. J.	

* Research Assistant
[†] Part Time
[‡] Leave of Absence

ELECTROOPTICAL DEVICES

R. C. Williamson, *Leader*
D. L. Spears, *Assistant Leader*
R. H. Rediker, *Senior Staff*

Aull, B. F.	Missaggia, L. J.
Bailey, R. J.	Mull, D. E.
Betts, G. E.	O'Donnell, F. J.
Corcoran, C. J.*	Palmacci, S. T.
Cox, C. H., III	Palmateer, S. C.
Donnelly, J. P.	Pheiffer, B. K.*
Ferrante, G. A.	Reeder, R. E.
Groves, S. H.	Roussell, H. V.
Harman, T. C.	Shiple, S. D.*
Hovey, D. L.	Tsang, D. Z.
Johnson, L. M.	Walpole, J. N.
Liau, Z. L.	Woodhouse, J. D.
Lind, T. A.	Yee, A. C.

ANALOG DEVICE TECHNOLOGY

R. W. Ralston, *Leader*
R. S. Withers, *Associate Leader‡*
T. C. L. G. Sollner, *Assistant Leader*
A. C. Anderson, *Senior Staff*
R. M. Lerner, *Senior Staff†*

Arsenault, D. R.	Lyons, W. G.
Bhushan, M.‡	Macedo, E. M., Jr.
Boisvert, R. R.	Minnick, R. G.
Brogan, W. T.	Oates, D. E.
Denneno, A. P.	Sage, J. P.
Denneno, J. M.	Seaver, M. M.
Fitch, G. L.	Slattery, R. L.
Green, J. B.	Westerheim, A. C.*
Holtham, J. H.	Whitley, D. B.
Lattes, A. L.	Yu-Jahnes, L. S.*

MICROELECTRONICS

E. D. Savoye, *Leader*
B. B. Kosicki, *Assistant Leader*
B. E. Burke, *Senior Staff*
A. M. Chiang, *Senior Staff*

Chuang, M. L.*	Felton, B. J.	Loomis, A. H.
Collins, I. K.	Gregory, J. A.	McGonagle, W. H.
Cooper, M. J.	Huang, C. M.	Mountain, R. W.
Daniels, P. J.	Hurley, E. T.	Percival, K. A.
Doherty, C. L., Jr.	Johnson, B. W.	Pichler, H. H.
Dolat, V. S.	Johnson, K. F.	Reich, R. K.
Donahue, T. C.	LaFranchise, J. R.	Reinold, J. H., Jr.
Durant, G. L.		Young, D. J.

* Research Assistant
† Part Time
‡ Leave of Absence

1. ELECTROOPTICAL DEVICES

1.1 TAPERED TRAVELING-WAVE OPTICAL POWER AMPLIFIER USING STRAINED LAYERS

High-power, single-spatial-mode sources are required for efficient pumping of rare-earth-doped fiber amplifiers and lasers. We have demonstrated a tapered amplifier that uses strained-layer InGaAs/ AlGaAs material in a master-oscillator/power-amplifier (MOPA) configuration capable of high-power CW operation at a wavelength suitable for pumping erbium.

Gain saturation limits high-power operation in amplifiers. Broad-stripe amplifiers can achieve higher saturation power than single-mode waveguide amplifiers by increasing the total gain volume, but both tend to be inefficient because energy is not fully extracted along the length of the strip until gain saturation is reached. After that point the remaining length of the amplifier provides little incremental power. High power and efficient energy extraction can be achieved while maintaining a single spatial mode by tapering the active medium width to match the diffraction of a Gaussian beam. With this geometry the amplified signal is spread out over a larger area as it gains power. Exponentially tapered amplifiers have been proposed [1], and adiabatic mode expansion from narrow-stripe sources into broad-stripe amplifiers has been reported [2]. We have now demonstrated an amplifier with a linearly tapered gain region having high saturation power and output in a nearly single lobed spatial mode.

The amplifier is fabricated from InGaAs/AlGaAs graded-index separate-confinement heterostructure single-quantum-well (GRIN-SCH SQW) semiconductor material similar to that reported in [3]. When this material is made into 600-μm-long broad-stripe lasers, it has a threshold current density of 185 A/cm^2 and a differential quantum efficiency of 47%/facet under pulsed conditions. The active region of the amplifier is defined by a linearly tapered contact pad and is 2 mm long. The input and output facets are antireflection coated.

The amplifier has been tested using a single-frequency Ti:Al$_2$O$_3$ laser as the master oscillator. A spherical lens telescope and a cylindrical lens telescope were used to shape the TM$_{00}$ beam of the Ti:Al$_2$O$_3$ laser to match the input aperture of the amplifier. Two fast objective lenses coupled light into and out of the amplifier. The amplifier was operated at a heat sink temperature of 21°C. With 95 mW of power at a wavelength of 970 nm incident on the input objective, the output power was nearly saturated. Figure 1-1 shows the dependence of CW output power on bias current under these conditions. The slope of the total emitted power is 0.66 W/A, corresponding to a differential quantum efficiency of 51%. Figure 1-2 shows the far-field intensity profile of the output beam along the axis parallel to the junction at a bias current of 1.9 A. The total emitted power is 1.2 W with 1.0 W (83%) of the power contained in the main lobe. To our knowledge, this is the highest CW power reported from an amplifier at this wavelength. By using a semiconductor laser as the master oscillator, this MOPA can be a compact, efficient source for pumping erbium-doped fiber as well as be suitable as a transmitter for free-space laser communication applications.

J. N. Walpole   C. A. Wang
E. S. Kintzer   L. J. Missaggia
S. R. Chinn
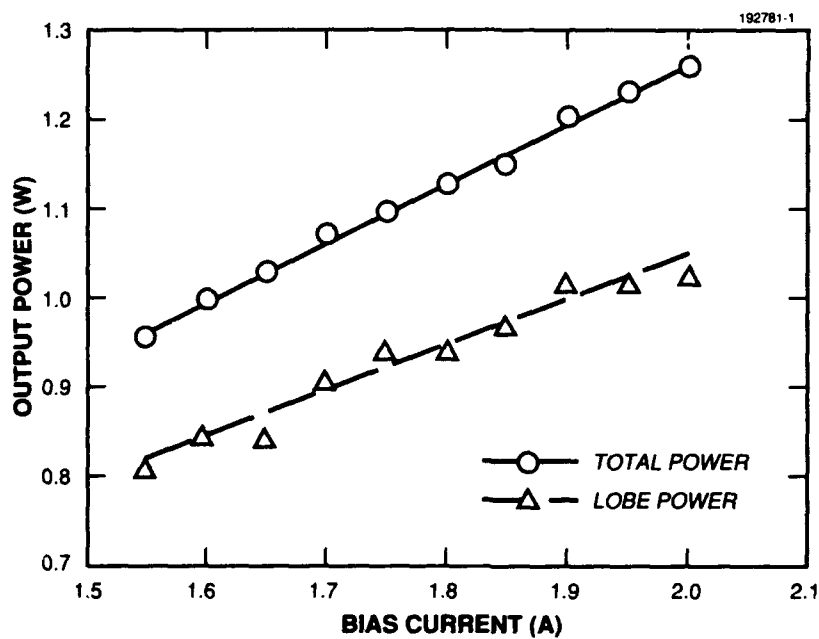
Figure 1-1. Light-current characteristic for the tapered amplifier with an input power of 95 mW. Circles indicate the total power emitted from the output facet while triangles indicate the power contained in the main lobe.
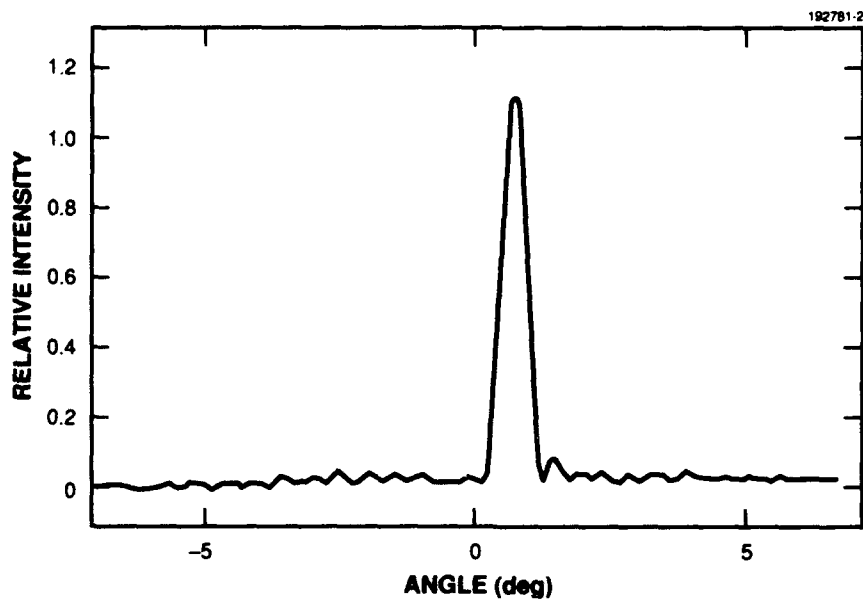
Figure 1-2. Far-field intensity profile of the amplifier output along the axis parallel to the junction at a bias current of 1.9 A and an input power of 95 mW. Total power is 1.2 W and the power in the main lobe is 1.0 W.

2

1.2 MONOLITHIC TWO-DIMENSIONAL SURFACE-EMITTING ARRAYS OF AlGaAs HORIZONTAL-CAVITY DIODE LASERS WITH ETCHED FACETS AND EXTERNAL PARABOLIC DEFLECTING MIRRORS

Arrays of semiconductor diode lasers are needed for applications that require the efficient generation of higher power levels than can be obtained with a single device. Monolithic two-dimensional arrays of surface-emitting lasers have several potential advantages over composite arrays of edge-emitting lasers with conventional cleaved end facets. Such advantages include the possibility of mass production and a more precise photolithographically defined two-dimensional output pattern that should make it simpler to integrate monolithic arrays with arrays of lenses. Several types of surface-emitting lasers in the GaAs/AlGaAs material system have been reported. These include lasers with resonant cavities normal to the surface [4], lasers with internal 45° cavity-folding mirrors [5]-[7], lasers with vertical etched facets and external deflecting mirrors [5],[8], and lasers that utilize a grating coupler to achieve emission normal to the surface [9]. Although considerable progress has been made in developing these lasers, substantial improvements are still needed before the performance of arrays of any surface-emitting lasers will rival that of composite arrays of cleaved-facet lasers.

Recently, low threshold current densities J_{th} and significantly improved external differential quantum efficiencies η_d have been reported for surface-emitting lasers with internal 45° cavity-folding mirrors [6],[7]. Small arrays of strained-layer AlInGaAs/AlGaAs quantum-well lasers with two internal 45° cavity-folding mirrors operating at a wavelength of 815 nm had J_{th} as low as 220 A/cm^2 and η_d as high as 53%. Similar strained-layer InGaAs/AlGaAs arrays operating at 1.03 μm had J_{th} as low as 160 A/cm^2 and η_d as high as 56% [7]. In this section, we report results on monolithic two-dimensional arrays of AlGaAs lasers with vertical etched facets and external parabolic deflecting mirrors, which are comparable to those of the strained-layer folded-cavity arrays. Although arrays of this type are more difficult to fabricate than arrays with folded-cavity lasers, higher performance should eventually be possible since there are no inherent diffraction losses (as in a folded-cavity laser).

The design of the laser arrays reported here is schematically illustrated in Figure 1-3. The arrays are fabricated in AlGaAs material with a GRIN-SCH SQW structure. The output beam divergence ($\leq 36°$ full width at half-maximum) of cleaved-facet lasers made with this material is smaller than the beam divergence ($\leq 45°$) of similar lasers made with the SCH SQW material used in the previously reported arrays with optical parabolic mirrors [5],[8]. The GRIN-SCH SQW structure is grown on an n^+-GaAs substrate by organometallic vapor phase epitaxy (OMVPE). The quantum well is 100 Å thick and contains ~ 7 mole % AlAs. The GRIN regions are graded from 30 to 60 mole % AlAs over ~ 2000 Å. The upper (p-type) and lower (n-type) cladding layers contain 60 mole % AlAs and are ~ 1.7 μm thick. A top p^+-GaAs contacting layer ~ 0.2 μm thick completes the structure. Broad-area lasers with 750-μm-long cavities fabricated in this material had a J_{th} of 214 A/cm^2 and η_d of 76%.

The fabrication of the arrays was similar to that previously described [5],[8], except that 4× chrome masks (produced with an optical pattern generator) and a 4:1 projection aligner were used for the facet and parabolic deflector photoresist exposure steps. We believe the 4× masks improve the smoothness of the edge of the photoresist mask used to dry etch the facets and therefore the smoothness of the facets themselves. In addition, the cavity length was increased from 250 to 1000 μm, which is more in line with obtaining low J_{th} in SQW lasers.

3
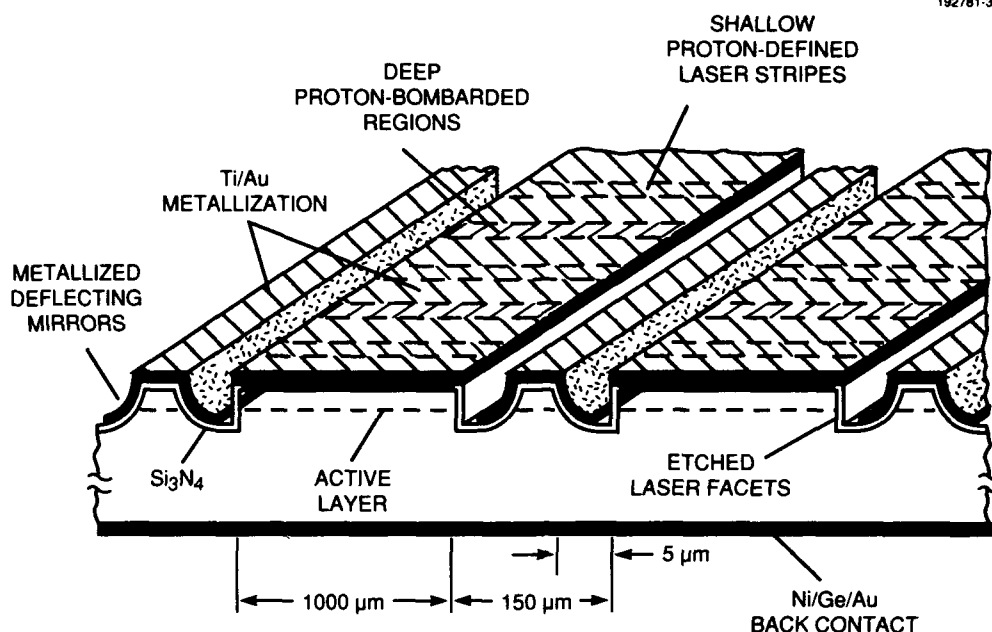
Figure 1-3. Schematic diagram of a monolithic two-dimensional array of surface-emitting AlGaAs diode lasers with etched facets and external parabolic deflecting mirrors.

The first step in the fabrication was to etch the laser facets. With photoresist as an etch mask, ion-beam-assisted etching (IBAE) [5] was used to form pairs of straight-sided grooves 2 μm wide and ~ 3 μm deep. The outer walls of each pair act as the facets for rows of laser cavities 1000 μm long. Lines ~ 3 μm wide immediately adjacent to the inside edge of one of the grooves in each pair were then opened in a new layer of photoresist, and parabolic deflectors were formed by computer-controlled angled IBAE [5]. The deflectors for the other side of each row were formed in a similar manner. A shallow proton bombardment was used to confine the injection current to 40-μm-wide stripes on 125-μm centers, while a deep proton bombardment midway between the laser stripes was used to introduce sufficient optical loss to suppress transverse lasing. Further details of the fabrication are given in [5] and [8].

The pulsed output power vs current of a 19-element array is plotted in Figure 1-4. The J_{th} is ~ 230 A/cm^2, which compares favorably to that measured on broad-area cleaved-facet lasers made in the same material. The η_d of this small array is about 56%, which is over a factor of 2 better than previously obtained in arrays of this type in AlGaAs. It is still lower than that observed in cleaved-facet broad-area lasers, however. We believe the primary reason for the lower efficiency is the incomplete collection of the light emitted from the laser facet by the deflecting mirrors.

Although we obtained small arrays with $\eta_d > 50\%$ from several other etched samples, larger arrays tended to have lower η_d, as illustrated in Figure 1-5, which plots the power output vs current of a 76-element array (~ 0.11 cm^2). The J_{th} of this array (~ 240 A/cm^2) is comparable to that of the smaller array, but η_d is now only about 43%. The uniformity of these arrays appears to be limited by the accuracy with which we can align the two parabolic deflector masks to the etched facets over large areas with our 4X mask aligner.

4
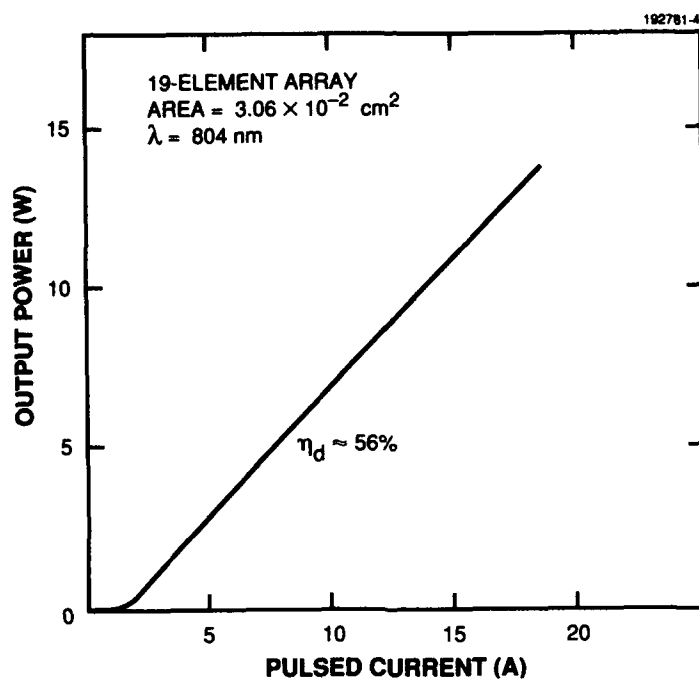
Figure 1-4. Pulsed power output vs current of a 19-element array. The current pulses were 500 ns wide at a 1-kHz repetition rate.
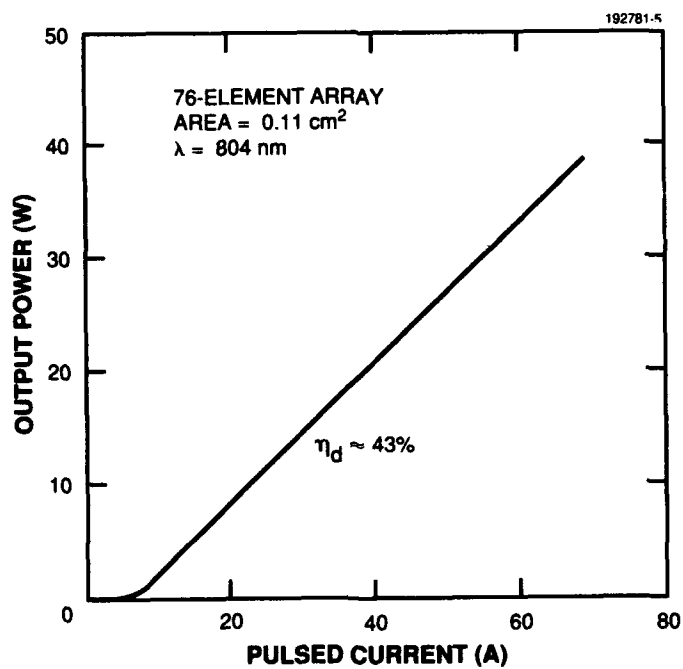
Figure 1-5. Pulsed power output vs current of a 76-element (19 elements/row by 4 rows) array.

5

The low J_{th} of these arrays indicate high facet quality. The value is not as low as the best obtained on strained-layer folded-cavity arrays [7]. However, comparison of the J_{th} to that of broad-area cleaved-facet lasers made in the same material is better for these arrays than for strained-layer folded-cavity arrays ($\sim$ 230 A/cm^2 vs 214 A/cm^2 for these arrays and $\geq$ 160 A/cm^2 vs 85 A/cm^2 for folded-cavity arrays). Higher η_d in arrays of this type is anticipated by using laser structures with an even smaller divergence angle ($\leq$ 30°) and deeper junctions. Both of these changes should increase the fraction of light emitted from the laser facets that is collected by the deflecting mirrors. In addition, the use of a self-aligned technique to accurately align the edge of the facets and parabolic deflectors in one step should improve uniformity and permit the fabrication of large high-performance arrays.

J. P. Donnelly   W. D. Goodhue
R. J. Bailey   C. A. Wang
G. A. Lincoln   G. D. Johnson

1.3 GaInP/GaInAsP/InGaAs STRAINED-LAYER SEPARATE-CONFINEMENT HETEROSTRUCTURES GROWN BY OMVPE

GaAs-based strained-layer SCH SQW lasers with $Ga_{0.51}In_{0.49}P$ (referred to as GaInP) cladding have been previously reported [10]. These devices are of interest because of, among other things, their potential for superior reliability compared to lasers incorporating AlGaAs alloys. Also, the mass transport of GaInP has been demonstrated for fabrication of buried-heterostructure lasers and can be useful for a variety of other tasks. The SCH SQW structure reported earlier was composed entirely of binary and ternary materials, with GaInP, GaAs, and InGaAs as the cladding, confinement, and strained layers, respectively. To understand and optimize device performance, however, it is desirable to fabricate structures incorporating GaInAsP quaternary alloys both as larger-bandgap confinement layers and as intermediate-bandgap step or grading layers. We report here the successful growth of SCH SQW structures with quaternary confinement layers, which could only be achieved after the key factors influencing crystal quality had been identified and controlled. The material has been evaluated by double-crystal x-ray diffraction (DXD), photoluminescence (PL), and differential interference contrast (DIC) microscopy.

The undoped layered structure investigated is shown in Figure 1-6. It is similar to that for a SCH SQW laser with emission at $\sim$ 980 nm. The $Ga_xIn_{1-x}As_yP_{1-y}$ alloy with $x \approx 0.7$ and $y \approx 0.3$ has an energy gap of 1.65 eV, which is about that of $Al_zGa_{1-z}As$ with $z = 0.2$. The layers were grown by OMVPE at 650°C on n^+-GaAs substrates using a chimney-type reactor incorporating susceptor rotation and operating at atmospheric pressure [11].

The morphology and quality of the GaInAsP alloy grown over the GaInP have been evaluated. As noted in [10], smooth layers of GaInP lattice matched to GaAs can be grown with atmospheric-pressure OMVPE if the substrate surface is given a sizable ($\sim$ 5°) misorientation from (001) toward the [111] direction. (Here, a surface is considered smooth if it has no structure as viewed by DIC microscopy.) An obvious starting objective was to obtain a lattice-matched condition between the binary, ternary, and quaternary components at the growth temperature. However, this led to layers with a slightly rough morphology, as shown in Figure 1-7. Both the 1.65-eV-energy-gap GaInAsP and the GaInP alloys are

6

metastable at the 650°C growth temperature, and they derive their stability as epitaxial layers from the elastic energy of the lattice [12]. The rough morphology may be an indication of partial spinoidal decomposition. When the GaInAsP was instead grown under compression with respect to the GaInP, smooth layers were reproducibly obtained. A preliminary interpretation of this result is that the biaxial compression suppresses the spinodal decomposition. Additional work is needed to explain why the compression with respect to the GaInP rather than the GaAs is important.

$Ga_{0.51}In_{0.49}P$ (~0.6μm)

$Ga_{0.7}In_{0.3}As_{0.3}P_{0.7}$ (~0.2 μm)

$In_{0.18}Ga_{0.82}As$ (~7 μm)

$Ga_{0.51}In_{0.49}P$ (~0.6μm)

GaAs BUFFER LAYER

n^+-GaAs SUBSTRATE
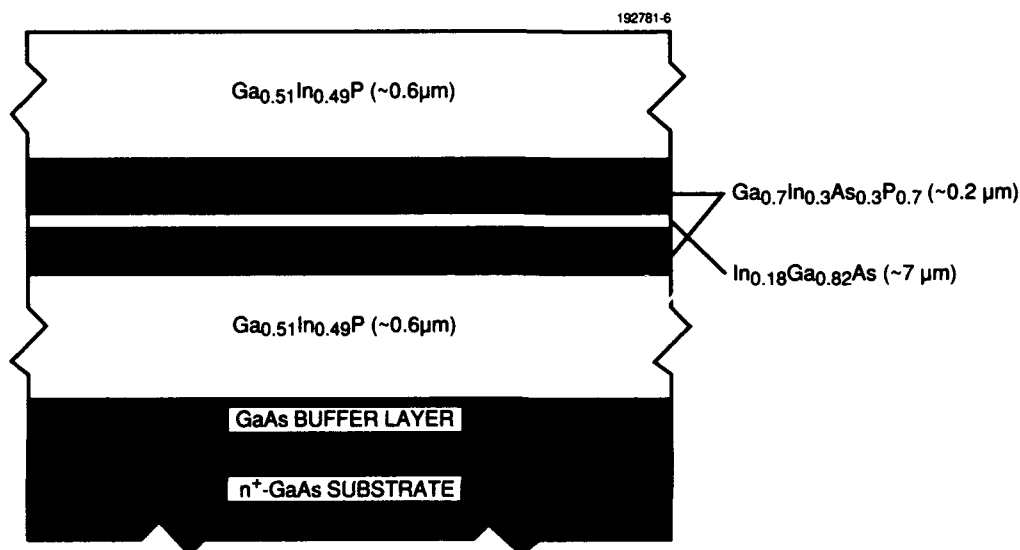
Figure 1-6. Strained-layer SCH SQW structure, which differs from a full SCH SQW laser structure in that the upper and lower $Ga_{0.51}In_{0.49}P$ cladding layers are undoped and of reduced thickness.

With smooth GaInAsP, the growth of smooth GaInP as a top layer presents no problem. This situation changes markedly, however, when the thin strained layer of InGaAs is included in the structure, as shown in Figure 1-8. Yet, when the rough GaInP is removed by selective chemical etching, surprisingly the morphology of the GaInAsP over the InGaAs is found to be smooth. Rocking curves of such a structure before and after the selective etching are shown in Figure 1-9. As seen, etching causes a change in the rocking curve over a large range of diffraction angles, which indicates that the lattice constant of the removed GaInP is poorly defined. Empirically, it has been found that the roughness of the top layer is minimized by the conditions that the GaInAsP must be slightly compressed with respect to the GaInP and that both materials must have nearly the same room-temperature lattice constant as GaAs.
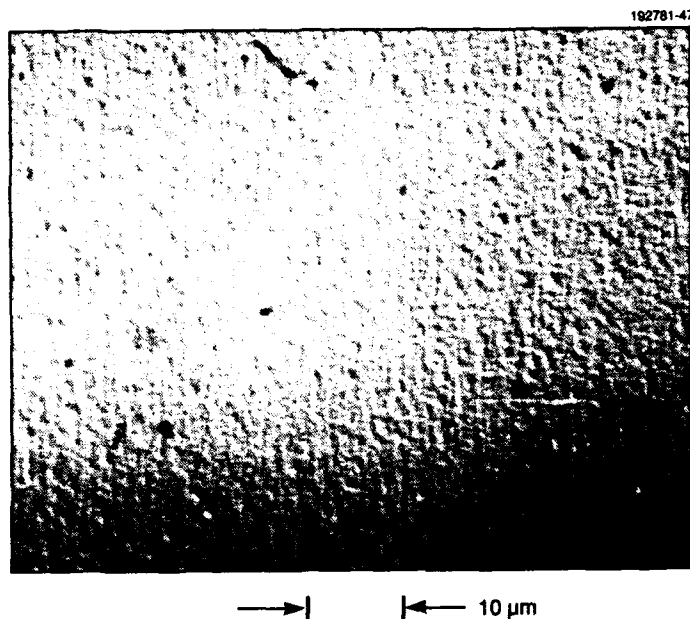
Figure 1-7. Photomicrograph of $Ga_{0.7}In_{0.3}As_{0.3}P_{0.7}$ surface showing the rough morphology that results when this alloy is grown on the lower $Ga_{0.51}In_{0.49}P$ layer under lattice-matched conditions.
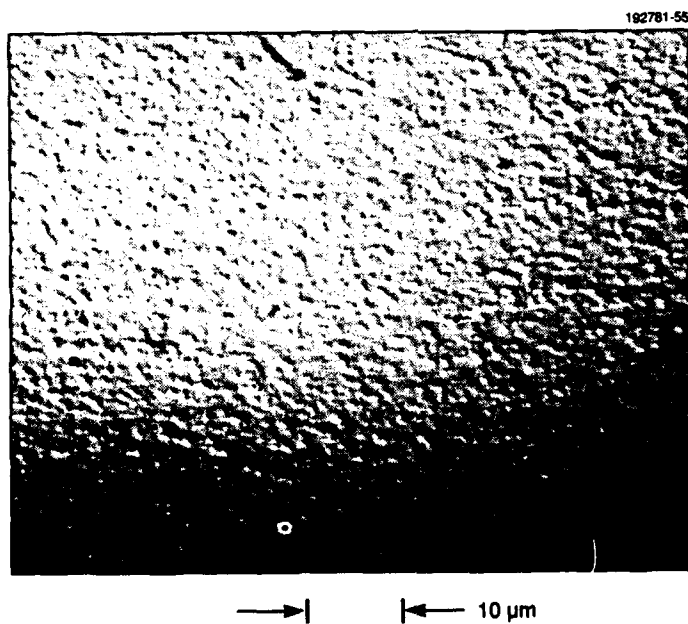
Figure 1-8. Photomicrograph of $Ga_{0.51}In_{0.49}P$ surface for the structure in Figure 1-6, showing a typically rough morphology.
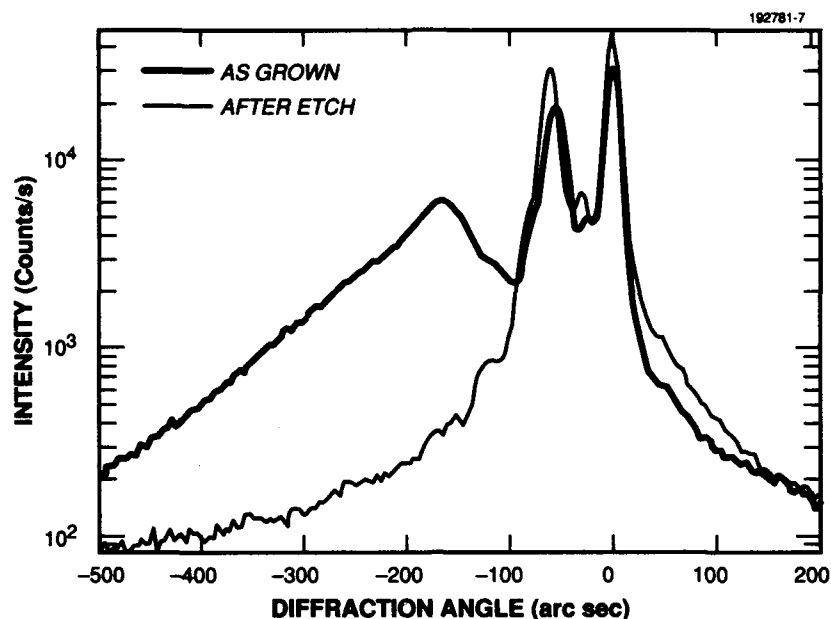
Figure 1-9. (004) DXD rocking curves before and after removal of the upper GaInP layer, showing that the lattice constant of this layer is poorly defined. The GaAs substrate peak is set at 0 arc sec, and the peak at −58 arc sec is due to the lower GaInP and the GaInAsP layers.

A marked improvement in morphology results when the structure in Figure 1-6 is modified to include a thin (~ 200 Å) layer of GaAs grown between the InGaAs and the GaInAsP. Rocking curves for the modified structure before and after selective etching are shown in Figure 1-10, in which the diffraction from the upper GaInP layer is seen to be well localized. With the insertion of the thin GaAs, the PL peak intensities for both the upper GaInP and the InGaAs are 10 to 100 times greater than those for the unmodified structure. Not unexpectedly, this result indicates a strong dependence of nonradiative recom   'ion rates on morphology.

Although more work is needed to establish a correct interpretation of the role of the thin GaAs layer, it seems that having a lattice-constant reference or template on each side of the strained layer is important for maintaining the in-plane lattice constant. Apparently, the GaInAsP alloy alone is too compliant for this purpose. The lattice constant shift implied by this explanation does not affect the morphology of the GaInAsP alloy but does degrade the GaInP.

S. H. Groves
D. R. Calawa
A. Napoleone

9
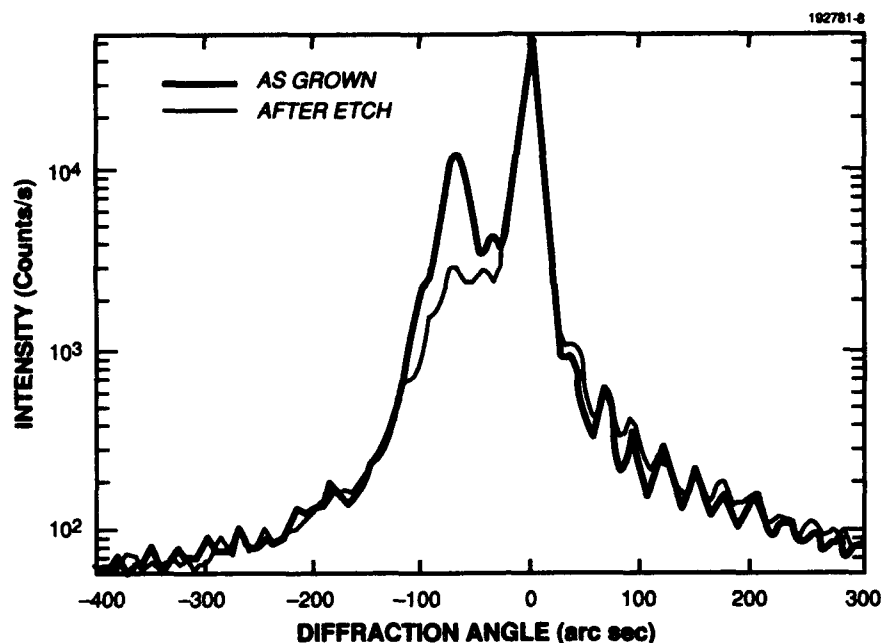
Figure 1-10. DXD rocking curves for the modified structure showing that the upper GaInP layer in this case has a well-defined lattice constant. (The modified structure contains ~ 200 Å GaAs on top of the InGaAs layer.) The upper GaInP and the GaInAsP contributions lie at ~ −70 arc sec, and the lower GaInP peak lies under that of the substrate.

REFERENCES

1. G. Bendelli, K. Komori, S. Arai, and Y. Suematsu, *IEEE Photon. Technol. Lett.* **3**, 42 (1991).

2. U. Koren, R. M. Jopson, B. I. Miller, M. Chien, M. G. Young, C. A. Burrus, C. R. Giles, H. M. Presby, G. Raybon, R. D. Evankow, B. Tell, and K. Brown-Goebeler, *Appl. Phys. Lett.* **59**, 2351 (1991).

3. H. K. Choi and C. A. Wang, *Appl. Phys. Lett.* **57**, 321 (1990).

4. R. S. Geels and L. A. Coldren, *Appl. Phys. Lett.* **57**, 1605 (1990).

5. W. D. Goodhue, K. Rauschenbach, C. A. Wang, J. P. Donnelly, R. J. Bailey, and G. D. Johnson, *J. Electron. Mater.* **19**, 463 (1990).

6. S. S. Ou, J. J. Yang, M. Jansen, M. Sargent, L. J. Mawst, and J. Z. Wilcox, *Appl. Phys. Lett.* **58**, 16 (1991).

7. W. D. Goodhue, J. P. Donnelly, C. A. Wang, G. A. Lincoln, K. Rauschenbach, R. J. Bailey, and G. D. Johnson, *Appl. Phys. Lett.* **59**, 632 (1991).

8. J. P. Donnelly, W. D. Goodhue, T. H. Windhorn, R. J. Bailey, and S. A. Lambert, *Appl. Phys. Lett.* **51**, 1138 (1987).

9. G. A. Evans, N. W. Carlson, J. M. Hammer, M. Lurie, J. K. Butler, S. L. Palfrey, R. Amantea, L. A. Carr, F. Z. Hawrylo, E. A. James, C. J. Kaiser, J. B. Kirk, W. F. Rerchert, S. R. Chinn, J. R. Shealy, and P. S. Zory, *Appl. Phys. Lett.* **53**, 2123 (1988).

10. Solid State Research Report, Lincoln Laboratory, MIT, 1991:1, p.1; Z. L. Liau, S. C. Palmateer, S. H. Groves, J. N. Walpole, and L. J. Missaggia, to be published in *Appl. Phys. Lett.*

11. S. C. Palmateer, S. H. Groves, J. W. Caunt, and D. L. Hovey, *J. Electron. Mater.* **18**, 645 (1989).

12. G. B. Stringfellow, *J. Cryst. Growth* **65**, 454 (1983).

2. QUANTUM ELECTRONICS

2.1 HIGH-POWER CW OPERATION OF MICROCHIP LASERS

A CW output power of 2 W from a 1.064-μm microchip laser [1] has been demonstrated. The laser was 640 μm long with flat mirrors and 2% output coupling. It was pumped with a Ti:Al$_2$O$_3$ laser tuned to 808 nm, the absorption peak of Nd:YAG. The Ti:Al$_2$O$_3$ laser was focused with a 35-mm lens to a spot size ~ 50 μm in ‹ameter on the microchip laser, which was heatsunk on two adjacent sides to a room-temperature, water-cooled copper block. Figure 2-1 shows the output power of the microchip laser as a function of incident pump power.

As shown in Figure 2-1, the power efficiency of the microchip laser increased with pump power up to 2 W. This increase has been observed in several earlier experiments with pump powers up to 1.3 W [2]. The microchip laser oscillates in a single longitudinal mode at low pump powers. As this power increases, additional modes reach threshold [3]. These modes are able to use the population inversion at the nulls in the standing-wave pattern produced by the first mode, thereby increasing the efficiency of the laser. The maximum power efficiency obtained in the experiment reported here was ~ 56%.

At pump powers in excess of 2 W the power efficiency of the laser decreased, to ~ 38% at 5.3 W. A likely explanation for the decrease is increased thermally induced optical aberrations within the cavity. This explanation is consistent with measurements of the M^2 parameter (the "times-diffraction-limited" performance of a laser) of the microchip laser output. Near threshold, at an incident pump power of 17 mW, M^2 was < 1.3. At an incident pump power of 2 W (~ 1 W of output power), M^2 was ~ 1.6. This value increased to > 5 at a pump power of 5.3 W.

J. J. Zayhowski
S. R. Henion
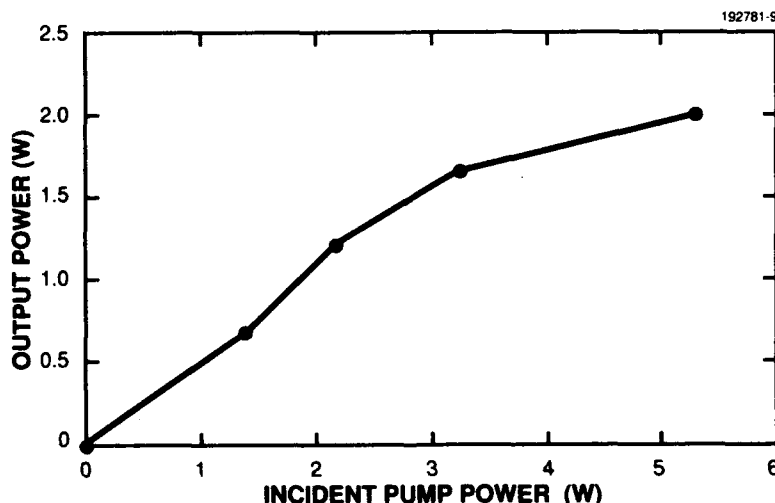
Figure 2-1. Output power as a function of incident pump power for a 640-μm-long 1.064-μm Nd:YAG microchip laser.

2.2 ELECTROOPTICALLY Q-SWITCHED MICROCHIP LASER

By electrooptically Q switching a microchip laser [1],[4], a train of single-frequency pulses has been obtained with a full width at half-maximum of < 2 ns at repetition rates up to 140 kHz. The pulse train and an individual pulse are shown in Figure 2-2.
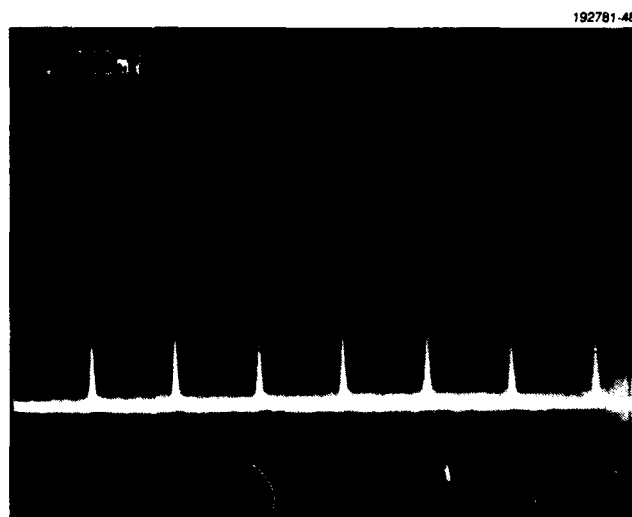
(a)
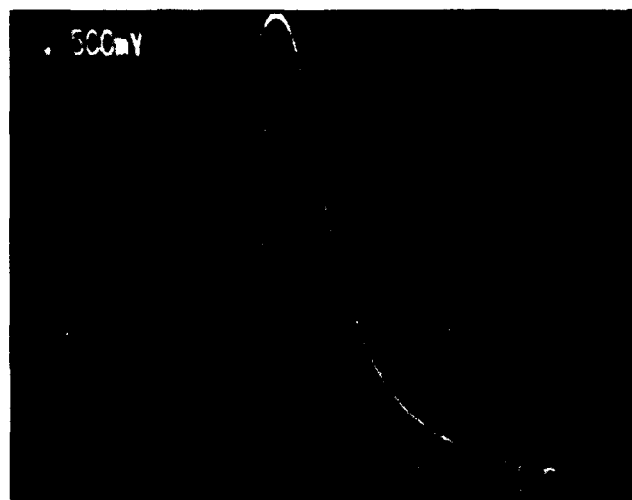
(b)

Figure 2-2. Output obtained from an electrooptically Q-switched 1.064-μm Nd:YAG microchip laser showing (a) a train of pulses and (b) one pulse on an expanded time scale.

The electrooptically Q-switched microchip laser, illustrated in Figure 2-3, consisted of a 532-μm-long piece of Nd:YAG bonded to a 904-μm-long piece of LiTaO$_3$. Both materials were polished flat and parallel on the two faces normal to the optic axis. The pump face of the Nd:YAG was coated to transmit the pump light and to be highly reflective at the oscillating wavelength (1.064 μm). A partially transmitting mirror between the two materials had a reflectivity of 95% at 1.064 μm and was highly reflecting at the pump wavelength. The opposite face of the LiTaO$_3$ was coated for 50% reflectivity at 1.064 μm. The LiTaO$_3$ was oriented with its c-axis orthogonal to the cavity axis. Electrodes were deposited on the two faces of LiTaO$_3$ normal to the c-axis, with an electrode spacing of ~ 1 mm.
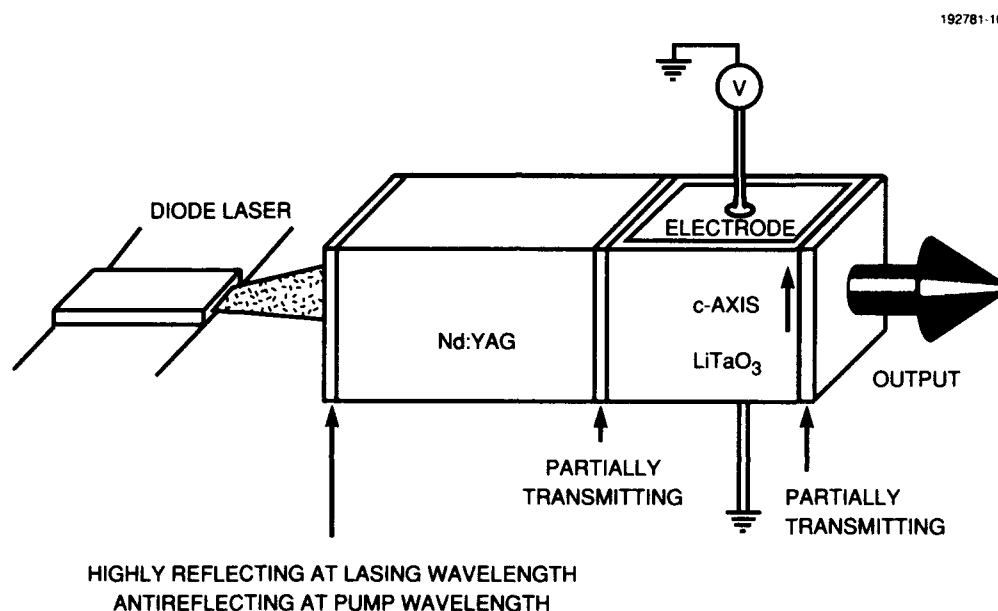
Figure 2-3. Diagram of an electrooptically Q-switched microchip laser. In these experiments the Nd:YAG crystal is 0.532 × 1.0 × 1.0 mm and the LiTaO₃ crystal is 0.904 × 1.0 × 1.0 mm.

The microchip laser was pumped with a Ti:Al$_2$O$_3$ laser to simulate the performance of the pump diode. A 1-kV pulse of 100-ns duration was used to Q switch the device. At an incident pump power of 400 mW, we obtained 40 mW of single-frequency Q-switched output pulses with a full width at half-maximum of < 2 ns at repetition rates up to 140 kHz. We are currently developing a fieldable diode-pumped version of this device.

We also frequency doubled the output of the Q-switched microchip laser to obtain 4 mW of single-frequency green pulses at a repetition rate of 100 kHz. By reducing the reflectivities of the partially reflecting mirrors, it will be possible to increase the peak power of the pulses [5] and obtain better than 50% doubling efficiency from the diode-pumped Q-switched microchip laser.

J. J. Zayhowski   C. Dill
J. L. Daneu   R. C. Hancock
C. Cook

2.3 MICROCHIP LASER ARRAYS WITH CURVED MIRRORS

Diode-laser-pumped monolithic solid state lasers are an attractive approach for the design of efficient all-solid-state lasers. Such lasers commonly have a two-mirror standing-wave cavity with one flat mirror and one curved mirror [6],[7]. The curved mirror is used to stabilize the laser cavity and create a well-defined cavity mode. However, creating curved mirrors using conventional techniques requires individually polishing each gain crystal—a process that can be time consuming and expensive. It has been demonstrated that pump-induced thermal effects in longitudinally pumped microchip lasers can eliminate the need for a curved mirror [1],[8]. This allows large wafers of gain media to be polished and dielectrically coated before being diced into small sections, each section being a complete laser cavity. The gain medium in such a laser must have an increase in optical length with increasing temperature. In addition, the tolerance on misalignment of the two flat mirrors forming the laser cavity is extremely small. For Nd:YAG microchip lasers, for example, the mirror misalignment tolerance is typically 10 μrad [8].

Previously, we reported a method for mass producing two-dimensional arrays of microchip lasers with curved mirrors [9]. The use of a curved mirror relaxes the tolerance on mirror misalignment, allows the use of a gain medium with a decrease in optical length with increasing temperature, reduces the radius of the oscillating mode, and lowers the threshold of the laser.

Several arrays of Nd:YAG microchip lasers were constructed with one curved mirror and one flat mirror. Array elements were ~ 1 mm square on 1.3-mm centers. These devices had a cavity length of 532 μm, a radius of curvature of ~ 1 m, and a 5% output coupler. Each curved-mirror array went through all processing steps with a flat-flat (conventional) microchip array to serve as a control in subsequent testing. Calculations indicate that thermal effects should result in a mode radius of ~ 150 μm for the flat-flat cavities near threshold [8]. The curved-mirror cavities should have a mode radius of ~ 88 μm at threshold and should therefore have a threshold ~ 0.34 times as large as the flat-flat cavities and a low-power divergence ~ 1.7 times as large.

To characterize the curved-mirror microchip lasers, they were pumped with an 808-nm Ti:Al$_2$O$_3$ laser focused to a 25-μm-radius spot and were compared to their flat-flat controls. Figures 2-4 through 2-6 show histograms of the thresholds (incident pump power) of all of the elements in the curved-mirror arrays for three different coating runs, and the thresholds of spots in the flat-flat controls taken on 1.25-mm centers. It can be seen that the curved-mirror lasers had significantly lower and more consistent thresholds. Measurements of the divergence of the output from curved-mirror and flat-flat devices were consistent with the calculated mode radii. The optical slope efficiency of both sets of devices was typically 25%.

J. J. Zayhowski
J. L. Daneu
R. C. Hancock
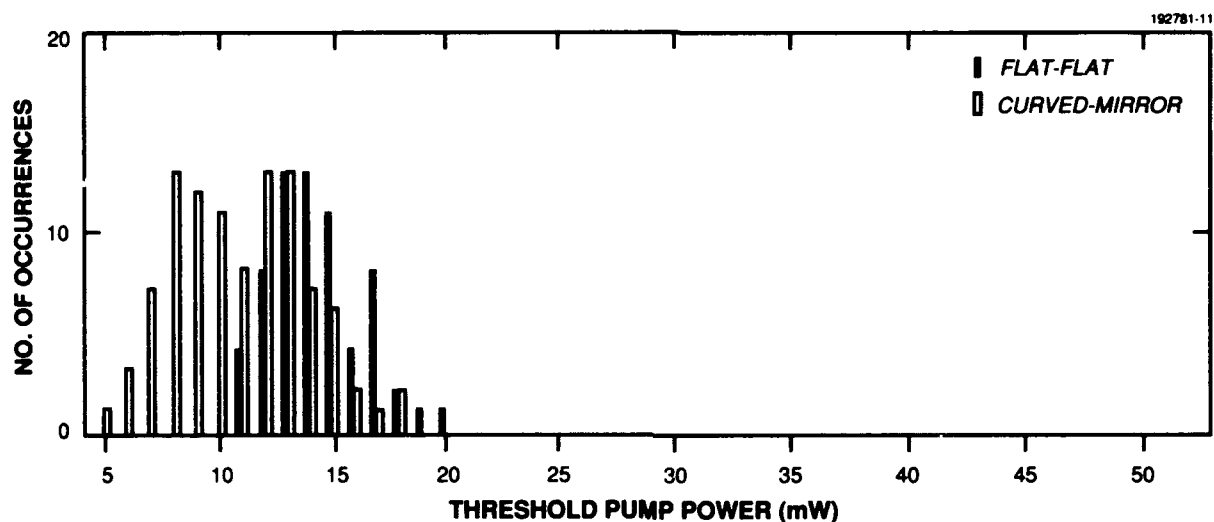
Figure 2-4. Histogram of the thresholds (incident pump power) of curved-mirror and flat-flat microchip lasers from coating run 1.
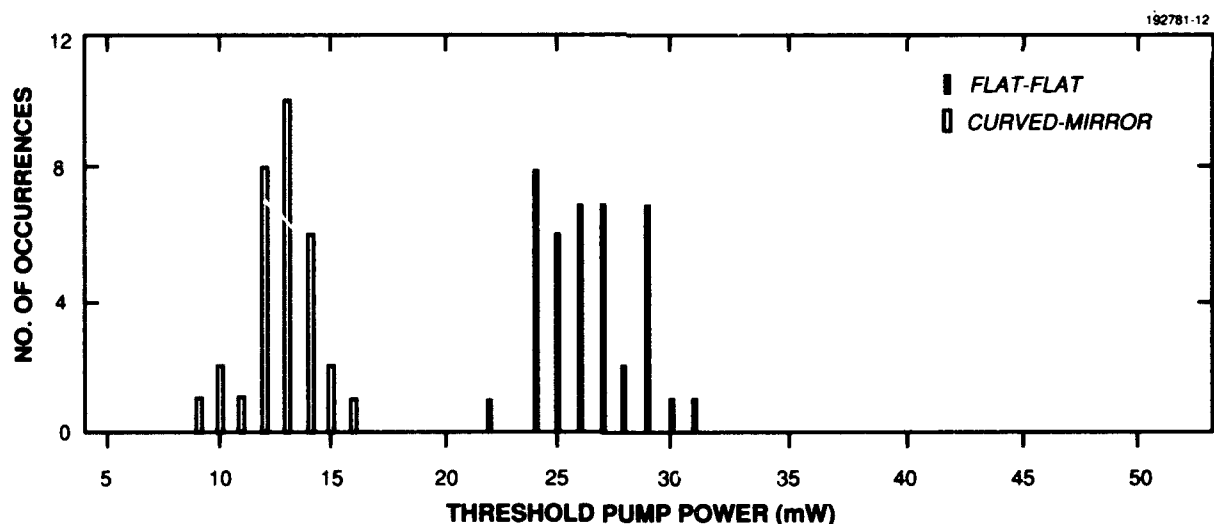
Figure 2-5. Histogram of the thresholds (incident pump power) of curved-mirror and flat-flat microchip lasers from coating run 2.

17
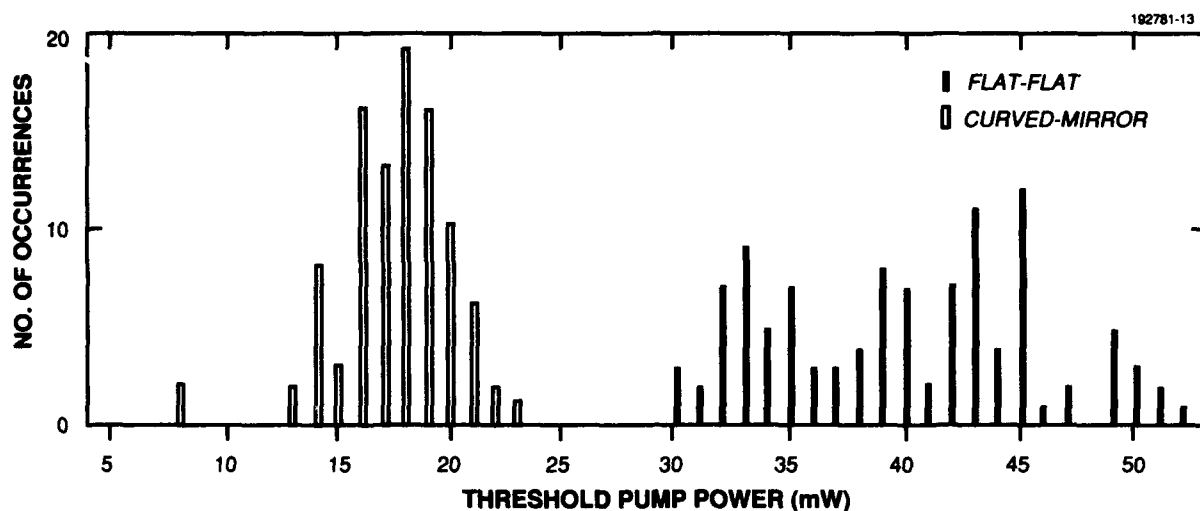
Figure 2-6. Histogram of the thresholds (incident pump power) of curved-mirror and flat-flat microchip lasers from coating run 3.

2.4 MODE LOCKING AND HIGH POWER OF Yb:YAG LASER

The room-temperature Yb:YAG laser at 1.03 μm has the potential for high-power, single-spatial-mode operation because of its broad absorption bandwidth (making control of the pump wavelength less important), the absence of mechanisms other than radiative relaxation that deplete the upper state, and the low thermal loading as a result of the small quantum defect [10]. The lasing transition has a 60-cm^{-1} width, which may allow mode locking to give pulses as short as 0.2 ps. We present initial results on mode locking of the laser and on optimization of the laser cavity to obtain 1.56 W of laser output.

A standing-wave acoustooptic modulator (AOM) was placed in the collimated section of the three-mirror laser cavity shown in Figure 2-7; the parameters of the three mirrors are given in Table 2-1. The pump radiation from an argon-ion-pumped, tunable Ti:Al$_2$O$_3$ laser was transmitted through the dichroic mirror (M1). A 2-mm-long Yb:YAG crystal placed at the Brewster angle in the focus between the two curved mirrors (M2 and M3) absorbed 90% of the incident pump radiation. The heat generated in the crystal was conducted through one edge into a water-cooled copper heat sink. The angle of incidence on the folding mirror was adjusted to 9° to compensate for 1.03-μm astigmatism caused by the Brewster-angle crystal. We made no attempt to introduce astigmatism into the pump beam to compensate for the astigmatism introduced in the focusing. This cavity arrangement was constrained by available optics, by a desire to have a low threshold, and by a cavity length consistent with a free spectral range equal to the mode-locked repetition rate of 246 MHz.

18
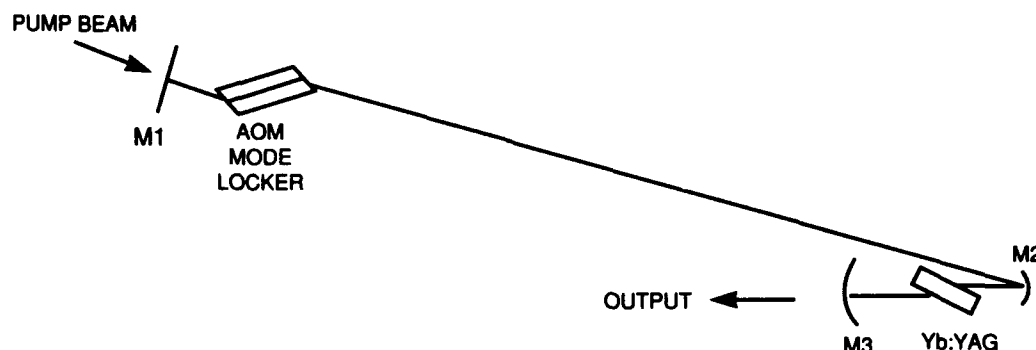
Figure 2-7. Schematic of the Yb:YAG mode-locked laser.

TABLE 2-1
Mirror Parameters for the Yb:YAG Mode-Locked Laser

Mirror	Reflectivity at 940 nm (%)	Reflectivity at 1030 nm (%)	Radius of Curvature (cm)
M1	10	99	∞
M2	99	99	6.7
M3	90	90	5

The AOM caused the cavity loss to be modulated at a frequency of 246 MHz. With 1.3 W from the Ti:Al$_2$O$_3$ laser incident on the laser cavity, 0.39 W of average mode-locked output power was obtained. During this measurement the Yb:YAG crystal was unintentionally not oriented at the Brewster angle, so much of the intracavity light was reflected off the Yb:YAG crystal. Later measurements without mode locking indicated that adjustment of the Yb:YAG crystal would have generated ~ 0.53 W of mode-locked power at 1.3-W pump power level. This output power is consistent with the 0.72 W obtained when the mode locker was not in the cavity; the difference is caused primarily by the AOM diffracting 20% of the pump light out of the pump beam.

The spectral bandwidth was broadened from 3 GHz for the free-running laser to 7 GHz for the mode-locked laser. Mode locking also stabilized the individual mode intensities. The pulse duration, as

measured with a fast photodiode and sampling oscilloscope, was 80 ps. The pulses were much longer than the 20 ps expected from the mode-locking theory for a homogeneously broadened transition. We are currently investigating this discrepancy.

Further work on the free-running laser has shown that with 2.9 W of pump power from the Ti:Al$_2$O$_3$ laser, 1.56 W of output power can be obtained. We believe this is the highest reported output power from a Yb:YAG laser.

<div align="right">
S. R. Henion

P. A. Schulz
</div>

2.5 MODELING OF ENERGY STORAGE Yb:YAG LASERS AND AMPLIFIERS

Diode lasers as pump sources for solid state lasers provide much higher pumping intensity than flashlamps, because of their spatial and spectral brightness [11]. This high brightness has allowed the demonstration of efficient room-temperature operation of solid state lasers on laser transitions that have significant thermal population in the lower laser level, such as the $^2F_{5/2}$-$^2F_{7/2}$ transition in Yb^{3+} [10]. Here, the pumping of energy storage devices is modeled, and it is shown that efficient Yb:YAG Q-switched and short-pulse amplifiers are possible.

The Yb:YAG laser design is significantly different from designs for Nd^{3+} lasers operating at 1.06 μm. In four-level Nd^{3+} lasers, the gain element can be made arbitrarily thick to absorb all the pump energy and still have good extraction. However, in quasi-three-level lasers such as Yb:YAG, arbitrarily thick elements cannot be used because in regions where the pump intensity is low the population inversion would not be achieved, but the thickness must be sufficient to allow efficient absorption.

To evaluate this problem, consider the energy level scheme of Figure 2-8. In this analysis the pump radiation is taken to be uniform in the transverse dimensions, and both single-pass and double-pass pumping are considered. Rapid thermalization of the levels within each manifold is assumed so that the relative populations of the levels within a manifold can be taken to be in Boltzmann equilibrium. The rate equations can be written in normalized form as

$$\frac{\partial \phi^\pm}{\partial \zeta} = \mp[1 - \beta(1 + f')]\phi^\pm(\zeta, t') \tag{2.1a}$$

and

$$\frac{\partial \beta}{\partial t'} = [1 - \beta(1 + f')][\phi^+(\zeta, t') + \phi^-(\zeta, t')] - \beta(\zeta, t') \quad . \tag{2.1b}$$

The term $\beta(\zeta, t')$ is the fraction of the total population in the upper manifold, and f' is equal to f_b'/f_a' where f_a' and f_b' are the Boltzmann occupation factors for the lower and upper levels of the pump transition within the lower and upper manifolds, respectively. Time has been normalized with respect to the upper manifold lifetime. The distance along the propagation direction ζ has been normalized to the absorption length at the pump wavelength. The term $\phi^\pm$ is the pump intensity in the forward and backward
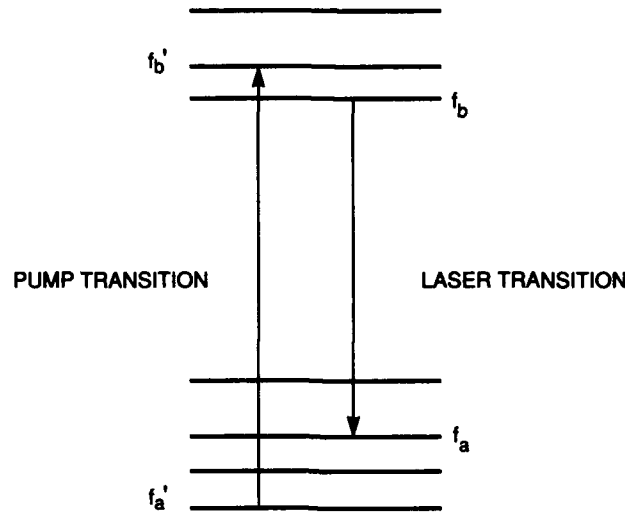
Figure 2-8. Energy level diagram showing the upper and lower manifolds of Yb^{3+} and the pump and laser transitions.

directions normalized to the saturation intensity at the pump wavelength. Similar equations can be found in an analysis by Krupke and Chase [12], *except they explicitly considered only* $f_b' = 0$, as is appropriate for 0.81-μm-pumped Nd^{3+} lasers; Yb^{3+} lasers do not satisfy $f_b' = 0$.

An important quantity is the net pump quantum efficiency η_{NP}, the ratio of the number of extractable excited states at the end of the pump pulse to the number of incident photons. Not all of the upper manifold population is extractable because of the quasi-three-level nature of the transition. This quantity η_{NP} is given by

$$\eta_{NP} = \frac{[\beta_{av}(1+f)-f]L}{\phi_0 t_p'(1+f)} \quad ,$$

(2.2)

where β_{av} is the spatially averaged normalized upper manifold population density at the end of the pump pulse, f is given by f_a/f_b where f_a and f_b are the Boltzmann occupation factors for the lower and upper levels of the laser transition within the lower and upper manifolds, respectively, L is the normalized length along the propagation direction, ϕ_0 is the normalized incident pump intensity, and t_p' is the pump pulse length in units of the upper-state lifetime.

Equation (2.1) has been solved numerically assuming that $t_p' = 0.5$ (~ 0.6 ms) for a pump pulse that is temporally a flattop, using the 300-K spectroscopic properties for 0.941- and 0.968-μm-pumped Yb:YAG. The value of η_{NP} has been calculated and is plotted in Figure 2-9 for two-pass pumping as a function of ϕ_0 and L. For $\phi_0 \approx 1$, the maximum energy storage efficiency, which is equal to the maximum value

21
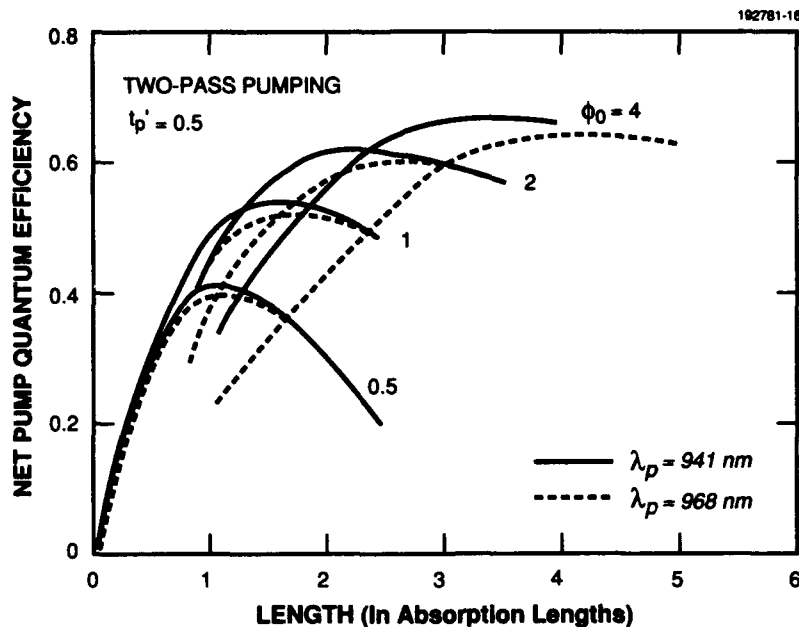
Figure 2-9. Net pump quantum efficiency of Yb:YAG laser as a function of normalized gain element length and pump intensity for two pump wavelengths.

of η_{NP} times the ratio of the output photon energy to the pump photon energy, is ~ 0.50. This value is equal to the energy storage efficiency of a 0.81-μm-pumped Nd:YAG laser if 90% of the optical power is absorbed in a 150-μs-long pump pulse. Even higher Yb:YAG energy storage efficiency (> 0.55) is predicted at $\phi_0 > 2$. Thus, the pumping models predict that Yb:YAG lasers and amplifiers operated in an energy storage mode can have optical-to-optical efficiency comparable to or exceeding that of 0.81-μm-pumped Nd:YAG lasers.

T.Y. Fan

2.6 ENERGY TRANSFER AND UPCONVERSION IN Yb:Er:YAG

Quasi-three-level laser operation has been obtained by White and Schleusener [13] in ytterbium-sensitized Er:YAG at 1.64 μm ($^4I_{13/2} - {}^4I_{15/2}$) using flashlamp pumping. Recent advances in diode laser technology, particularly the development of efficient InGaAs diodes lasing near 940 to 970 nm, suggest diode pumping Er:YAG for operation on this transition. As in the flashlamp-pumped case, high pump absorption with an erbium concentration small enough to reduce upconversion [14] might be realized with ytterbium sensitization. Previous spectroscopic studies of Yb:Er:YAG have centered on low-intensity excitation [15], where upconversion is not likely to be evident, so it is worthwhile revisiting this system under laser-pumping conditions.

The Yb-Er transfer efficiency and the Yb-Yb and Yb-Er dipole-dipole interaction strengths were determined from the time dependence of the ytterbium 1.03-μm fluorescence after short-pulse pumping. Samples of Yb:YAG (6.5 at.% Yb) without erbium doping and with 0.1, 1, and 2 at.% erbium were pumped at 941 nm using 40-ns-wide pulses from a doubled Nd:YAG-pumped Ti:Al$_2$O$_3$ laser, and the ytterbium fluorescence was detected with a silicon photodiode masked by a 1.03-μm narrow-line filter.

The Yb-Er transfer efficiency was found from the ratio of the quantum yield of the donor (ytterbium) fluorescence in the erbium-containing crystals to the quantum yield in the ytterbium-only sample. The measured transfer efficiencies are 0.76, 0.66, and 0.18 for Yb:YAG (6.5 at.% Yb) doped with 2, 1, and 0.1 at.% erbium, respectively.

Donor-donor migration can be important in ytterbium systems. The calculated probabilities for Yb-Yb and Yb-Er transfer in YAG indicate [16] that dipole-dipole interactions dominate at the average interionic distance in these samples ($\sim$ 10 Å) and that Yb-Yb transfer for this average distance could be over 20 times as likely as either fluorescent decay or Yb-Er transfer. When the donor-donor and donor-acceptor transfer are due to dipole-dipole interactions, the hopping model [17] for donor migration predicts the donor fluorescence to decay as

$$I(t) = I_0 \ \exp\left\{-\frac{t}{\tau} - \gamma\sqrt{t} - \overline{W}t\right\} \qquad , \tag{2.3}$$

where

$$\gamma = \frac{4}{3}\pi^{3/2} n_A \sqrt{C_{DA}} \tag{2.4}$$

and

$$\overline{W} = \pi(2\pi/3)^{3/2} \sqrt{C_{DA} C_{DD}} \, n_A n_D \qquad . \tag{2.5}$$

Here, τ is the fluorescence lifetime, n_D and n_A are the densities of donors and acceptors, and C_{DD} and C_{DA} are the donor-donor and donor-acceptor dipole-interaction strengths. Least-squares fits were made to the ytterbium decays for the four samples described above. The experimental value of C_{DA} is 5.5×10^{-40} cm^6 s^{-1}, in good agreement with the calculated value of 4.8×10^{-40} cm^6 s^{-1} from [16], while the experimental value of C_{DD} is 1.0×10^{-39} cm^6 s^{-1}, about 10% of the calculated value. This suggests that, for this system, the picture of donor-donor migration occurring through the dipole interaction of randomly distributed donors may not be appropriate and higher-multipole orders must be included.

Quantitative measurements of upconversion in this system were made under intense CW pumping by an argon-ion-pumped Ti:Al$_2$O$_3$ laser. The Ti:Al$_2$O$_3$ output was focused into the sample by an 8-cm-focal-length lens mounted on a set of translation stages, which permitted the intensity at the sample to be varied reproducibly over 4 orders of magnitude while maintaining constant incident power. The power transmitted through the sample was recorded so that the effects of saturation of the pump absorption could be included. The populations of the erbium $^4I_{13/2}$, $^4I_{11/2}$, and $^4S_{3/2}$ and ytterbium $^2F_{5/2}$ manifolds were
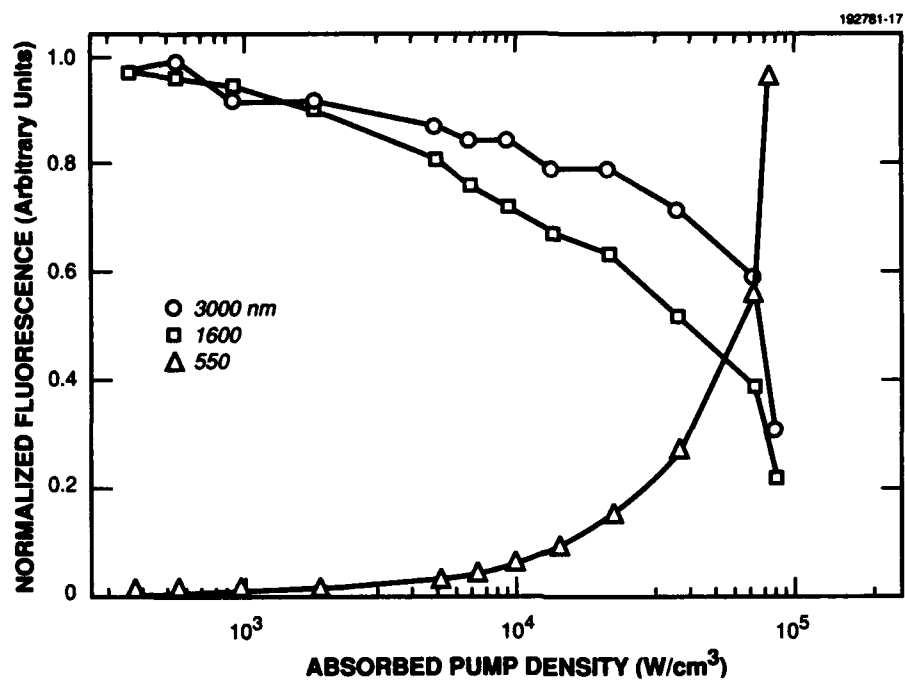
Figure 2-10. Normalized fluorescence vs absorbed pump density for Yb:Er:YAG (6.5 at.% Yb and 1 at.% Er).
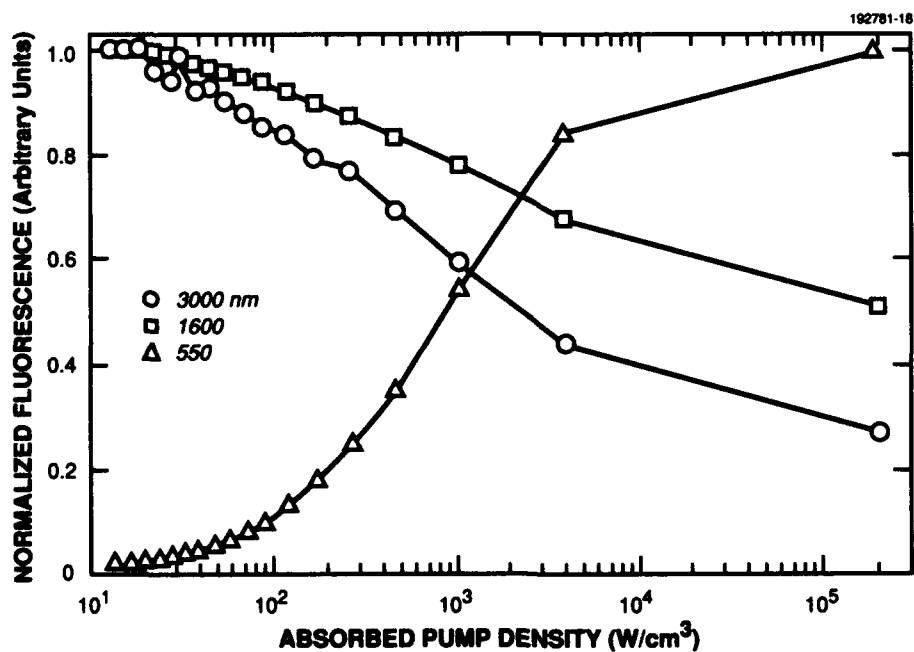
Figure 2-11. Normalized fluorescence vs absorbed pump density for Er:YAG (1 at.% Er).

24

measured by monitoring the fluorescence due to transitions to the ground state (except for the $^4I_{11/2}$, which was monitored near 3 μm for the transitions to the $^4I_{13/2}$) using appropriate combinations of detectors and filters for wavelength discrimination. The Ti:Al$_2$O$_3$ laser was mechanically chopped with a 50% duty cycle into 50-ms pulses so that the fluorescence signals could be averaged using a pair of digital oscilloscopes. The relative intensities were then measured using voltage cursors on the displays between the zero and steady state pump conditions.

Figures 2-10 and 2-11 show the normalized fluorescence vs absorbed pump density for samples of Yb:Er:YAG (6.5 at.% Yb and 1 at.% Er) and Er:YAG (1 at.% Er). The fluorescence from the $^4I_{11/2}$ and $^4I_{13/2}$ manifolds decreases substantially in both samples as the pump density is increased. The ytterbium-erbium-doped sample displays a stronger upconversion effect than the erbium-only sample and exhibits it even to pump densities about 50 times lower. Also, the $^4I_{11/2}$ fluorescence decreases more than that from the $^4I_{13/2}$, while the erbium-only sample shows the opposite behavior. Measurements on a sample of Yb:Er:YAG (6.5 at.% Yb and 0.1 at.% Er) display the same qualitative behavior as the higher-concentration Yb:Er:YAG sample with nearly the same magnitude. These results indicate that in YAG, as in many fluoride hosts [18], ytterbium participates strongly in upconversion with erbium. Rate equation analyses of this system are ongoing to help determine the relative role of Er-Er and Yb-Er interactions.

P. Lacovara

2.7 STRESSES IN LASER MATERIALS RESULTING FROM GAUSSIAN HEAT DEPOSITION

The temperature and stress distribution within laser rods, where it is assumed that the heat is generated uniformly throughout the rod, is a classic problem in laser design [19]. Of particular interest is the point at which a laser rod will fail because of those stresses. The fracture limit of a rod derived from the assumption of uniform heat generation is often used in cases where the heat deposition is clearly not uniform, such as in end-pumped rod geometries. End-pumped rod geometries are often used when the pump source for the laser is itself a laser.

A rigorous derivation of the stresses that result from the absorption of a Gaussian laser beam within a cylindrically shaped medium requires a full three-dimensional analysis and is best approached using numerical techniques. Here, the simplifying assumption is made that the heat deposition is uniform along the axis of the cylinder. This assumption is true when the absorption coefficient times the length over which absorption takes place is much less than one. This is approximately true for the case of laser diode pumping of a 1-mm-long cylinder of Nd:YAG (absorption coefficient ~ 4 cm^{-1} at 808 nm); these parameters are appropriate for a microchip laser. It will be shown that the stresses at the surface of the laser rod for the case of Gaussian heat deposition are greater than for the case of uniform heat deposition by only a factor of 2.

The temperature profile in a laser rod when heated by an incident laser beam is modeled using the following approximations. First, we assume a cylindrical geometry for the laser rod and the heat deposition. It is assumed that the heat flow is only radial, i.e., that no heat flows through the faces of the rod.

25

The axes of the laser beam and the cylinder are taken to be concentric. Finally, the Rayleigh range of the laser beam is assumed to be much larger than the length of the laser rod so that the incident laser beam is essentially collimated within the rod. The geometry for the case where the length of the rod is much smaller than the radius (a disk) is illustrated in Figure 2-12.
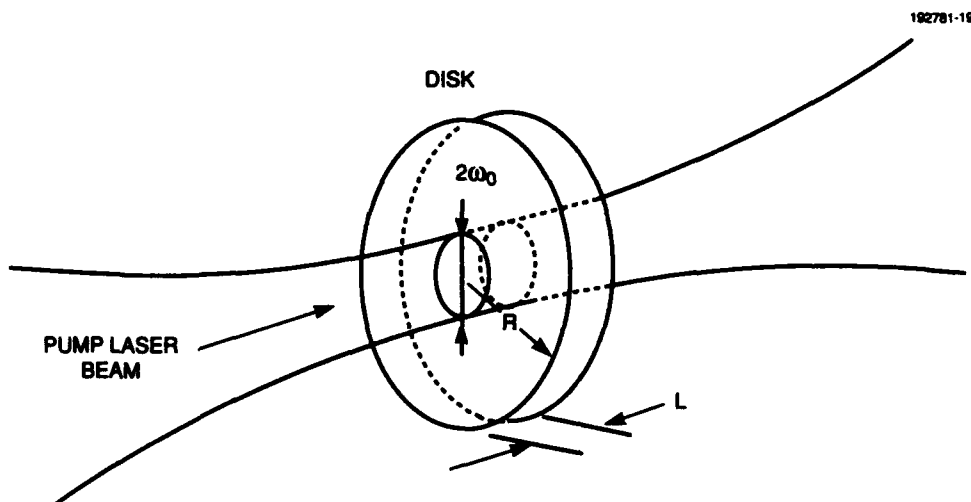
Figure 2-12. Geometry of Gaussian heat deposition in a disk-shaped medium. R is the radius of the disk, L is the length, and ω_0 is the $1/e^2$ radius of the laser beam responsible for generating the heat. It is assumed that the heat flow is only in the radial direction; no heat flows through the faces of the disk.

Having made the above simplifications, we begin the analysis with the one-dimensional heat flow equation

$$\frac{\partial Q(r,t)}{\partial t} = -K\,A\,\frac{\partial T(r,t)}{\partial r} \quad , \tag{2.6}$$

where $Q(r,t)$ is the heat energy at a radius r and time t. The heat energy deposited by a Gaussian beam per unit time is given by

$$\frac{\partial Q(r,t)}{\partial t} = P_h\left[\frac{1-e^{-2(r/\omega_0)^2}}{1-e^{-2(R/\omega_0)^2}}\right] \quad , \tag{2.7}$$

where P_h is the incident laser beam power absorbed by the laser rod resulting in the generation of heat, ω_0 is the $1/e^2$ intensity radius of the incident laser beam, and R is the radius of the laser rod. The denominator of the expression within the brackets results from the fact that the normalization is such that the integral of the right side of Equation (2.7) over the cross-sectional area of the cylinder is P_h. The area A is given by

$$A = 2\pi r L \quad , \tag{2.8}$$

where L is the length of the laser rod.

Substituting Equations (2.7) and (2.8) into Equation (2.6) yields

$$\frac{dT}{dr} = -\frac{P_h}{2\pi L K}\frac{1}{r}\left[\frac{1-e^{-2(r/\omega_0)^2}}{1-e^{-2(R/\omega_0)^2}}\right] \quad . \tag{2.9}$$

If we assume that the boundary of the laser rod is maintained at a constant temperature T_0, this equation can be integrated to yield

$$T(r) = \beta\left[E_1(\varepsilon) - E_1(\gamma) - \ln(\gamma/\varepsilon)\right] + T_0 \quad . \tag{2.10}$$

Here,

$$\beta \equiv \frac{P_h}{4\pi L K\left(1-e^{-\varepsilon}\right)} \quad , \tag{2.11}$$

$$\varepsilon \equiv 2\left(\frac{R}{\omega_0}\right)^2 \quad , \tag{2.12}$$

$$\gamma \equiv 2\left(\frac{r}{\omega_0}\right)^2 \quad , \tag{2.13}$$

and

$$E_1(z) \equiv \int_z^\infty \frac{e^{-t}}{t}dt \quad , \tag{2.14}$$

where $E_1(z)$ is an exponential integral [20]. A plot of temperature vs radius is shown in Figure 2-13 for the case where $L = 0.1$ cm, $R = 1.0$ cm, $\omega_0 = 0.1$ cm, $K = 0.13$ W/cm °C, $T_0 = 20$°C, and $P_h = 2.5$ W.
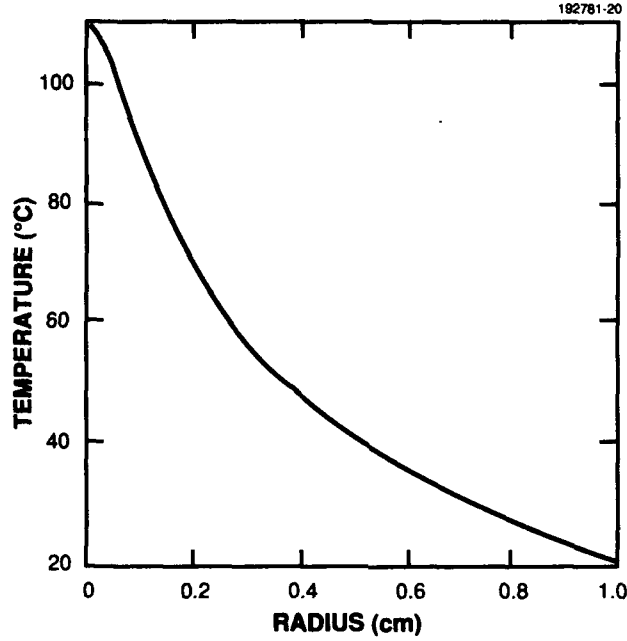
Figure 2-13. Temperature distribution resulting from Gaussian heat deposition. Equation (2.10) is plotted for the case where $L = 0.1$ cm, $R = 1.0$ cm, $\omega_0 = 0.1$ cm, $K = 0.13$ W/cm °C, $T_0 = 20°C$, and $P_h = 2.5$ W.

Once the radial dependence of the temperature is known, the stresses can be found. It is assumed that the laser rod can be treated to first approximation as an isotropic material and that $L < R$ (a disk), which corresponds to the case of plane stress if all of the surfaces are free of traction. For a temperature profile that depends only on the radial coordinate, the stresses are given by [21]

$$\sigma_r(r) = \alpha E \left[\frac{1}{R^2} \int_0^R T\, r\, dr - \frac{1}{r^2} \int_0^r T\, r\, dr \right] \tag{2.15}$$

and

$$\sigma_\phi(r) = \alpha E \left[\frac{1}{R^2} \int_0^R T\, r\, dr + \frac{1}{r^2} \int_0^r T\, r\, dr - T \right] , \tag{2.16}$$

where σ_r and σ_ϕ are the radial and azimuthal stresses, respectively, α is the coefficient of linear expansion, and E is Young's modulus. Inserting the radial temperature distribution given by Equation (2.10) into Equations (2.15) and (2.16) yields

$$\sigma_r = \frac{1}{2} \alpha E \beta \left\{ \ln(\gamma/\varepsilon) + \frac{1}{\varepsilon}\left[E_2(\varepsilon) - 1\right] - \frac{1}{\gamma}\left[E_2(\gamma) - 1\right] \right\} \tag{2.17}$$

28

$$\sigma_\phi = \frac{1}{2}\alpha E \beta \left\{ 2 + \ln(\gamma/\varepsilon) + \frac{1}{\varepsilon}\left[E_2(\varepsilon) - 1\right] + \frac{1}{\gamma}\left[E_2(\gamma) - 1\right] + 2E_1(\gamma) \right\} \quad , \tag{2.18}$$

where E_2 is another exponential integral defined [20] as

$$E_2(z) \equiv \int_1^\infty \frac{e^{-zt}}{t^2}\, dt \tag{2.19}$$

so that $E_2(z) = e^{-z} - zE_1(z)$.

Figure 2-14 shows an example of the radial dependence of the stresses for the case $L = 0.1$ cm, $R = 1.0$ cm, $\omega_0 = 0.1$ cm, $K = 0.13$ W/cm °C, $E = 2.82 \times 10^6$ kg/cm^2, $\alpha = 6.9 \times 10^{-6}$ °C^{-1}, $T_0 = 20$°C, and $P_h = 2.5$ W. The material parameters are appropriate for Nd:YAG. It can be seen that the center of the cylinder is under compression while the surface is under tension.
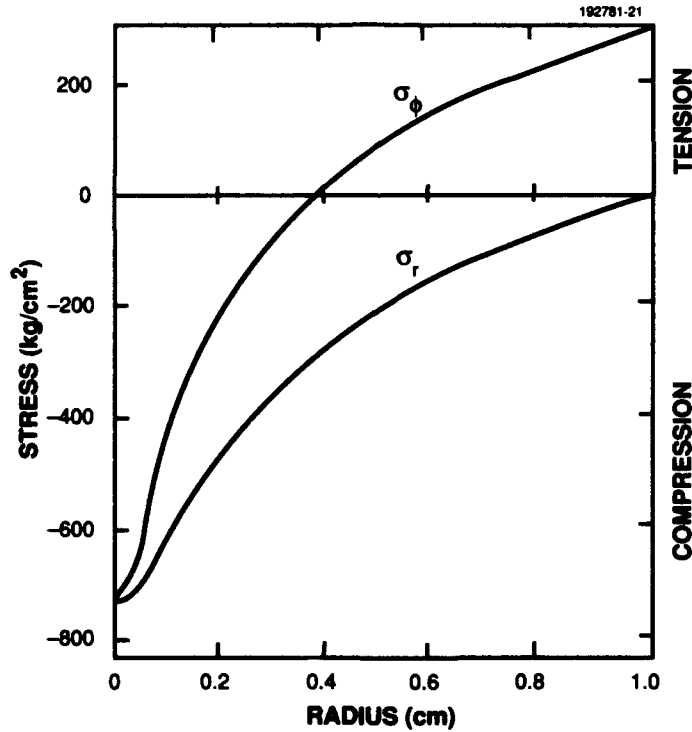
Figure 2-14. Stress distribution in a disk as a result of Gaussian heat deposition. Equations (2.17) and (2.18) are plotted for the case where $L = 0.1$ cm, $R = 1.0$ cm, $\omega_0 = 0.1$ cm, $K = 0.13$ W/cm °C, $E = 2.82 \times 10^6$ kg/cm^2, $\alpha = 6.9 \times 10^{-6}$ °C^{-1}, $T_0 = 20$°C, and $P_h = 2.5$ W. The material parameters are appropriate for Nd:YAG.
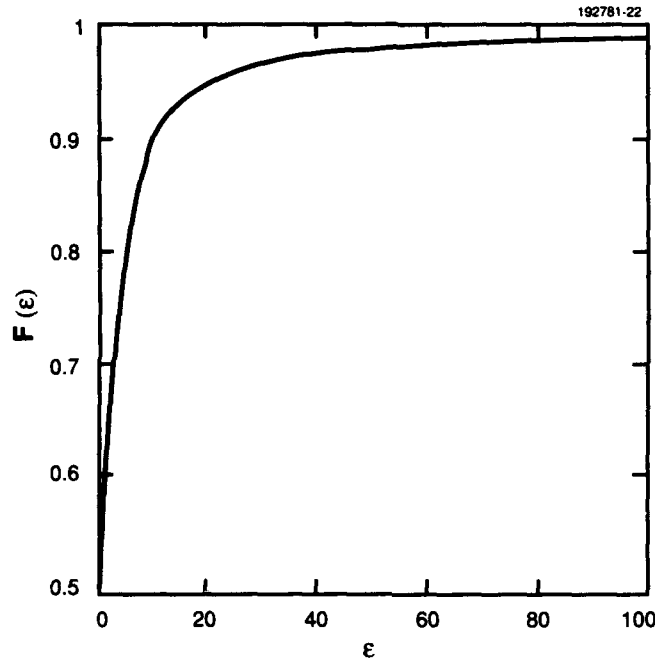
Figure 2-15. Plot of $(\varepsilon - 1 + e^{-\varepsilon})/\varepsilon(1 - e^{-\varepsilon}) \equiv F(\varepsilon)$, which corresponds to the last factor in Equation (2.20). A disk that is uniformly heated corresponds to the point $\varepsilon = 0$.

Fracture of the disk occurs when the tension exceeds that necessary to propagate the largest flaw. The maximum amount of tension occurs at the edge of the disk where typically a large number of flaws exist. The maximum surface tension σ_{max} is obtained by evaluating σ_ϕ at $r = R$. Using Equation (2.11) we have

$$\sigma_{max} = \frac{\alpha E}{4 \pi K} \frac{P_h}{L} \frac{\varepsilon - 1 + e^{-\varepsilon}}{\varepsilon\left(1 - e^{-\varepsilon}\right)} . \tag{2.20}$$

While this expression may appear complex, it should be noted that the first factor in the product contains only material parameters and the last factor is a weak function of ε, as shown in Figure 2-15. Thus, the maximum stress at the edge of the disk is proportional to the heat power per unit length deposited in the disk and varies by only a factor of 2 depending on the geometry.

K. F. Wall

2.8 HIGH-POWER, HIGH-EFFICIENCY CW ROTATING-DISK Nd:GLASS LASER

Nd:glass lasers have traditionally been limited to relatively low average powers [22] by the poor thermal conductivity of glass, which results in either physical damage or thermally induced lensing and birefringence [23]. Previously, we demonstrated the operation of the first rotating-disk Nd:glass laser [24] designed to alleviate thermal problems caused by the pump source; here we report improvements in the performance of this laser. Specifically, a Ti:Al$_2$O$_3$-laser-pumped CW rotating-disk Nd:glass laser has produced nearly 2 W of output in a TEM$_{00}$ mode.

As shown in Figure 2-16, a cylindrical disk of Nd-doped phosphate glass, 0.5 cm thick and 5 cm in diameter, was inserted at the Brewster angle into a 12-cm-long linear stable laser cavity that consisted of a high reflector M1 at 1.054 μm with a radius of curvature (RC) of 5 cm and a 1% output coupler M2, with an RC of 10 cm; the glass disk was placed 4 cm from the high reflector. The mode spot in the Nd:glass disk had an elliptical cross section, whose major and minor axes were calculated to be 404 and 220 μm (full width at $1/e^2$), respectively. The Nd:glass was end pumped through M1 by the focused output radiation from a Ti:Al$_2$O$_3$ laser. The pump spot was located 2 cm from the center of rotation of the Nd:glass disk and had an elliptical cross section of dimensions 360 × 90 μm (full width at $1/e^2$). The laser always operated in the TEM$_{00}$ mode with an output power that depended on both the pump power and the rate of rotation of the Nd:glass disk.

192781-23
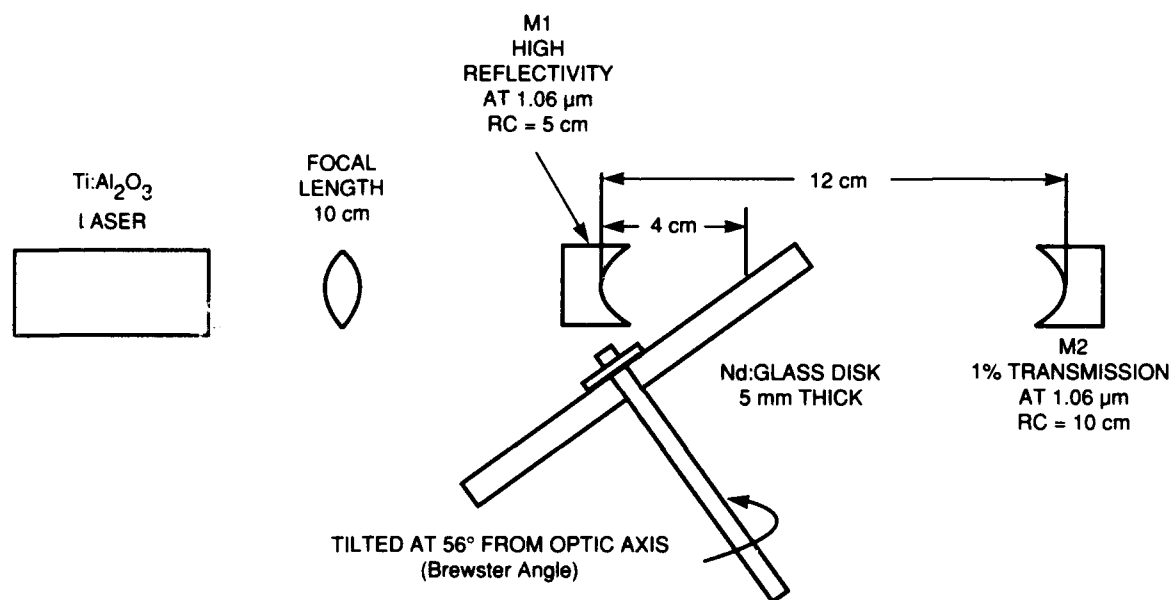
Figure 2-16. Experimental arrangement of rotating-disk Nd:glass laser. M1 is a high reflector at 1.054 μm with a 5-cm radius of curvature, and M2 is a 1% output coupler with a 10-cm radius of curvature.
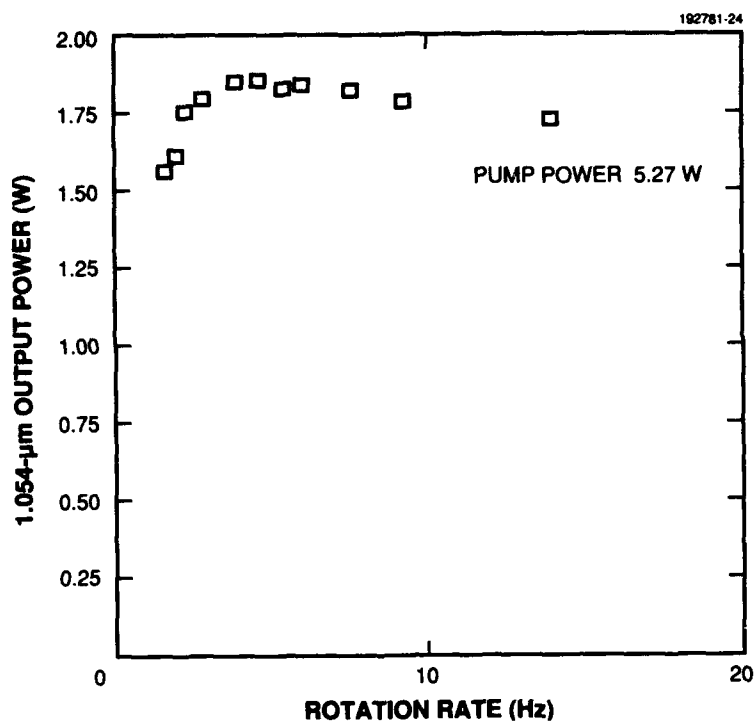
Figure 2-17. Rotating-disk Nd:glass laser output power vs rotation rate.
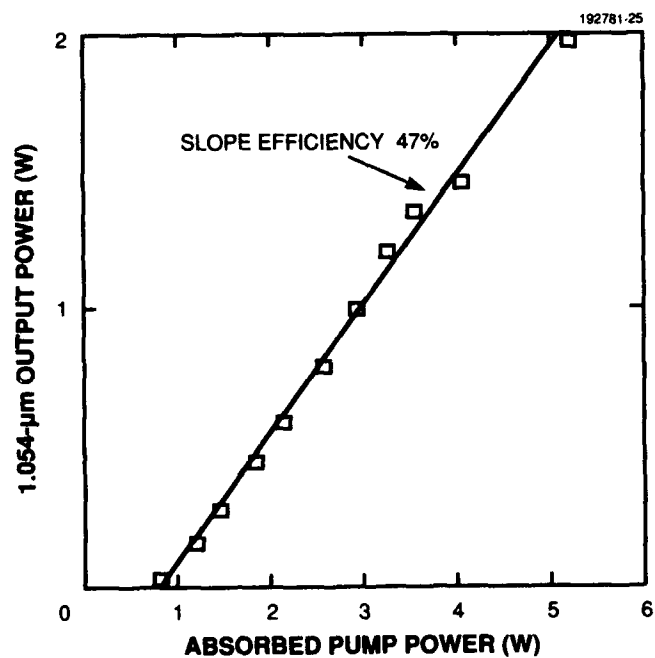
Figure 2-18. Rotating-disk Nd:glass laser output power vs pump power at a rotation rate of 6.5 Hz, which is optimized for 5.2-W pumping.

32

The graph in Figure 2-17 demonstrates that as the rate of rotation of the disk was increased from zero, the output power of the laser increased from zero to a maximum and then rolled off gradually. Initial increase in laser power with rotation rate is attributed to the distribution of the pumping heat load over a larger volume of Nd:glass, which decreases thermal effects. In contrast to our previous results [24] the roll-off at higher rotation rates is not substantial, because the stimulated emission lifetime is short compared with the time it takes to translate the excited state population out of the laser mode. Figure 2-18 shows the output power as a function of absorbed pump power for a rotation rate of 6.5 Hz. The slope efficiency is 47% and the data form a straight line, indicating that thermal degradation at 6.5 Hz was not a problem. A maximum 1.98 W of output power was obtained with an absorbed pump power of 5.2 W. This rotating-disk laser was limited only by the available pump power. We believe this to be the highest reported power for a CW Nd:glass laser operating in the TEM_{00} mode.

Substantially higher output powers should be possible from rotating-disk lasers by increasing the pump powers and by active longitudinal cooling of the disks. Higher-power Nd:glass lasers could operate over a larger spectral bandwidth than other Nd-doped crystals and should allow continuous mode-locked operation with short pulses.

<div style="text-align: center;">

J. Korn
T. Y. Fan

</div>

REFERENCES

1. J. J. Zayhowski and A. Mooradian, *Opt. Lett.* **14**, 24 (1989).

2. J. Ochoa, unpublished.

3. J. J. Zayhowski, *IEEE J. Quantum Electron.* **26**, 2052 (1990); *Opt. Lett.* **15**, 431 (1990).

4. J. J. Zayhowski, *Opt. Lett.* **16**, 575 (1991).

5. J. J. Zayhowski and P. L. Kelley, *IEEE J. Quantum Electron.* **27**, 2220 (1991).

6. B. Zhou, T. J. Kane, G. J. Dixon, and R. L. Byer, *Opt. Lett.* **10**, 62 (1985).

7. A. Owyoung, G. R. Hadley, P. Esherick, R. L. Schmitt, and L. A. Rahn, *Opt. Lett.* **10**, 484 (1985).

8. J. J. Zayhowski, *OSA Proc. Advanced Solid-State Lasers* **6**, 9 (1991).

9. Solid State Research Report, Lincoln Laboratory, MIT, 1990:2, p. 23.

10. P. Lacovara, H. K. Choi, C. A. Wang, R. L. Aggarwal, and T. Y. Fan, *Opt. Lett.* **16**, 1089 (1991).

11. T. Y. Fan and A. Sanchez, *IEEE J. Quantum Electron.* **26**, 311 (1990).

12. W. F. Krupke and L. L. Chase, *Opt. Quantum Electron.* **22**, S1 (1990).

13. K. O. White and S. A. Schleusener, *Appl. Phys. Lett.* **21**, 419 (1972).

14. D. K. Killinger, in *Conf. Lasers Electro-Optics Tech. Dig.* (Optical Society of America, Washington, D.C., 1987), Paper THJ4.

15. D. Pacheco and B. DiBartolo, *J. Lumin.* **14**, 19 (1976).

16. P. Lacovara, Ph.D. thesis, Boston College, 1992.

17. Y. K. Voron'ko, T. G. Mamedov, V. V. Osiko, M. I. Timoshechkin, and I. A. Shcherbakov, *Sov. Phys. JETP* **38**, 565 (1974).

18. L. F. Johnson, H. J. Guggenheim, T. C. Rich, and F. W. Ostermayer, *J. Appl. Phys.* **43**, 1125 (1972).

19. W. Koechner, *Solid-State Laser Engineering* (Springer, Berlin, 1988), pp. 350-355.

20. M. Abramowitz and I. A. Stegun, *Handbook of Mathematical Functions* (Dover, New York, 1965), p. 228.

21. B. Boley and J. Weiner, *Theory of Thermal Stresses* (Wiley, New York, 1960), pp. 288-291.

22. T. Dimmick, *Opt. Lett.* **15**, 177 (1990).

23. F. Krauz, E. Winter, A. Schmidt, and A. Dienes, *IEEE J. Quantum Electron.* **26**, 158 (1990).

24. J. Korn, T. H. Jeys, and T. Y. Fan, *Advanced Solid-State Lasers 1991 Tech. Dig. Ser.* (Optical Society of America, Washington, D.C., 1991), p. 188.

3. MATERIALS RESEARCH

3.1 InAsSb/AlAsSb DIODE LASERS EMITTING AT 4 μm

Diode lasers incorporating a GaInAsSb active layer and AlGaAsSb confining layers lattice matched to a GaSb substrate are being developed to provide emission in the 2- to 5-μm spectral range for such applications as laser radar, optical communications, remote sensing, and molecular spectroscopy. We recently reported [1] the CW operation at temperatures up to 30°C of gain-guided double-heterostructure $Ga_{0.84}In_{0.16}As_{0.14}Sb_{0.86}/Al_{0.75}Ga_{0.25}As_{0.06}Sb_{0.94}$ lasers emitting at ~ 2.2 μm. These devices, which were grown by molecular beam epitaxy (MBE) on GaSb substrates, exhibited room-temperature pulsed threshold current densities J_{th} as low as 0.94 kA cm^{-2}, the lowest value for any diode laser emitting beyond 2 μm. We now report the fabrication of double-heterostructure InAsSb/AlAsSb diode lasers, also grown by MBE on GaSb substrates, that emit at 4.0 μm. These devices have exhibited CW operation up to 80 K and pulsed operation up to 155 K. The only III-V diode lasers with a longer emission wavelength are InSb devices that emitted at 5.2 μm but were operated only up to 10 K.

The InAsSb and AlAsSb layers were grown in the manner described previously for GaInAsSb and AlGaAsSb layers [2], except that a valved effusion cell was used for the As source. The reflection high-energy electron diffraction patterns observed during growth were sharp and well streaked, indicating that the microscopic surface structure was smooth and highly ordered. The InAsSb and AlAsSb surfaces exhibited group-V-stabilized 3 × 1 and 4 × 2 reconstructions, respectively. The intended compositions of the active and cladding layers were $InAs_{0.91}Sb_{0.09}$ and $AlAs_{0.08}Sb_{0.92}$, respectively. The $InAs_{0.91}Sb_{0.09}$ alloy has nearly the lowest bandgap of the GaInAsSb alloys that are lattice matched to GaSb. The $AlAs_{0.08}Sb_{0.92}$ alloy has the highest bandgap and lowest refractive index of the lattice-matched AlGaAsSb alloys, so it can provide the best electrical and optical confinement.

The laser structure consists of the following layers: 0.5-μm-thick n-GaSb buffer, 3-μm-thick n-AlAsSb cladding, 0.8-μm-thick nominally undoped InAsSb active, 3-μm-thick p-AlAsSb cladding, and 0.075-μm-thick p^+-GaSb cap. The carrier densities at 300 K in n- and p-AlAsSb test layers were ~ 2 × 10^{17} and ~ 2 × 10^{16} cm^{-3}, respectively. Two wafers, designated A and B, were grown with this structure. The peak wavelengths of photoluminescence spectra measured at 4.5 K for these wafers were 3.72 and 3.97 μm, respectively, which correspond to active-layer bandgaps of 0.333 and 0.312 eV. These values indicate that the As content of the active layer is higher for wafer A than for wafer B, and that both active layers have a higher As content than $InAs_{0.91}Sb_{0.09}$, for which the calculated bandgap at 0 K is 0.296 eV.

To fabricate gain-guided lasers, 100-μm-wide Ti/Au stripes were defined on the p^+-GaSb cap by a photoresist lift-off process. Mesas were formed by etching the p^+-GaSb and p-AlAsSb layers to a depth of ~ 0.2 μm. The wafers were lapped from the substrate side to a thickness of ~ 100 μm. Ohmic contact to the n-GaSb was obtained by depositing Au/Sn/Ni/Ti/Au and alloying at 300°C. Each wafer was then cleaved to form lasers with a cavity length of 300 μm. Individual devices were mounted p-side up on Cu heatsinks and installed in a Dewar for low-temperature operation.
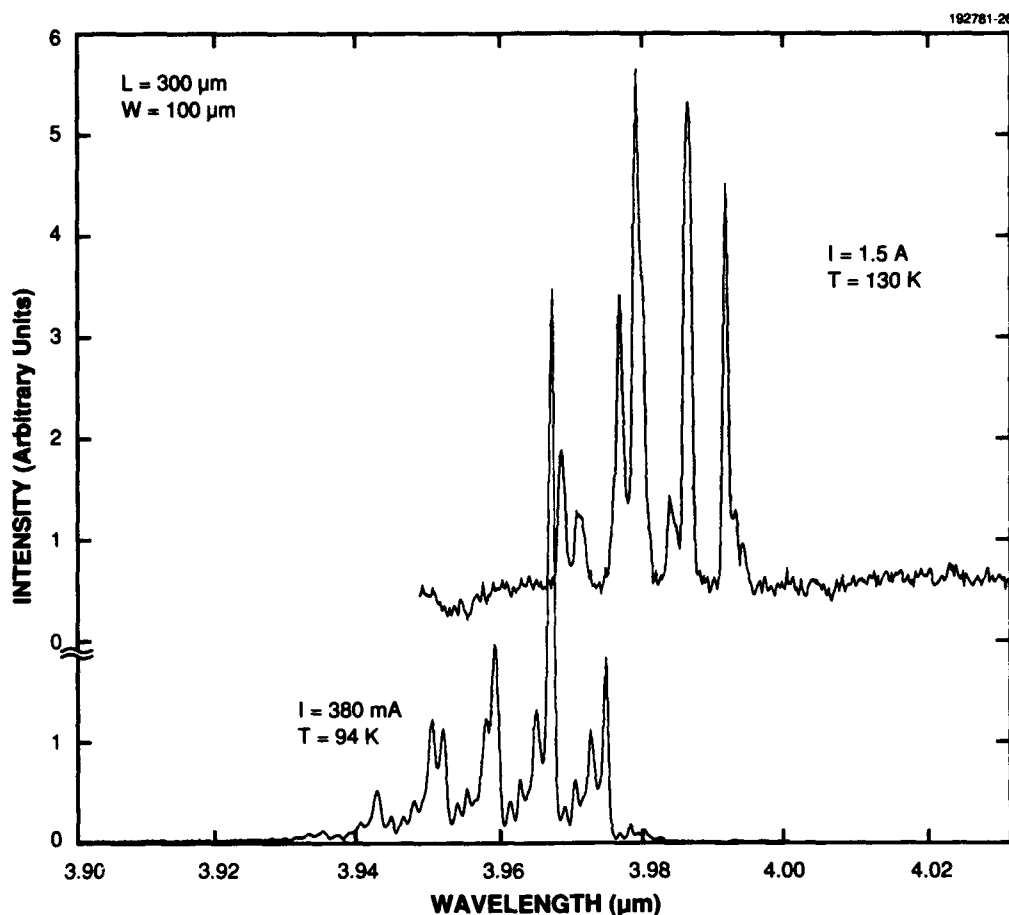
Figure 3-1. Emission spectra at 94 and 130 K for pulsed operation of InAsSb/AlAsSb double-heterostructure diode laser.

Figure 3-1 shows the emission spectra obtained for pulsed operation of a laser from wafer B at 94 and 130 K. Both spectra exhibit multiple longitudinal modes separated by ~ 7.5 nm and multiple lateral modes separated by ~ 1.5 nm. The emission peaks at 3.97 μm for 94 K and at 3.98 μm for 130 K. For a laser from wafer A, the emission at 90 K peaked at 3.71 μm. The difference between the laser emission wavelengths of the two wafers at ~ 90 K is the same as the difference between their photoluminescence (PL) wavelengths at 4.5 K. For each wafer, from the difference between the laser emission and PL wavelengths, together with the calculated change in bandgap with temperature, it is found that bandfilling of 13 meV occurs during laser operation at ~ 90 K.
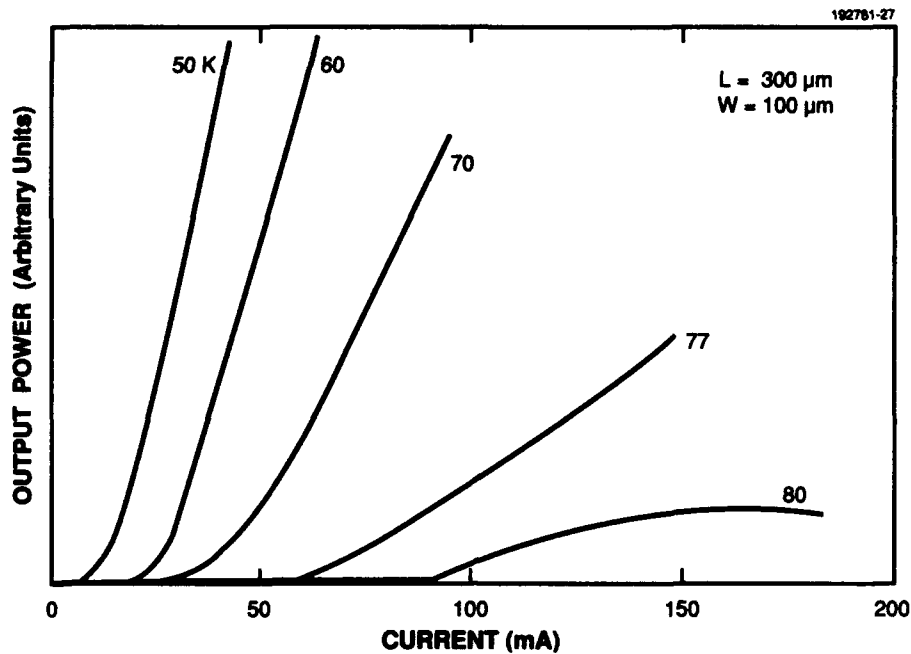
Figure 3-2. Light output vs current for CW operation of InAsSb/AlAsSb diode laser at several heatsink temperatures.

The light output vs current (L-I) curves shown in Figure 3-2 were obtained for CW operation of a laser from wafer B at heatsink temperatures from 50 to 80 K. Although we have not yet assembled the apparatus required for measuring the total output power emitted by lasers mounted in a Dewar, it is estimated that power levels of a few milliwatts have been achieved at the lower temperatures. Figure 3-3 shows the temperature dependence of the values of J_{th} obtained from the L-I curves for pulsed operation of lasers from wafers A and B. For the device from wafer A, pulsed operation was obtained up to 115 K, J_{th} = 180 A cm^{-2} at 50 K, and the characteristic temperature T_0 = 23 K. For the device from wafer B, the corresponding values are 155 K, 33 A cm^{-2}, and 17 K. The low T_0 values suggest that loss mechanisms such as Auger recombination and diffusion of carriers out of the active region are considerably more important for these devices than for double-heterostructure GaInAsSb/AlGaAsSb lasers emitting at ~ 2.2 μm, which have T_0 values of ~ 50 K at room temperature.

S. J. Eglash   W. L. McGilvary
H. K. Choi   J. V. Pantano
G. W. Turner   J. W. Chludzinski
D. F. Kolesar   M. K. Connors

37
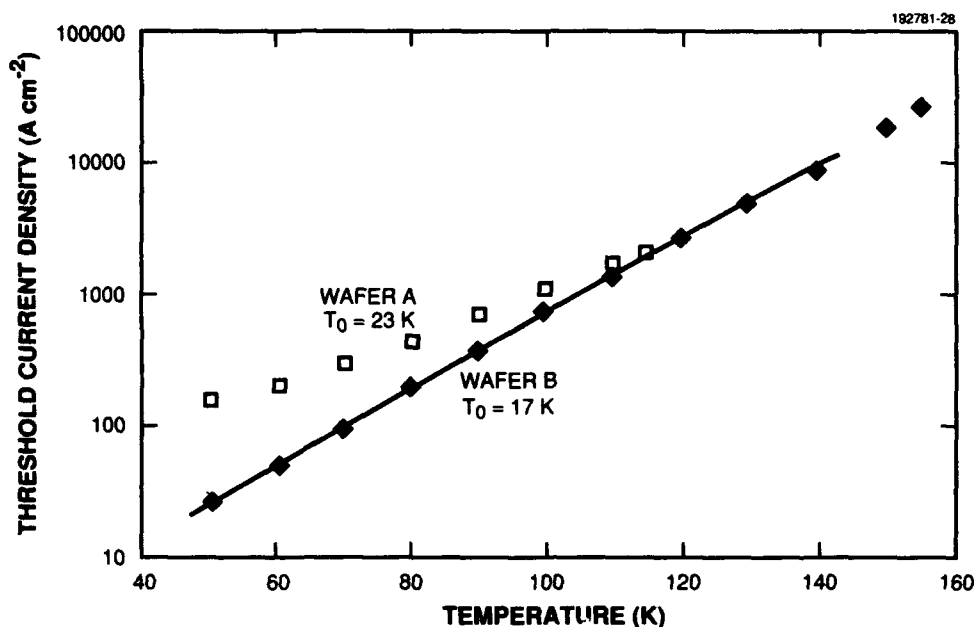
Figure 3-3. Pulsed threshold current density vs temperature for InAsSb/AlAsSb diode lasers from two different wafers.

3.2 VAPOR ETCHING OF GaAs AND AlGaAs BY CH_3I

Development of a more satisfactory process for vapor etching of GaAs and AlGaAs alloys in organo-metallic vapor phase epitaxy (OMVPE) reactors could significantly advance the technology available for fabricating optoelectronic devices. The use of such a process for in situ wafer patterning and cleaning would permit OMVPE to be employed more conveniently in the fabrication of GaAs/AlGaAs devices, such as buried-heterostructure and distributed-feedback diode lasers, that require two epitaxial growth steps inter-rupted by a patterning/etching step. Currently, the employment of OMVPE for such devices is limited because the oxide formed on AlGaAs surfaces exposed to air prevents high-quality regrowth.

Studies of the vapor etching of GaAs by HCl, $AsCl_3$, HBr, and $AsBr_3$ and of AlGaAs by HCl have been reported. In all cases, etching temperatures above 750°C were required in order to maintain specular surface morphology. Dopant and/or alloy interdiffusion occurring at such high temperatures could degrade the performance of some types of devices. Furthermore, HCl and HBr are corrosive gases that could cause system contamination. Consequently, in situ vapor etching is infrequently used in OMVPE processing.

We have recently reported [3] initial experiments on the vapor etching of GaAs substrates with an alternative etchant, methyl iodide (CH_3I), that is potentially useful in OMVPE systems because it is liquid at room temperature, has a suitable vapor pressure, and is noncorrosive. It was found that featureless surface morphology can be maintained with this etchant at temperatures of only 450 to 500°C. We have now made a more detailed study of the etch rate and morphology for GaAs substrates and for $Al_xGa_{1-x}As$ epilayers with x up to 0.7. On the basis of the results, we believe that etching with CH_3I vapor is a promising process for in situ treatment of GaAs/AlGaAs structures in OMVPE reactors.

38

The etching experiments were performed in a horizontal reactor operated at atmospheric pressure with H_2 or He as the carrier gas. The total flow rate through the reactor ranged from 0.5 to 5 slpm. By flowing part of the carrier gas through the CH_3I bubbler maintained at temperatures between 2 and 18°C, values of CH_3I concentration y_{CH_3I} ranging from 0.0012 to 0.03 mole fraction could be obtained. The GaAs samples were Si-doped n^+ (100) wafers that were partially masked with silicon nitride. The AlGaAs samples were nominally undoped 2-μm-thick epilayers that were grown on a GaAs substrate by OMVPE in a separate reactor, capped with 500 Å of GaAs, and then partially masked with silicon nitride. Before CH_3I etching, each sample wafer was first degreased, cleaned successively with concentrated H_2SO_4 and concentrated HCl, rinsed in deionized water, and finally dried with N_2 gas. The wafer was then placed on a Mo susceptor in the etching reactor. The reactor was purged with H_2 for 30 min, the susceptor was heated to the desired etching temperature, and CH_3I was switched in for a given length of time. The reactor was then purged with H_2 and cooled to room temperature. The silicon nitride mask was removed from GaAs samples by etching with HF and from AlGaAs samples by CF_4 plasma etching. The step height was then measured with a mechanical stylus, and the etch rate was found by dividing the step height by the exposure time.

Figure 3-4 shows the measured etch rate r of GaAs as a function of reciprocal absolute temperature for susceptor temperatures from 400 to 625°C and y_{CH_3I} values of 0.0012, 0.0058, and 0.015 mole fraction in H_2 carrier gas at a flow rate of 2.1 slpm. For $y_{CH_3I} = 0.015$ mole fraction, r increased from
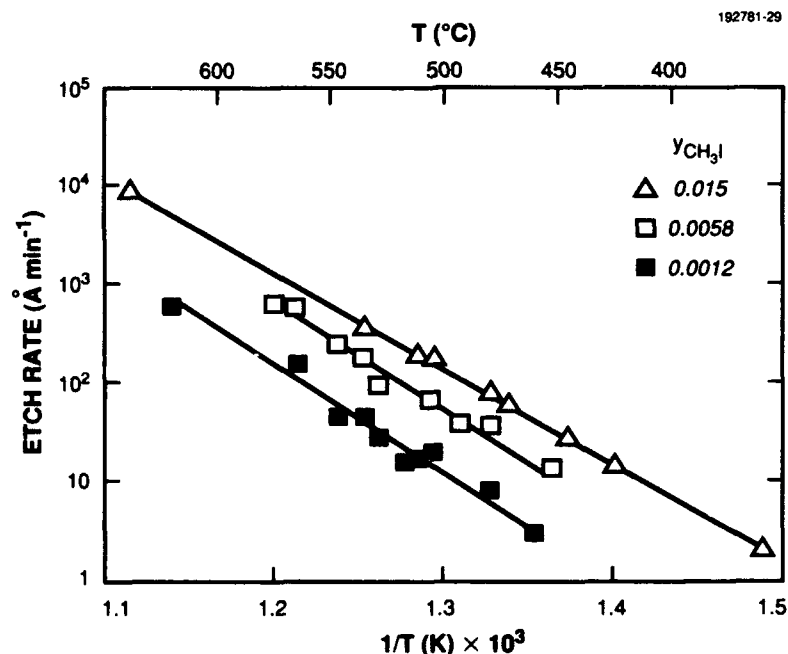
Figure 3-4. Etch rate of GaAs as a function of temperature for three concentrations of CH_3I in H_2 carrier gas at a flow rate of 2.1 slpm.

2.5 Å min^{-1} at 400°C to 9000 Å min^{-1} at 625°C. For each CH_3I concentration, a good fit to the data is given by a straight line whose slope corresponds to an activation energy of 45 ± 2 kcal mol^{-1}. Using He instead of H_2 as the carrier gas decreased r by a factor of 1.5 but did not affect the activation energy. Figure 3-5 shows the dependence of r on y_{CH_3I} at 480, 500, and 525°C, again with H_2 carrier gas at a flow rate of 2.1 slpm. For each susceptor temperature, the data are well fitted by a curve given by the expression $r = \text{const} \, (y_{CH_3I})^n$, where the reaction order $n = 0.83 \pm 0.03$.
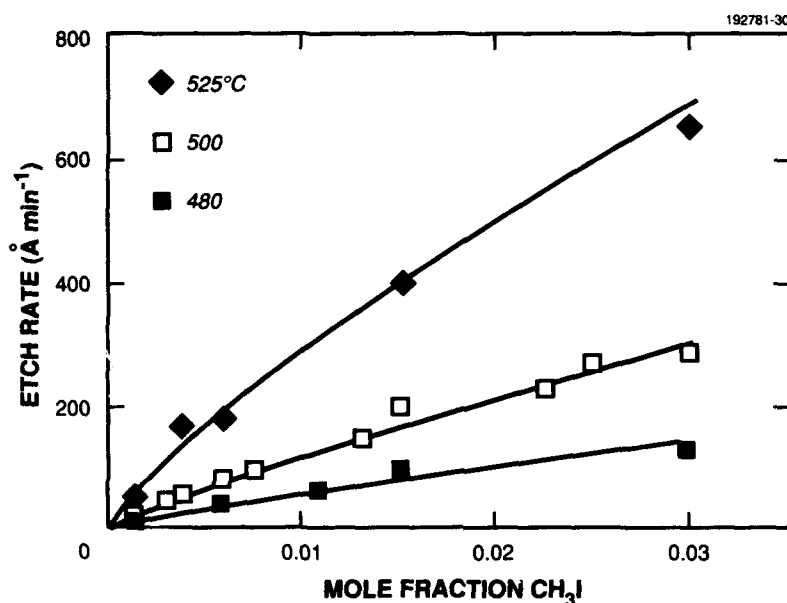
Figure 3-5. Etch rate of GaAs at three temperatures as a function of CH_3I concentration in H_2 carrier gas at a flow rate of 2.1 slpm.

The data of Figures 3-4 and 3-5 can be represented by the expression

$$r = k_0 \, y_{CH_3I}^{0.83} \exp\left(-45 \, \text{kcal mol}^{-1}/RT\right) , \tag{3.1}$$

where R is the gas constant, T is the absolute temperature, and $k_0 = 3.2 \times 10^{16}$ Å min^{-1}. The activation energy for the unimolecular gas-phase decomposition of CH_3I to CH_3 and I is reported to be 43.5 kcal mol^{-1} [4]. The agreement between this value and the activation energy of 45 kcal mol^{-1} in Equation (3.1) indicates that the decomposition reaction is the principal rate-controlling step in the etching process, although the slightly sublinear dependence of r on y_{CH_3I} indicates that the etching rate is also influenced

by some other factor. The value of k_0 in Equation (3.1) depends upon a number of experimental conditions, including reactor geometry, total gas pressure, carrier gas species, and carrier gas flow rate. The reduction in r obtained by changing the carrier gas from H_2 to He was noted above. Figure 3-6 shows the dependence of r on H_2 flow rate for $y_{CH_3I} = 0.015$ mole fraction and a susceptor temperature of 485°C. The value of r decreases from 190 Å min^{-1} at 0.5 slpm to 70 Å min^{-1} at 5 slpm. The data are fitted by a power law expression with an exponent of –0.44. By decreasing the residence time of the CH_3I molecules in the high-temperature region adjacent to the susceptor, an increase in flow rate tends to reduce the decomposition rate and therefore the etching rate, as observed. To explain the quantitative dependence of r on flow rate, it is also necessary to take account of the effect of the flow rate on the temperature profile in the gas phase and on the thickness of the diffusion boundary layer adjacent to the wafer surface, which influence the CH_3I decomposition rate and the rate at which the decomposition products are transported to the surface.

To investigate the etching of $Al_xGa_{1-x}As$ alloys with CH_3I vapor, a GaAs control wafer and epilayers with $x = 0.1$, 0.3, and 0.7 were etched at 480°C with $y_{CH_3I} = 0.015$ mole fraction and a H_2 flow rate of 2.1 slpm. As shown in Figure 3-7, under these conditions r was the same over the entire composition range. This result is consistent with control of the etching rate by the gas-phase decomposition of CH_3I and transport of the decomposition products to the sample surface.
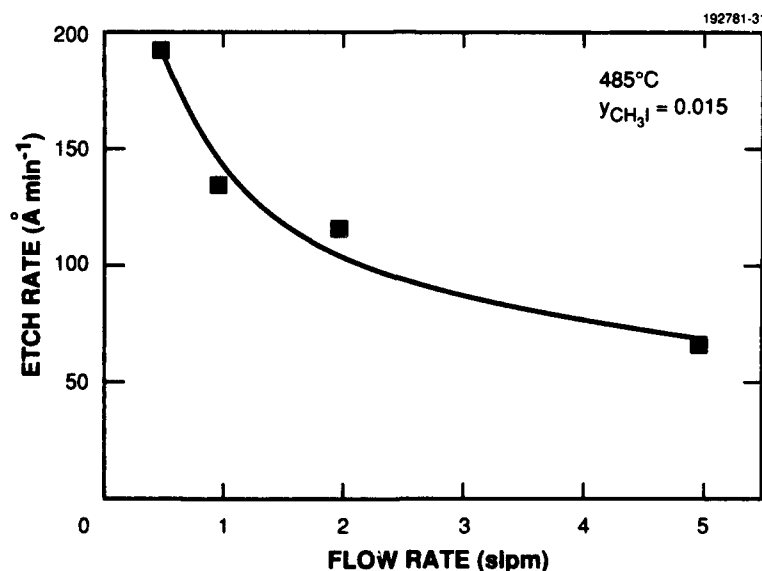
Figure 3-6. Etch rate of GaAs vs flow rate of H_2 carrier gas for CH_3I mole fraction of 0.015 and temperature of 485°C.
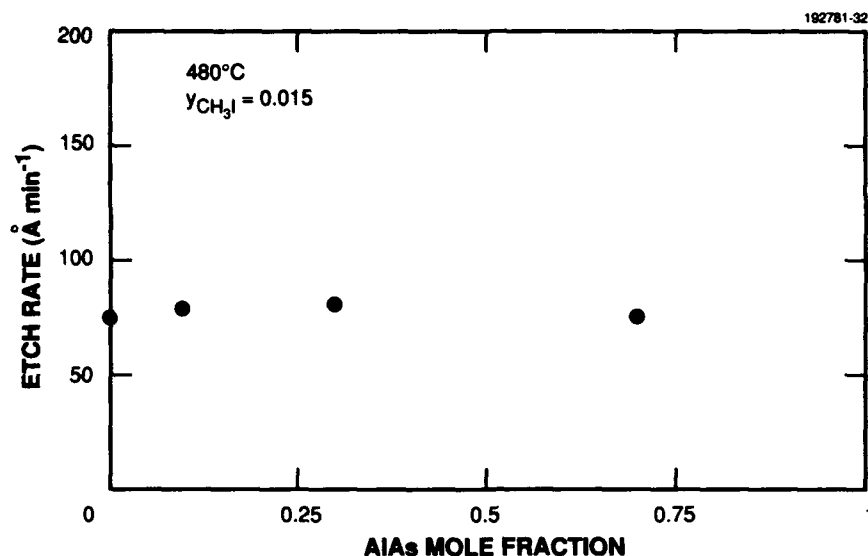
Figure 3-7. Etch rate of $Al_xGa_{1-x}As$ vs x for a temperature of 480°C and CH_3I mole fraction of 0.015 in H_2 carrier gas at a flow rate of 2.1 slpm.

Some but not all of the GaAs etching experiments discussed above yielded surfaces that were smooth and featureless as observed by Nomarski interference microscopy. In these and supplementary experiments it was found that the surface morphology generally improved with decreasing temperature for fixed y_{CH_3I} and etch depth, and with increasing y_{CH_3I} for fixed temperature and depth. Specular surface morphology was maintained at temperatures of 480°C and below for etching times up to 1 h (depths up to 0.9 μm) and at 500°C for times up to 15 min (depths up to 0.5 μm). Above 520°C, surfaces were generally degraded in times as short as 5 min (depths as small as 0.35 μm).

C. A. Wang
C. W. Krueger

REFERENCES

1. H. K. Choi and S. J. Eglash, *Appl. Phys. Lett.* **59**, 1165 (1991).

2. S. J. Eglash, H. K. Choi, and G. W. Turner, *J. Cryst. Growth* **111**, 669 (1991).

3. C. W. Krueger, M. Flytzani-Stephanopoulos, R. A. Brown, and C. A. Wang, presented at Electronic Materials Conf., Santa Barbara, Calif., 27-29 June 1990.

4. K. Saito, H. Tahara, O. Kondo, T. Yokubo, T. Higashihara, and I. Murakami, *Bull. Chem. Soc. Jpn.* **53**, 1335 (1980).

4. SUBMICROMETER TECHNOLOGY

4.1 DEPENDENCE OF RESIDUAL IMPURITY CONCENTRATION ON ARSINE PYROLYSIS TEMPERATURE IN GAS-SOURCE MOLECULAR BEAM EPITAXY OF GaAs FILMS

Gas-source molecular beam epitaxy (MBE) of III-V compound semiconductors is a growth technique that employs elemental effusion sources for the group III cations and for dopants and uses such gas sources as arsine and phosphine for the group V anions. Arsine (or phosphine) is typically injected through a pyrolysis furnace and cracked to yield molecular fragments containing arsine and hydrogen. By prepyrolyzing arsine, rather than relying on its decomposition on the GaAs surface during growth, a lower substrate temperature can be used. This allows a greater control of the MBE growth chemistry. The residual impurity concentration, as determined from Hall effect measurements, is a strong function of the cracking temperature of the arsine [1]. Films are generally n-type and exhibit a decreasing residual impurity concentration with decreasing cracker temperature. This dependence has been attributed to impurities from the cracker [1], to variations in the molecular fragment distribution that influence the growth chemistry [2], and in particular to the presence of the arsine radical AsH on the growth surface [1],[3]. This radical is thought to play a role in the scavenging of carbon, the residual impurity found in solid-source MBE systems, from the growth surface. Gas-source MBE has produced the highest-purity epitaxial GaAs ($n_{70K} \approx 3 \times 10^{13}$ cm^{-3}, $\mu_{70K} = 2.8 \times 10^5$ cm^2/V s) [3] ever grown.

Here, we report on an initial set of growths using arsine in a turbomolecular-pumped gas-source MBE system. We observe the expected residual impurity concentration dependence on cracker temperature. An examination of the Hall effect measurements and the 4-K photoluminescence spectra of the samples points to a reduction of both a donor impurity and an acceptor impurity with decreasing cracker temperature. The acceptor impurity at the highest cracker temperature studied (1000°C) is equal to that for material grown in the same system using a solid arsenic source and decreases with lower cracker temperature. This indicates that either the solid arsenic is a source of carbon or that the arsine radicals interact with the carbon to reduce its incorporation on the GaAs surface during a growth.

The growths were made using a Varian gas-source MBE system that has both solid arsenic and 100% arsine for group V sources. The system can be pumped by either an ion pump or a turbomolecular pump backed by a dry roughing-pump system. The GaAs layers were grown on a (100) semi-insulating GaAs substrate at a substrate temperature of 620°C, a growth rate of 1 μm/h, and a substrate revolution rate of 5 rpm. Table 4-1 summarizes the growth data and Hall measurement results for four arsine runs; the results for a growth with solid arsenic in the same system (run 38), which was intentionally doped with silicon, are shown for comparison with the unintentionally doped arsine runs. The Hall mobilities and carrier concentrations are corrected for surface and substrate depletion effects. The donor concentration N_D and acceptor concentration N_A are calculated using the procedure of Wolfe and Stillman [4]. The Hall mobility increases monotonically with decreasing cracker temperature, which indicates a reduction in the total ionized impurity concentration, $N_D + N_A$, the dominant scattering centers at 77 K for mobilities less than 1.5×10^5 cm^2/V s. From 1000 to 900°C, the reduction is primarily in N_A, whereas N_D remains nearly constant. From 900 to 800°C, both impurity types decrease, with N_A dropping by a factor of 4.5 compared with a 2.7 times decrease in N_D. Run 66, performed at a cracker temperature of 750°C, was slightly n-type at 300 K and highly resistive at 77 K (> 500 kΩ for the van der Pauw samples), indicating closely compensated GaAs.

TABLE 4-1

Summary of Growth Data and Hall Measurement Results for GaAs Films

Run	Cracker Temperature (°C)	Arsine Flow Rate (sccm)	n_{77K} (cm^{-3})	μ_{77K} (cm^2/V s)	N_D (cm^{-3})	N_A (cm^{-3})
62	1000	2.8	3.6×10^{14}	9.4×10^4	6.2×10^{14}	2.6×10^{14}
63	900	2.8	4.6×10^{14}	9.8×10^4	6.5×10^{14}	1.9×10^{14}
64	800	2.8	2.0×10^{14}	1.5×10^5	2.4×10^{14}	4.2×10^{13}
66	750	3.0	Highly resistive	—	—	—
38*	—	—	2.6×10^{14}	9.6×10^4	5.4×10^{14}	2.8×10^{14}
* Elemental arsenic.						

Photoluminescence scans of the layers grown with arsine are shown in Figures 4-1 and 4-2. The curves in the region of acceptor recombination (~ 1.495 eV) have been magnified to facilitate examination. Peak assignments have been made in accordance with other high-purity GaAs work [5]. In Figure 4-1 the ratio of the band-edge intensity near 1.518 eV to the conduction-band-to-acceptor transition $C(e-A^0)$ near 1.495 eV is relatively high, consistent with the low N_A as determined from the Hall measurements. The neutral (D^0,X) and ionized (D^+,X) donor-bound excitons are well resolved, indicative of high-quality material, although the linewidths are not particularly narrow at this pump power. Similarly, the acceptor-bound exciton (A^0,X) is observed, but the light- and heavy-hole splitting has not been resolved. Noteworthy for the arsine growth is the absence of a defect-bound exciton band, which is normally observed in MBE growth using elemental arsenic [5].

In Figure 4-2, the $C(e-A^0)$ intensity first increases as the injector temperature is reduced from 1000 to 900°C and then decreases with a further reduction to 800°C. This intensity increase results from the contribution of the adjacent peak attributed to a donor-acceptor pair transition $C(D^0-A^0)$. This transition first increases from 1000 to 900°C, which is consistent with the lower compensation observed in the Hall measurements. At 800°C, it has decreased below the 1000°C spectrum. Additional lower-intensity peaks are observed at lower energies, which have been attributed to donor/deep-acceptor pair transitions [5]. The particularly striking feature of the scans of the 750°C layer is the reduction of all the neutral-donor-related transitions. The donor-acceptor pair transition $C(D^0-A^0)$ is greatly reduced in intensity and the neutral-donor-bound exciton (D^0,X) transition has been eliminated. This is consistent with the high resistivity of the material. The transition labeled FE observed at 750°C at the band edge is probably due to the free exciton.
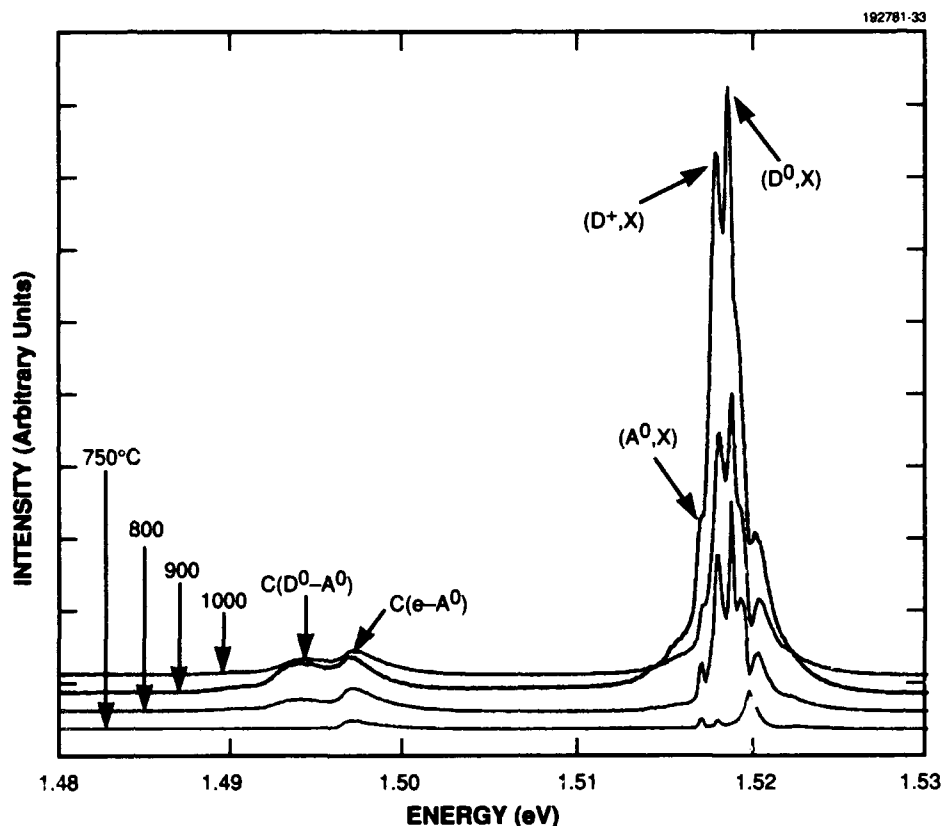
Figure 4-1. 4-K photoluminescence spectra of layers from runs 62 (1000°C), 63 (900°C), 64 (800°C), and 66 (750°C). The excitation wavelength is 514 nm, and the excitation power is ~ 6 W/cm². The resolution is 0.14 meV. The traces have been offset for clarity.

The main sources of unintentional impurities in gas-source MBE are outgassing of the vacuum system components and impurities in the source materials. The predominant unintentional impurity in solid-arsenic source MBE is carbon from volatile hydrocarbons in the MBE ambient, which yields p-type material in the 1×10^{14} cm^{-3} range. In very clean MBE systems with low hydrocarbon concentrations, lightly doped n-type $(N_D + N_A \approx 6 \times 10^{13}$ cm^{-3}, $\mu_{77K} = 1.7 \times 10^5$ cm²/V s) material is obtained, which contains residual sulfur impurities emanating from the arsenic source material [6]. According to the gas manufacturer, the dominant impurities in the arsine are silane and germane. Incorporation of these impurities in gas-source MBE of GaAs will dope the material n-type whereas hydrocarbons will dope the GaAs p-type; silicon and germanium are also present in elemental arsenic source material, but are insignificant impurities using elemental arsenic as they have a very low vapor pressure at typical arsenic source temperatures (200 to 300°C). Run 62 yields high N_D (6.2 $\times 10^{14}$ cm^{-3}), which indicates an n-type impurity present in the arsine that is pyrolyzed at the high cracker temperature (1000°C). The N_A in run

45

62 is approximately the same as in run 38, which implies that at 1000°C the residual carbon concentration is unaffected by the use of arsine. As the cracker temperature is reduced, the residual acceptors in the films are reduced over sixfold in comparison with runs 38 and 62. An examination of the arsine cracking pattern using in situ residual gas analysis shows that over the temperature range from 1000 to 700°C, arsine predominates at the lower temperatures but that the concentrations of arsenic and As_2 increase above that of arsine at 1000°C.

Quantitative analysis is complicated by the presence of residual arsine condensed on cryopanels. At the lower temperatures, partially cracked arsine (AsH, AsH_2) and arsine are present in the incident group V beam. The greatly lowered N_A with lower cracker temperatures suggests that a reaction is occurring between the arsine or arsine fragments and the hydrocarbons, which is suppressing carbon incorporation into the growing film. The decrease in the n-type impurity with decreasing cracker temperature is consistent with a reduction in the cracking efficiency of silane or germane. For run 66, with the cracker at 750°C, the arsine flow rate was increased to maintain a stoichiometric surface. Although the epilayer was too resistive to make Hall measurements, the photoluminescence spectrum indicated that the donor density was less than for layers grown with higher cracker temperatures.
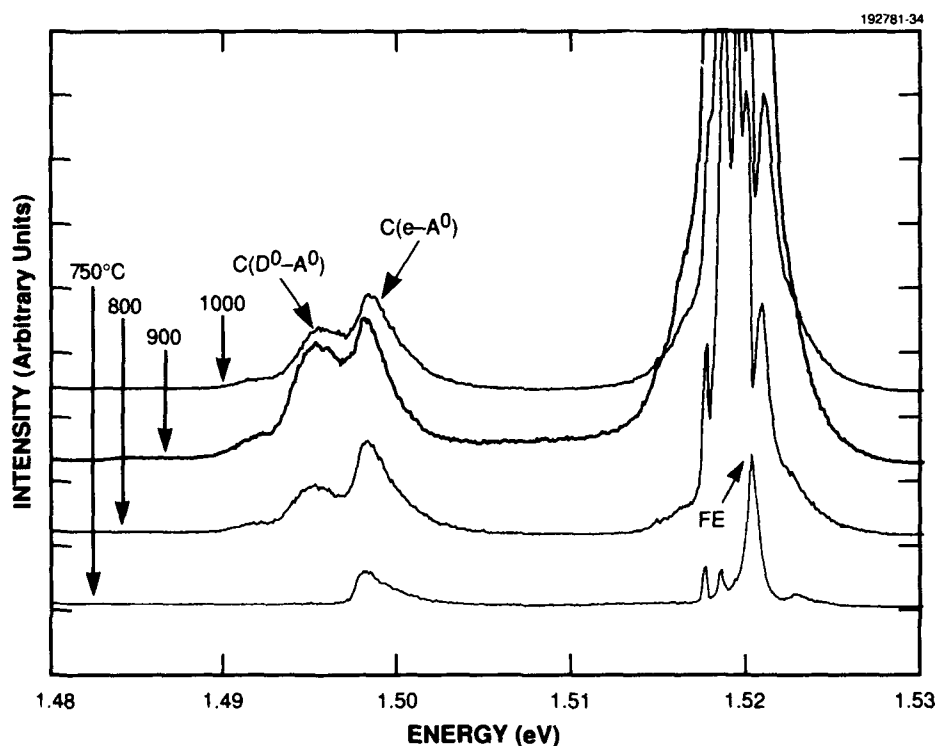
Figure 4-2. Same photoluminescence spectra as in Figure 4-1, but with the intensity scaled 4×.

46

The question remains as to what form of arsine molecule the surface is able to decompose as a source of arsenic for the GaAs crystal. For the higher cracker temperatures, a flow rate of 2.8 sccm was used because this was the lowest stable flow setting of the mass flow controllers. At this flow rate the reflection electron diffraction (RED) patterns during growth indicated an excessive arsenic flux for growing higher-quality GaAs. The optimum As:Ga flux ratio has been found to be slightly greater than one. A higher growth rate, which is determined by the group III arrival rate, would have likely resulted in higher-purity material. This was not attempted because of potential side effects that might have affected other device work on the gas-source MBE system. As the cracker temperature was lowered, the quantity of arsenic available to the surface was reduced, until at 750°C the arsine flow rate needed to be increased to 3.0 sccm to maintain the slightly As-rich surface, according to the RED pattern. It is unclear whether GaAs can be formed from elemental gallium and partially cracked arsine at the low substrate temperatures (580 to 640°C) used for GaAs growth by MBE. The RED pattern observed using a cracker temperature of 750°C was significantly different from that observed when solid arsenic was used. When the arsine flux was turned off, the pattern indicated a Ga-rich surface at a substrate temperature that would normally have resulted in a Ga-stable pattern. The precursor to GaAs growth with a solid arsenic source is considered to be two As atoms bonded to a Ga atom. The RED pattern observed when arsine is used suggests that the precursor to GaAs growth involves dissociation products such as AsH. We would expect the Ga-AsH precursor to be less stable than the As-Ga-As precursor, which would result in a Ga-rich surface when the arsine is turned off.

Our initial observations of the growth of GaAs with arsine indicate low arsine usage (a factor of 30 to 60 times lower than for organometallic chemical vapor deposition), ease of group V flux control compared to solid arsenic, and the capability of growing high-purity GaAs by using a lower cracker temperature. An advantage of arsine over solid arsenic is that background hydrocarbon incorporation is reduced. The residual impurity concentration is n-type and appears limited by the purity of the arsine.

P. A. Maki
S. C. Palmateer
A. R. Calawa

4.2 ADVANCES IN LASER-DIRECT-WRITE REPAIR OF DIGITAL INTEGRATED CIRCUITS

Laser-direct-write techniques have been used for repairing the interconnect metallization of digital integrated circuits (IC) [7]. In this report, we describe two improvements to the repair procedure, involving the addition of an excimer laser to the apparatus and the development of a platinum deposition technique. These refinements have enhanced the reliability and yield of the repair process.

Our improved system employs two lasers: a pulsed excimer laser, which is used for opening via holes and for cutting conductors, and an argon-ion laser operating CW at 488 nm, which is used for metal deposition. The two laser beams are focused by two separate microscope objectives onto the plane of the IC. The sample to be repaired can be positioned under either optical path. Thus, in a typical repair

procedure the cuts and via holes are completed first using the excimer laser. Then, without exposing the sample to air, the IC is translated under the argon-ion laser and the metal lines are added. By avoiding exposure to air and water vapor and depositing the new metal lines promptly, the contact resistance of the via holes is minimized. The translation stage and lasers are computer controlled, and a video camera and monitor allow real-time viewing of the repair.

The choice of lasers was dictated by the spatial and thermal requirements of the cutting and deposition processes. For instance, on highly thermally conducting layers such as aluminum, the diffusion of heat delivered to the target during the laser pulse, instead of the focal size, may determine the resolution. In fact, laser pulse durations of ~ 1 ns would be desirable to obtain highly controllable ablation of submicrometer regions. The pulsed excimer laser in our system is a microwave-pumped waveguide laser operating at 248 nm. It has a variable pulse repetition rate up to 2 kHz and an average output power up to 50 mW. Diode-pumped Q-switched Nd:YLF lasers operating at 523 nm and excimer lasers typically produce pulses with durations in the range of 20 to 50 ns, and a spatial resolution of 1 to 2 μm can be obtained for ablation of aluminum using either laser. On some materials, however, such as polyimide, the much greater absorption at the 248- or 193-nm excimer laser wavelength compared to the visible can improve the selectivity of ablation.

Many polymers, including polyimide, strongly absorb deep ultraviolet radiation and undergo a combination of thermal and photochemical decomposition. This process can lead to very clean ablation, without charring of the polymer. We have found that when metal conductors buried in polyimide or sitting on polyimide layers are cut with either a beam from a CW 488-nm argon-ion laser or with a pulse from a Q-switched 523-nm laser, a conductive track with a sheet resistance of a few kilohms per square is produced between the severed sections of the conductor. Cutting with pulses from a 248-nm excimer laser, on the other hand, does not produce this conductive track. Excimer ablation can remove polyimide cleanly and selectively, as shown in the scanning electron micrograph in Figure 4-3. The excimer laser has been rastered over a region of a copper-polyimide multichip module, and the polyimide, except where masked by the copper conductors sitting on and buried in it, has been cleanly removed. At the laser fluences used the metal remained intact; at higher fluences the metal lines would be cut as well. This localized selective process of removing polyimide allows buried conductors in a multichip module to be exposed for laser cutting or for probing.

Several different conductors have been explored for circuit repair applications. Polysilicon has been used, but in some circuits the high deposition temperature has led to shorts forming through the field oxide to the underlying substrate. Tungsten and cobalt have also been laser deposited, but both have limitations. Tungsten lines are deposited under high stress and have poor adhesion to SiO_2 layers, and as a result they are likely to lift from the substrate and curl. Furthermore, the WF_6:SiH_4 mixture used for deposition can be explosive if mixed in incorrect proportions. The high reactivity of WF_6 with water vapor results in a requirement to flow fresh WF_6 through the cell unless the reaction cell is well passivated. Likewise, cobalt deposition is hampered by the high reactivity of the precursor $Co_2(CO)_8$ with air and water vapor and by its tendency to decompose spontaneously at room temperature. On the other hand, cobalt deposition is a photolytic process at 488 nm, and it therefore has the advantage of taking place at temperatures as low as 20°C, even on transparent substrates.

192781-49

→| |←— 10 μm
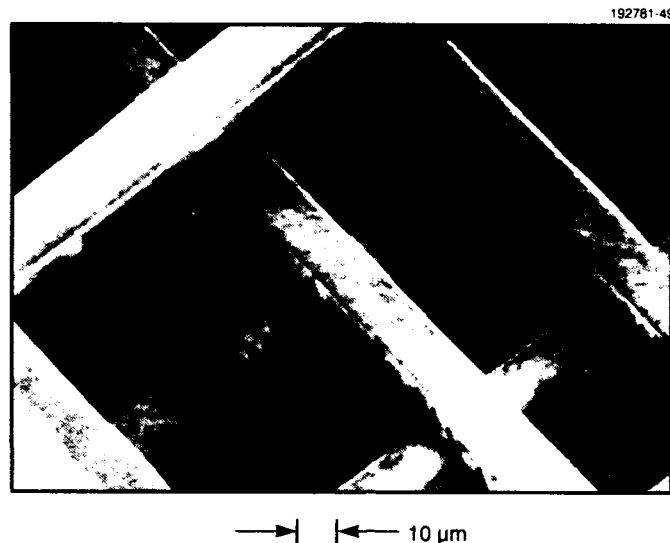
Figure 4-3. Scanning electron micrograph of a copper-polyimide multichip module. An excimer laser has been used to ablate the polyimide, revealing the buried copper conductors.

We have recently developed a laser deposition process for platinum, which overall is more reliable and more convenient than either the tungsten or the cobalt process. The platinum deposition is carried out at a low enough temperature to allow its use on polyimide layers, the resistivity of the deposited material is consistently near the bulk value of platinum, good quality contacts can be formed to aluminum, and the precursor vapor is stable in the cell for long periods. The precursor is $Pt(PF_3)_4$, which at room temperature is a transparent liquid with ~ 35-Torr vapor pressure. Laser writing is typically performed with ~ 5 Torr of pure vapor in a static cell. The laser is operated at 488 nm, and a 50×, 0.45-numerical-aperture, long-working-distance objective is used to focus the beam to a spot ~ 1 μm in diameter. The laser power at the focus is usually ~ 50 mW. Writing rates of platinum are in the range of ~ 250 μm/s and can be as high as 5 mm/s on substrates such as polyimide. The resistivity of the deposited material is 10 to 11 μΩ cm. Although platinum lines as narrow as 2 μm have been deposited, a more typical connection is 5 μm wide and ~ 1 μm thick.

The conditions listed above maintain a good process window above minimum deposition threshold, with good step coverage and without damage to the oxide and underlying layers. The 5-μm width may at first appear to limit the resolution of the repair process, but actually the micrometer-sized via formation procedure sets the resolution limit. The passivation on the chip allows the laser-deposited lines to cross over and overlap existing conductors. Contact is made only where the vias are placed using the excimer laser. Successful repairs have been made to existing aluminum lines as small as 3 μm. A scanning electron micrograph illustrating the connection of a laser-written platinum line to existing aluminum lines on an IC is shown in Figure 4-4. The arrow indicates the location of a laser-drilled via, and the platinum line is seen extending to the right from the via. An existing aluminum line that has been laser cut is seen near the bottom of the micrograph.

49
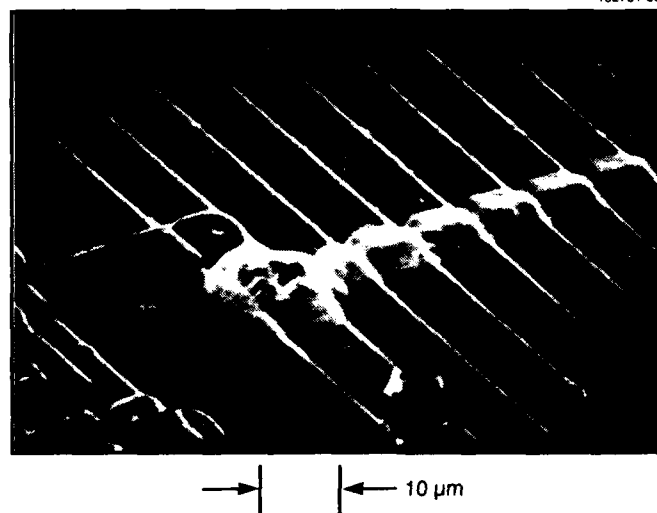
Figure 4-4. *Scanning electron micrograph showing the connection (arrow) between a laser-written platinum line and the existing aluminum lines on an IC.*

By employing the above procedure, modifications can be made to fully fabricated and packaged ICs. The most common modification is correction of a design error involving inadvertent miswiring of a connection. By cutting away the incorrect wire and depositing a new conductor with vias, the modified part of the IC can then be tested. On occasion, this further testing has revealed additional errors that can be repaired. The cycle is repeated until the chip is fully functional, with each iteration saving the cost and time of fabricating a new IC. The procedure also allows a designer to obtain diagnostic information from previously inaccessible internal points by adding probe points or by isolating sections of circuitry. We have repaired and/or analyzed over two dozen designs using the laser cutting and deposition techniques, thereby significantly simplifying and shortening the design process. Although the resolution achieved with our methods is somewhat greater than a micrometer, this limitation does not appear to be a constraint for most areas requiring repair.

D. C. Shaver   M. Rothschild
S. P. Doran   J. H. C. Sedlacek

REFERENCES

1.   A. R. Calawa, *Appl. Phys. Lett.* **38**, 701 (1981).

2.   M. J. McCollum, Ph.D. thesis, University of Illinois, 1990.

3.   J. E. Cunningham, T. H. Chiu, G. Timp, E. Agyekum, and W. T. Tsang, *Appl. Phys. Lett.* **53**, 1285 (1988).

4. C. M. Wolfe and G. E. Stillman, *Appl. Phys. Lett.* **27**, 564 (1975).

5. B. J. Skromme, S. S. Bose, B. Lee, T. S. Low, T. R. Lepkowski, R. Y. DeJule, G. E. Stillman, and J. C. M. Hwang, *J. Appl. Phys.* **58**, 12 (1985).

6. E. C. Larkins, E. S. Hellman, D. G. Schlom, J. S. Harris, M. H. Kim, and G. E. Stillman, *Appl. Phys. Lett.* **49**, 391 (1986).

7. Solid State Research Report, Lincoln Laboratory, MIT, 1989:1, p. 47.

5. HIGH SPEED ELECTRONICS

5.1 GaAs/AlGaAs QUANTUM WELLS GROWN OVER EPITAXIAL CoAl LAYERS BY MOLECULAR BEAM EPITAXY

Structural and photoluminescence properties have been investigated for GaAs/AlGaAs multiple quantum wells (MQWs) grown by molecular beam epitaxy (MBE) over AlAs/CoAl/AlAs (for simplicity, we use CoAl to refer to Co_xAl_{1-x} with $x \approx 0.5$). CoAl was chosen as the buried metal layer because it is thermally stable on AlAs with < 1.2% lattice mismatch to GaAs [1] and because techniques for growing epitaxial CoAl are well documented [2]. The quantum wells can be used to understand both the growth history of the overlayers and their optical quality. Growing each layer of the MQW structure for a specific time allows an examination of the evolution of the growth surface. This evolution can be observed and studied quantitatively on cross-sectional transmission electron micrographs (TEMs). Photoluminescence data from the MQW structures yield information on well uniformity and doping, well and barrier traps, and aggregate doping levels. This preliminary work indicates the feasibility of growing epitaxial quantum wells over a CoAl layer and may lead to a variety of unique electrooptical devices incorporating buried optical mirrors, Schottky barriers, and/or ohmic electrical contacts.

Figure 5-1 shows a schematic diagram and Figure 5-2 presents cross-sectional TEMs of a sample consisting of 2-nm-thick AlAs, 10-nm-thick CoAl, and 2-nm-thick AlAs base layers along with a sequence of MQW buffer layers and a 20-well MQW structure. AlGaAs was used between all MQW layers and as the top cladding layers. All layers of all samples were grown with no intentional doping. The
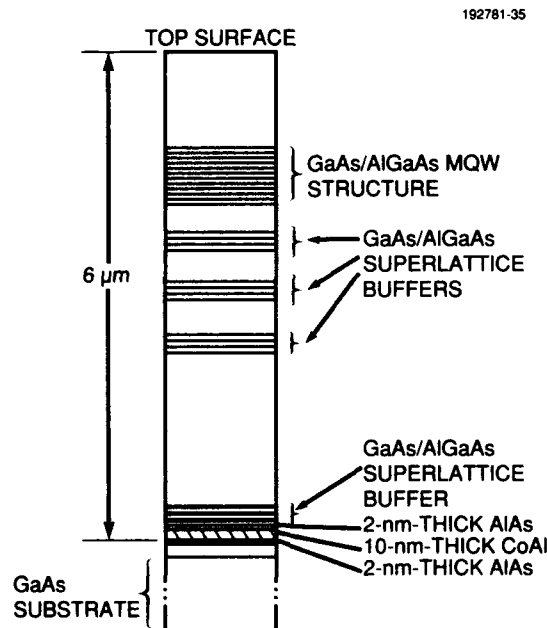
Figure 5-1. Schematic diagram of a sample consisting of 2-nm-thick AlAs, 10-nm-thick CoAl, and 2-nm-thick AlAs base layers along with a sequence of MQW buffer layers and a 20-well MQW structure.

53

(a)

(b)
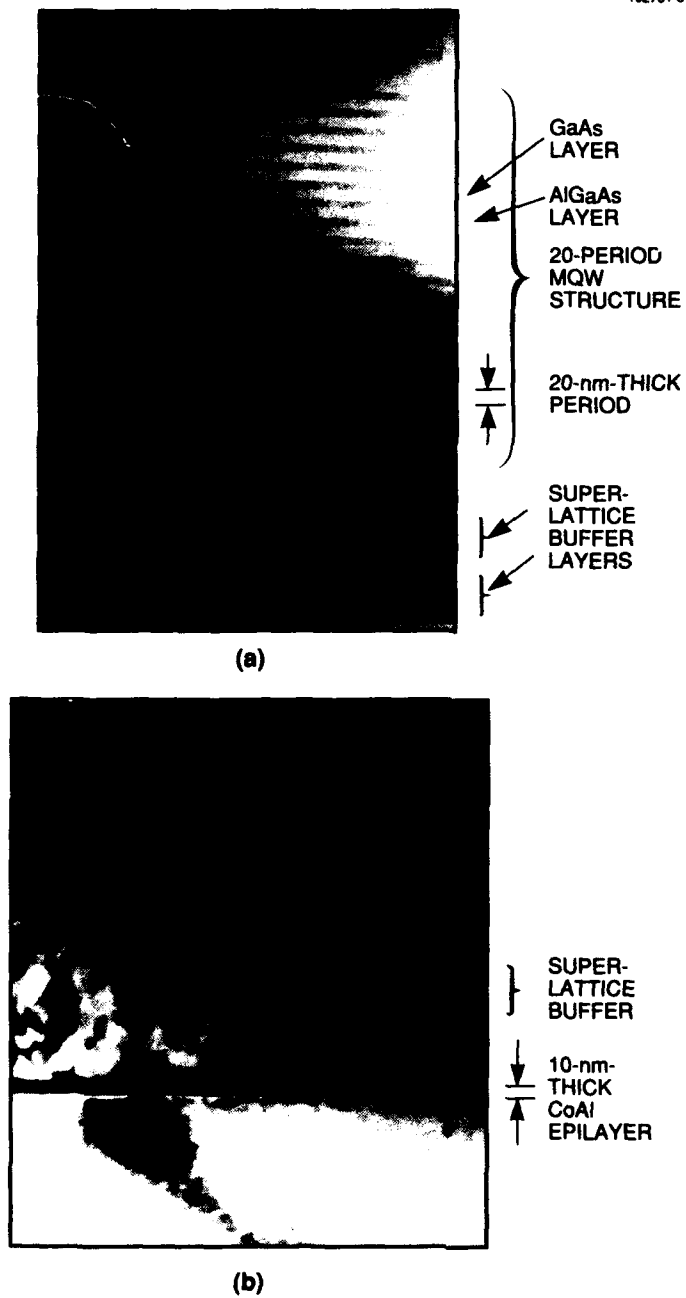
Figure 5-2. Cross-sectional TEMs of the sample in Figure 5-1 showing (a) the MQW structure and (b) the AlAs/ CoAl/AlAs base layers.

54

TEMs of the MQW structure and base layers in Figures 5-2(a) and 5-2(b), respectively, clearly show the evolution of the morphology of the growing surface. A number of stacking faults and other defects are evident, which are generated at the interface between the CoAl and top AlAs base layers. As the total overlayer thickness increases, some faults merge, creating some faceting that propagates to the surface.

The photoluminescence data at 77 K from the sample in Figure 5-1 are presented in Figure 5-3, showing a peak due to the MQW structure (heavy-hole exciton) with a half-intensity linewidth of ~ 15 meV and less resolved peaks due to excitons in the top AlGaAs cladding layer and to excitons bound to acceptors associated with this layer. Photoluminescence intensities were moderate, being 50 times lower than those of high-quality MQW structures grown on GaAs in our laboratory. The MQW photoluminescence peak implies a well thickness of 7.5 nm, and measurements from the cross-sectional TEM in Figure 5-2(a) yield well and barrier thicknesses of ~ 7 and 13 nm, respectively. The fact that the MQW peak is well defined with a half-intensity linewidth of ~ 15 meV is not surprising since, as shown in Figure 5-2(a), the quantum wells have very uniform thicknesses while conforming to the irregularly shaped growing surface. The 15-meV half-intensity linewidth of the MQW peak can be accounted for by one to two monolayers of variation in the well thicknesses (the well thickness is only 7.5 nm). Furthermore, the narrow linewidth indicates that the quantum wells have very low background doping levels. From the AlGaAs peak, the AlAs mole fraction is calculated to be ~ 0.26. The acceptor in the sample is probably
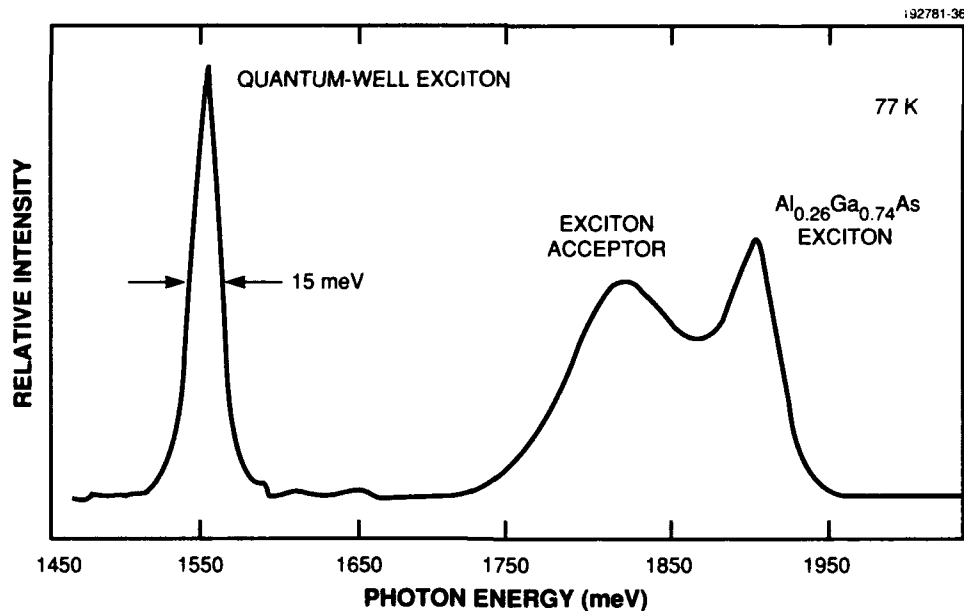
Figure 5-3. Photoluminescence spectra at 77 K for the sample in Figure 5-1.

carbon that is incorporated while growing AlGaAs at low substrate temperatures. A 550°C substrate temperature was used in this work, which is much lower than the 685°C temperature normally employed in our systems to grow high-quality AlGaAs.

W. D. Goodhue   G. D. Johnson
H. Q. Le   J. W. Bales

REFERENCES

1. T. Sands, C. J. Palmstrom, J. P. Harbison, V. G. Keramidas, N. Tabatabaie, T. L. Cheeks, R. Ramesh, and Y. Silberberg, *Mater. Sci. Rep.* **5**, 99 (1990).

2. J. B. Harbison, T. Sands, N. Tabatabaie, W. K. Chan, L. T. Florez, and V. G. Keramidas, *Appl. Phys. Lett.* **53**, 1717 (1988).

6. MICROELECTRONICS

6.1   CCD IMAGE FEATURE EXTRACTOR

An image processor based on a charge-coupled device (CCD) has been designed and fabricated for two-dimensional finite impulse response filtering or extraction of features from a gray-level image. The processor, called an image feature extractor (IFE), consists of an analog input buffer, 49 multipliers, and 49 8-bit 20-stage local memories in a 29-mm-square chip area. Better than 99.999% charge-transfer efficiency (CTE) and > 42-dB dynamic range have been achieved by the IFE, which performs one billion arithmetic operations per second while dissipating < 1 W when clocked at 10 MHz. The device is suitable for neural networks with local connections and replicated weights such as the neocognitron [1]. Implementation of the neocognitron network using IFEs has been simulated, and the effects of weight quantization imposed by the 8-bit words of the IFE memory are presented.

The IFE scans up to 20 7 × 7 feature templates or filter kernels over a 128-column-wide image in raster fashion. The image pixels are serially read into the device line by line, and the task of reformatting the input and selecting the appropriate pixels for windowing is performed on chip. At each window position the inner products of the kernels and the windowed pixels are computed. As can be seen in Figure 6-1, the IFE consists of two major functional blocks: processing elements and a 775-stage input buffer that shifts and holds input pixels. Taps placed at appropriate points along the input buffer select the windowed pixels. The processing elements consist of 49 CCD 8-bit four-quadrant multiplying digital-to-analog converters (MDACs) [2] with digital words represented in two's-complement notation. The digital words are stored in cyclic CCD shift registers, as described in [3]. The volatility of the CCDs is circumvented by use of a feedback-enable switch at each bit of memory, which allows refreshing by reading and rewriting words as needed. Clocked at 10 MHz, the IFE can produce 20 filtered versions of a 128 × 128-pixel image in 32 ms.

The IFE was fabricated using a double-polysilicon, double-metal buried-channel CCD/CMOS process. The design rules were 3 μm for the second-polysilicon and second-metal layers, 2.5 μm for the first-metal layer, and 2 μm for all other layers. The CTE of the input buffer was tested at 10-MHz clock rate, and the results are shown in Figure 6-2. No transfer loss was observed after 3100 transfers, indicating greater than 99.999% CTE. The uniformity of the MDACs was also tested. Figure 6-3 depicts the output of the IFE with a uniform gray input and kernels programmed as follows: in the first 7 × 7 kernel 40 weights were set to the maximum representable value with the other 9 weights set to zero; in the next template 38 weights were set to the maximum value with the other 11 weights set to zero; and so forth to the 20th template in which only 2 weights were set to maximum. The expected output is a linear ramp, which is indeed observed in Figure 6-3.

The IFE is suited for implementation of neural networks with local connectivity patterns and groups of neurons with identical weights. The neocognitron, a feature-extraction network based on a model of the early visual system, is such a network. A neocognitron was implemented in software and trained to recognize hand-printed characters represented by 20 × 20-pixel binary images. The simulation was then modified so that the computations and weight representations were limited to 8 bits, as would be the case

57
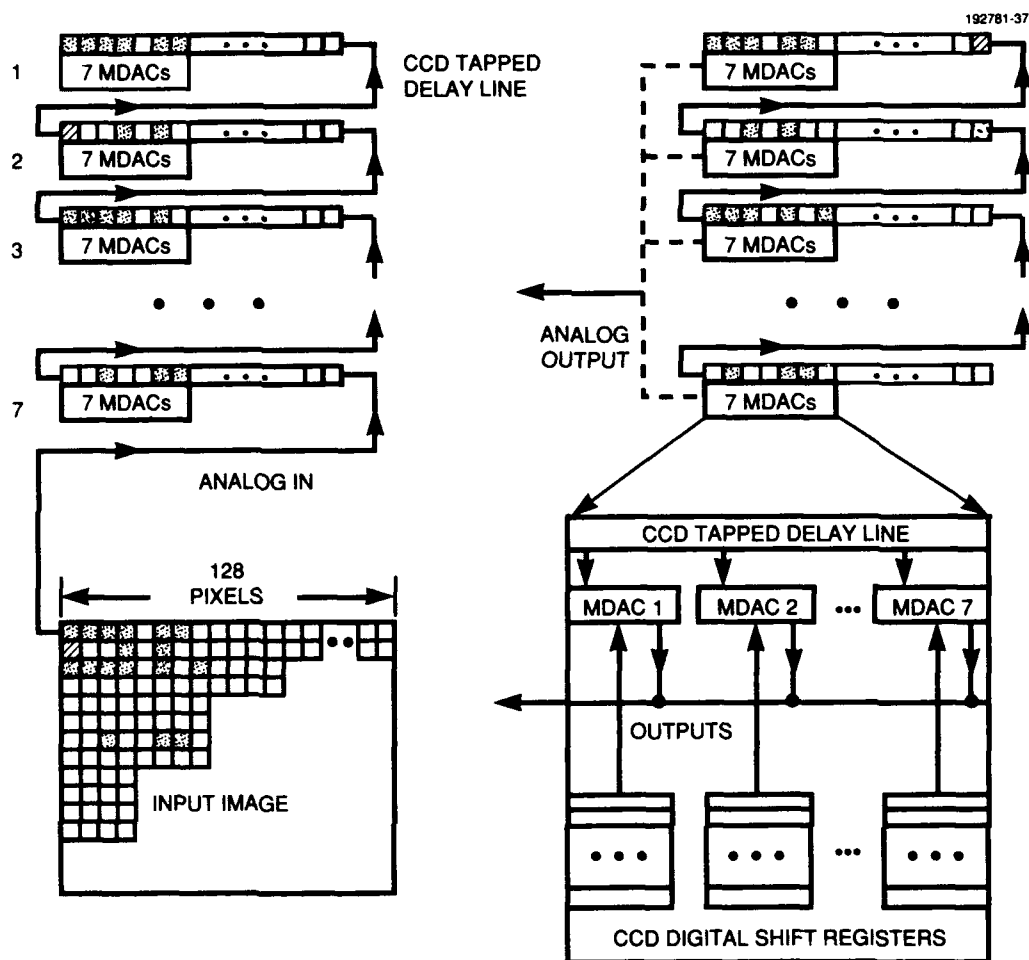
Figure 6-1. Layout arrangement and data flow of the CCD image feature extractor. The pattern in the CCD delay line at the upper right occurs one clock period after that shown at the upper left.

if the network were implemented using IFEs. Relative to a network using floating-point arithmetic and weights, the ability to correctly identify characters decreased to 89.4%. A modified training procedure was then developed to reduce the effects of quantization that would result from the use of IFEs. The networks trained by the new procedure had a 96.0% correct identification rate.

A. M. Chiang
J. R. LaFranchise
M. L. Chuang

192781-52
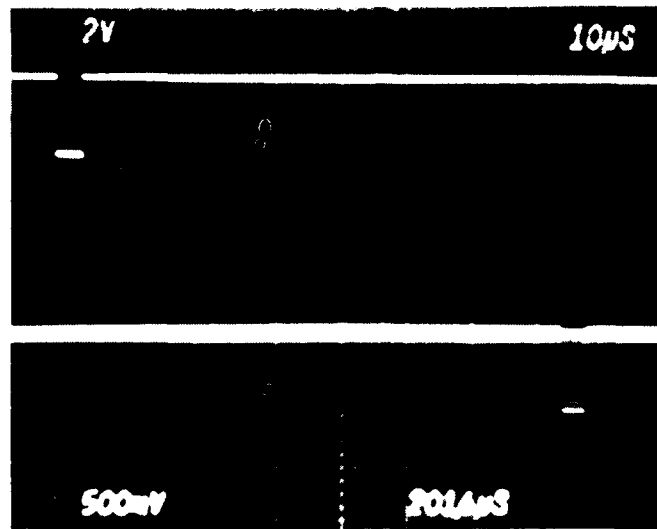
Figure 6-2. Input (top trace) and output (bottom trace) signals of the CCD tapped delay line demonstrating better than 99.999% CTE at 10-MHz clock rate.

192781-53
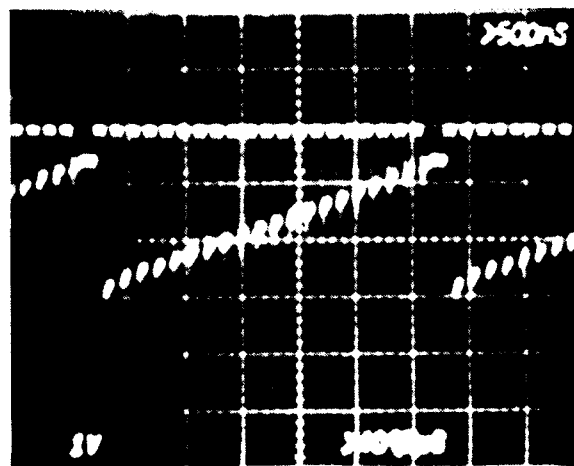
Figure 6-3. Test result demonstrating uniformity of CCD MDACs.

6.2 CHARACTERIZATION OF AN ELECTRONIC SHUTTER FOR BACK-ILLUMINATED CCDs

An integrated electronic shutter for back-illuminated CCDs, which was described in an earlier report [4], has been characterized during operation. Measured results show that the shuttered devices have extinction ratios $> 10^4$ for wavelengths < 540 nm and have switching times < 55 ns. Also characteristic of the shuttered devices is an optical pixel response that is linear for signal levels as high as two-thirds of the CCD pixel full well.

Measurements demonstrating the capability of the integrated electronic shutter were done on a 64 × 64 back-illuminated frame-transfer CCD with a 27 × 27-μm pixel size and a substrate thickness ~ 17 μm. Figure 6-4 shows the measured extinction ratio for wavelengths between 450 and 800 nm. Up to 540-nm wavelength the value was $> 7.5 \times 10^4$, higher than could be measured with the experimental setup; beyond 540 nm it declined sharply. This decrease is caused by the exponential decay of photon absorption with depth. Calculated values, based upon a 2-μm perpendicular distance between the silicon dioxide surface and the p-type buried layer and a 15-μm distance between the p-type buried layer and the back-illuminated entry surface, are shown for reference in Figure 6-4. While the extinction ratio at longer wavelengths is low, the value can be increased by increasing the thickness of the silicon membrane; for instance, increasing the silicon membrane thickness to 25 μm wo᾽ ι increase the value from 300 to ~ 2500 at 630 nm. The extinction ratio for a fixed wavelength remained constant up to photoelectron flux densities as high as 8×10^8 cm^{-2} s^{-1}.
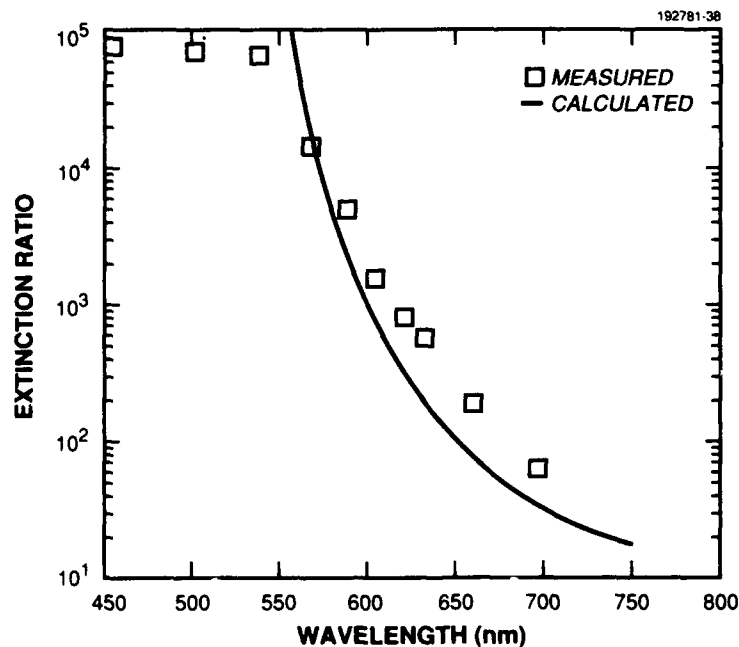
Figure 6-4. Comparison of measured and calculated extinction ratios vs wavelength for the integrated electronic shutter.

Shutter rise and fall times were measured by stepping in time a pulse of light through the shutter transition regions (closed to opened and opened to closed) and recording the CCD output response vs the time step. A shutter function $S(t)$ is defined as $[D(t)-D_c]/[G(t)-D_c]$, where $D(t)$ is the number of photoelectrons detected out of the total number $G(t)$ generated by a unit light impulse at time t, and D_c is the number of photoelectrons detected from a similar pulse of light with the shutter fully closed. The CCD output is the convolution of $S(t)$ with the rate of photoelectrons generated by the experimental light pulse. Figure 6-5 gives the measured CCD output signal for shutter rise and fall regions and shows that the switching times are < 55 ns taken between the 10 and 90% values. Since the light pulse used in the experiment is between 6 and 8 ns, the CCD output signal gives a reasonable measure of the shutter switching times. The rise and fall times of the external drive circuitry are ~ 35 ns, while the time required for photoelectrons to reach either the storage or shutter drain region after being generated by the light pulse is estimated to be a few nanoseconds. Thus, most of the electronic switching time is attributed to the external drive circuitry.
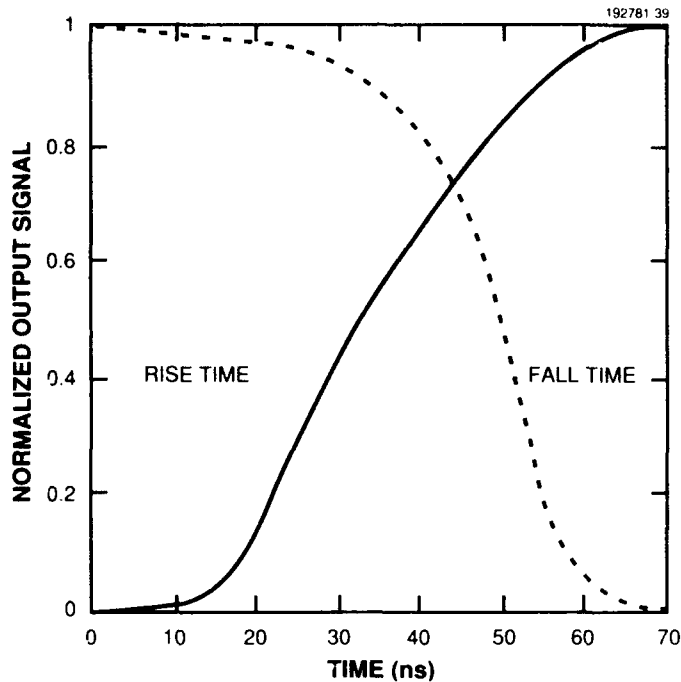
Figure 6-5. Shutter rise and fall times of a typical pixel.
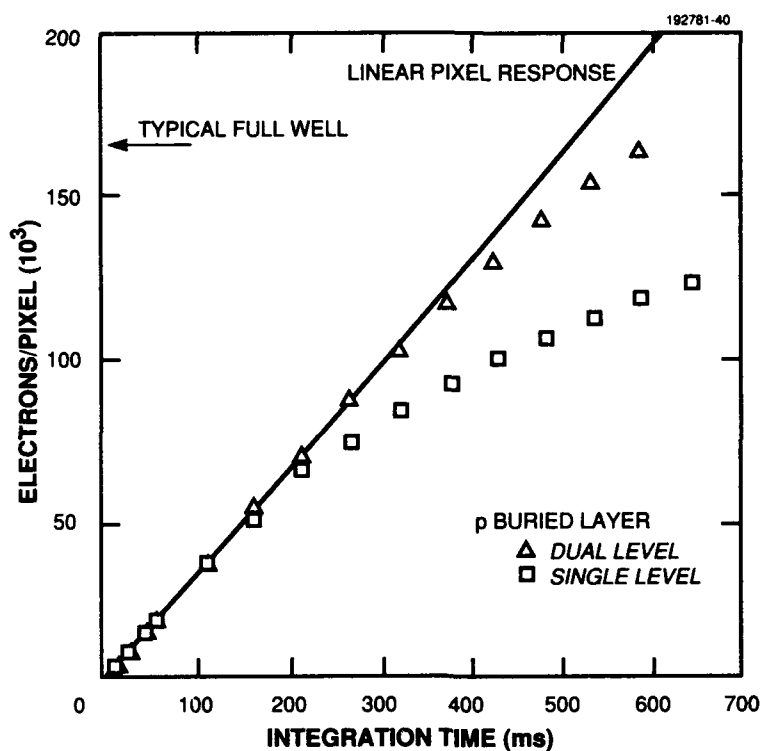
Figure 6-6. Pixel response of the single and dual p-type buried layer as a function of the integration time. The linear pixel response is given for reference.

As discussed in the earlier report [4], the stepped or dual p-type buried layer provides a depletion region that is independent of the signal accumulated in the well up to some maximum amount. Figure 6-6 shows the pixel response vs integration time for both a single and dual p-type buried layer. The shutter drain was biased so the depletion region went through and slightly beyond the p-type buried layer. As long as the depletion region associated with the detection area is constant, the pixel response would have a linear dependence on integration time with the photoelectrons dividing in some constant proportion between the shutter drain and the n-type buried-channel detection area. The results in Figure 6-6 show that the pixel response for the dual p-type buried layer remains linear up to about two-thirds of the pixel full well, while the single p-type buried layer becomes sublinear at relatively low signal levels.

R. K. Reich   J. C. Twichell
R. W. Mountain   B. B. Kosicki
W. H. McGonagle,   E. D. Savoye
C. M. Huang

6.3   IMPROVEMENTS IN CCD HARDNESS UNDER PROTON IRRADIATION

An urgent problem with the long-term use of CCD imagers is the increase of charge-transfer inefficiency (CTI) and dark current that results from high-energy proton bombardment. These effects are most pronounced on low-noise devices that must function at low signal levels. In a previous report [5] we described a technique for minimizing trapping effects at low charge levels by adding a narrow (2 to 3 μm) potential trough down the center of the channel. In this report we describe measurements of CTI vs temperature on a device with troughs, both before and after proton irradiation. The results show that an optimum temperature range exists where the CTI degradation is minimized.

The CTI was measured on a 420 × 420-pixel frame-transfer imager [6] that had troughs of 2 μm in the imaging and frame-store arrays and 3 μm in the serial register [5]. The device was made on magnetic Czochralski (MCZ) material with a resistivity of 1000 Ω cm. This material was selected because it has produced devices with excellent CTI over the temperature range from 100 to 230 K [7]. To perform the CTI measurements, we used a technique described previously [7] in which the device is irradiated with soft x-rays from the radioisotope Fe^{55} to generate charge packets of ~ 1620 e^-. The device was operated in the full-frame mode in which both imaging and frame-store regions collected x-ray events for a few seconds and then both arrays were read out. The serial register transfer rate was 500 kHz, while the parallel-to-serial transfer of each row used a 5-μs clock burst. Proton irradiation was performed at the Harvard Cyclotron Laboratory, and for the device described here the dose was 1.1×10^{11} cm^{-2} at 40 MeV, or 20 krad (Si).

Figure 6-7 shows the CTI data as a function of temperature before and after irradiation. The parallel CTI data refer to the frame store; the data for the imaging array were similar to but about 30% higher than for the frame store. One source of the difference is that the length of each pixel in the direction of charge transfer is greater in the imaging array (27 μm) than in the frame store (18 μm). Thus, a charge packet should encounter 50% more traps in traversing the imaging array than the frame store. The preirradiation parallel CTI was < 10^{-5} per pixel transfer over the entire temperature range, while the serial CTI rose above this level only below 140 K. As discussed previously [7], this increase is due to an unknown shallow trap.

As shown by Figure 6-7, the CTI rises substantially after irradiation because of defects introduced by displacement damage. As the temperature drops from 200 to 150 K, the parallel CTI shows a sevenfold improvement. In this regime the primary trapping center affecting charge loss is the phosphorus-vacancy (PV) center [8], and the emission time of this center is increasing from ~ 10^{-2} to 10^3 s. At the upper temperature this center empties completely between data frames, and each charge packet experiences maximum trapping loss in the parallel arrays. At 150 K the traps stay filled for much longer than the frame time, and the charge loss is accordingly reduced. The serial CTI, by contrast, is relatively unaffected by the temperature decrease, in part because all the charge from the parallel arrays is being transferred through the serial register. This ensures that the serial traps are exposed to charge packets at a rate higher than the PV emission rate, and therefore these centers remain mostly filled throughout the temperature range of the measurement. The PV center alone, however, cannot explain all the features of the data. Additional trapping centers with much faster emission times must be present to account for the facts that at the lower end of the temperature range the parallel CTI levels off and the serial CTI is much poorer than the parallel.
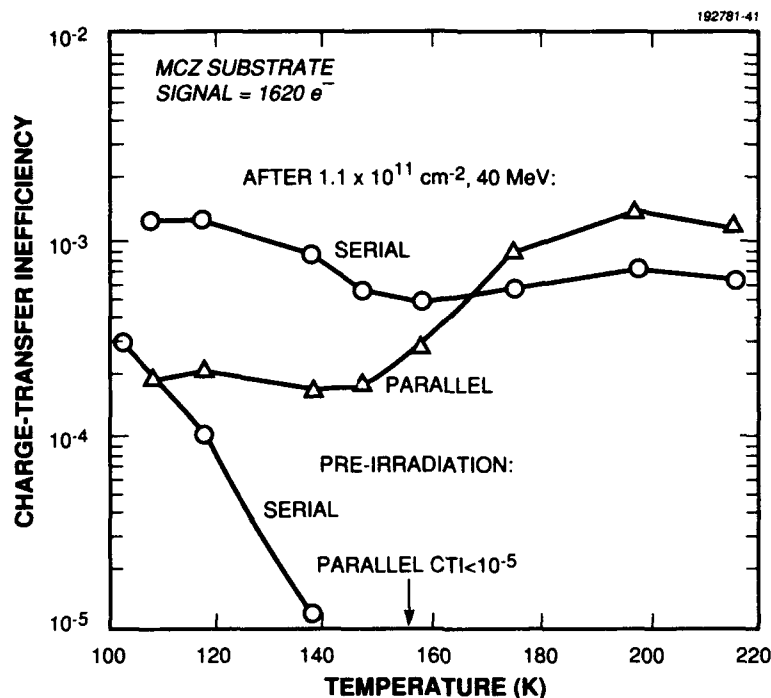
Figure 6-7. Measured charge-transfer inefficiency vs temperature in a 420 × 420-pixel frame-transfer imager using x-rays from an Fe^{55} source. Data are shown both before and after irradiation with 40-MeV protons at a dose of $1.1 × 10^{11}$ cm^{-2}.

The results in Figure 6-7 indicate that 150 K is approximately the optimum temperature of operation for an irradiated device. The worst-case charge loss at this temperature is 17% in the parallel arrays (840 transfers) and 20% for the serial register (420 transfers), a level that would still be considered useful for space surveillance applications. A perspective on the dose that produced this degradation is provided by the case of the space-based visible (SBV) experiment that will be placed on the MSX satellite in a 900-km polar orbit. The CCD focal plane environment of the SBV test has shielding equivalent to ~ 20 mm of Al. The proton spectrum penetrating this shielding can be calculated using a code such as Severn Associates' Space Radiation. Then, by using a program developed previously [9], the number of vacancies generated by this multienergy spectrum can be compared with that generated by the monoenergetic irradiation from the Harvard cyclotron. The result indicates that the displacement damage in the device described here would be the same as would accumulate during 43 years in orbit.

B. E. Burke
M. J. Cooper
J. A. Gregory

REFERENCES

1. K. Fukushima, S. Miyake, and T. Ito, *IEEE Trans. Syst. Man Cybern.* **SMC-13**, 826 (1983).

2. A. M. Chiang and B. E. Burke, *IEEE J. Solid-State Circuits* **SC-18**, 745 (1983).

3. A. M. Chiang, *IEEE J. Solid-State Circuits* **25**, 1510 (1990).

4. Solid State Research Report, Lincoln Laboratory, MIT, 1990:3, p. 53.

5. Solid State Research Report, Lincoln Laboratory, MIT, 1990:4, p. 61.

6. B. E. Burke, R. W. Mountain, D. C. Harrison, M. W. Bautz, J. P. Doty, G. R. Ricker, and P. J. Daniels, *IEEE Trans. Electron Devices* **38**, 1069 (1991).

7. Solid State Research Report, Lincoln Laboratory, MIT, 1991:3, p. 39.

8. Solid State Research Report, Lincoln Laboratory, MIT, 1990:2, p. 51.

9. Solid State Research Report, Lincoln Laboratory, MIT, 1991:2, p. 49.

7. ANALOG DEVICE TECHNOLOGY

7.1 STRIPLINE RESONATOR MEASUREMENTS OF SURFACE IMPEDANCE VS RF MAGNETIC FIELD IN YBa$_2$Cu$_3$O$_{7-x}$ THIN FILMS

Almost all of the reported measurements of surface resistance R_s of the high-temperature super-conductor YBa$_2$Cu$_3$O$_{7-x}$ have been carried out at low power and thus at low values of RF magnetic field H_{rf}. It has been known for some time that measured values of R_s are dependent on the level of microwave power used. This has been noted in measurements of Q or R_s in stripline resonators [1] as well as in cavities [2]. Much higher values of H_{rf} can be reached at a given input power level in stripline structures than in the usual cavity geometries because the narrow transmission line concentrates the current and leads to a higher current density. Until now, however, measurements of R_s as a function of the input power in stripline structures have not been quantitative, because the current distribution in the stripline could not be calculated accurately and hence the exact value of the magnetic field was not known.

Recently completed calculations of current distributions in stripline transmission line structures [3] enable quantitative measurements of R_s vs the peak H_{rf}. Using the results of the calculations and the measured values of Q and resonant frequency of a stripline resonator, we report here the microwave-frequency surface impedance Z_s as a function of frequency from 1.5 to 20 GHz, the temperature from 4 K to the transition temperature ($T_c \approx 90$ K), and the H_{rf} from 0 to 250 Oe.

The measurements have been carried out on a number of YBa$_2$Cu$_3$O$_{7-x}$ films deposited in situ by single-target off-axis magnetron sputtering. The results show that the best epitaxial films exhibit weak dependence of R_s on H_{rf}, while lower-quality films, believed to be composed of grains connected by weak links, demonstrate an R_s that increases in linear proportion to H_{rf}. The films exhibit a critical field beyond which the R_s increases sharply, indicating that a substantial fraction of the line has become normal. In the best films the field at which this happens is ~ 250 Oe, which is higher than any previously reported value.

Our measurements of Z_s were made using the stripline resonator described in detail previously [1]. The films for the resonators were fabricated by an off-axis magnetron sputtering process also reported earlier [4]. We concentrate on results from two sets of films deposited at 760°C but with different sputtering targets. These have the best microwave properties among our films, including those reported previously [1],[5]. The substrate used was LaAlO$_3$.

The method of calculation of the current distribution, elaborated in [3], is based on a modification of the method of Weeks et al. [6] and incorporates a complex conductivity to describe the superconductor and ensure that the London equations as well as the Maxwell equations are satisfied. The calculations can be applied to any number of coupled superconductors in a quasi-TEM system. Figure 7-1 shows the results for the geometry of the stripline used in these experiments, a penetration depth $\lambda = 0.16$ μm, and a film thickness $t = 0.30$ μm. From such current distributions the inductance L per unit length of the stripline was calculated as a function of λ.
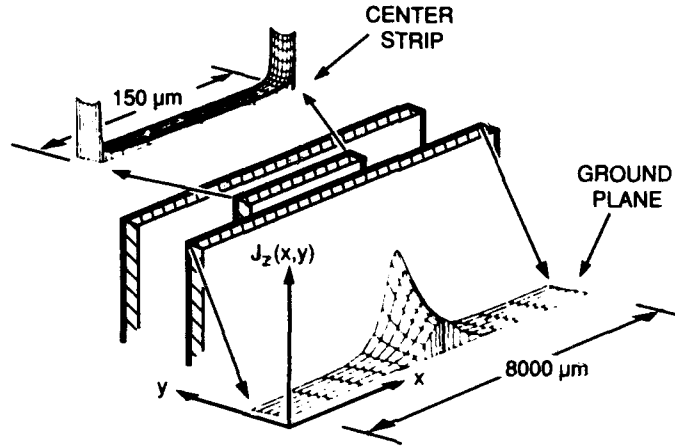
Figure 7-1. Calculated current distributions for the center conductor and ground plane of the resonator used in the experiments. Note the different distance scales for the center strip and the ground plane. The calculations are for $\lambda = 0.16$ μm and film thickness $t = 0.30$ μm.

We next determined the penetration depth at $T = 0$ K, λ_0, by measuring the temperature dependence of the fundamental resonant frequency of the resonator and then fitting a model of the temperature dependence of λ to the measured data. This procedure used $L(\lambda)$, the calculated inductance as a function of λ. Figure 7-2 shows the measured resonant frequency vs temperature for one of the resonators (sample 2 in Table 7-1). The solid line is a least-squares fit to the data using the temperature dependence calculated from the two-fluid model in which

$$\lambda(T) = \frac{\lambda_0}{\sqrt{1 - \left(\dfrac{T}{T_c}\right)^4}} \quad , \tag{7.1}$$

where T_c is the transition temperature. Both λ_0 and T_c were employed as free parameters. The best fit was obtained with $\lambda_0 = 0.167$ μm and $T_c = 86.4$ K, the latter being consistent with the measured resistive transition. As others have observed [7], the fit shows some deviation from the two-fluid model.

Table 7-1 shows the value of λ_0 obtained for a sputtered niobium film, which was used as a check of the method, as well as the values for the two sputtered $YBa_2Cu_3O_{7-x}$ films. The value of λ_0 for sputtered niobium agrees with previously reported values.

To obtain the R_s of the films at each value of T for low RF fields, we used λ_0, determined as described above, and $\lambda(T)$ given in Equation (7.1) to calculate L as a function of T. The measured Q and calculated L were used to obtain the resistance R per unit length of the stripline as a function of T from the expression $Q = \omega L/R$. Then, R and λ were used to find the real part σ_1 of the complex conductivity, and R_s was obtained from $R_s = \omega^2 \mu^2 \sigma_1 \lambda^3/2$, where μ is the permeability. This process for calculating R, σ_1, and R_s was then repeated at each of the overtone frequencies of the resonator up to 20 GHz.

68

192781-43
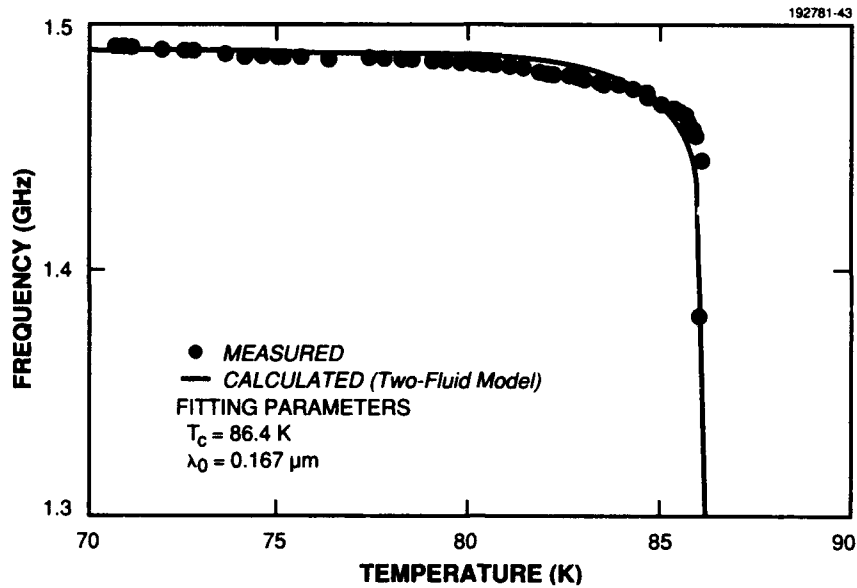
Figure 7-2. *Measured and calculated values of resonant frequency of the fundamental mode of the resonator vs temperature for $YBa_2Cu_3O_{7-x}$ film (sample 1 in Table 7-1). The calculated values use the two-fluid model. The best fit is obtained with $\lambda(0) = 0.167$ μm and $T_c = 86.4$ K.*

TABLE 7-1

Parameters of $YBa_2Cu_3O_{7-x}$ and Sputtered Niobium Films

Film	Sample	λ_0 (μm)	T_c (K)
$YBa_2Cu_3O_{7-x}$	1	0.22	90
$YBa_2Cu_3O_{7-x}$	2	0.167	86.4
Sputtered niobium	—	0.070	9.2

Figure 7-3 shows, for the best of the sputtered films (sample 1 in Table 7-1), the frequency dependence of the R_s at low RF fields, with temperature as a parameter. Each point in the plot corresponds to one of the modes of the resonator. The R_s increases very nearly as the square of frequency. Many models of losses in superconductors, including the two-fluid model [8] and others based on losses in intergrain weak links [9], predict an f^2 dependence of R_s, so this result is expected and does not differentiate among the various proposed models of RF losses. Figure 7-4 shows the temperature dependence of the low-field resistance for the three lowest modes. It should be pointed out that the values of R_s shown in Figures 7-3 and 7-4 are among the best reported [10],[11]. We also believe that these values are the lowest that have been realized for a patterned film.
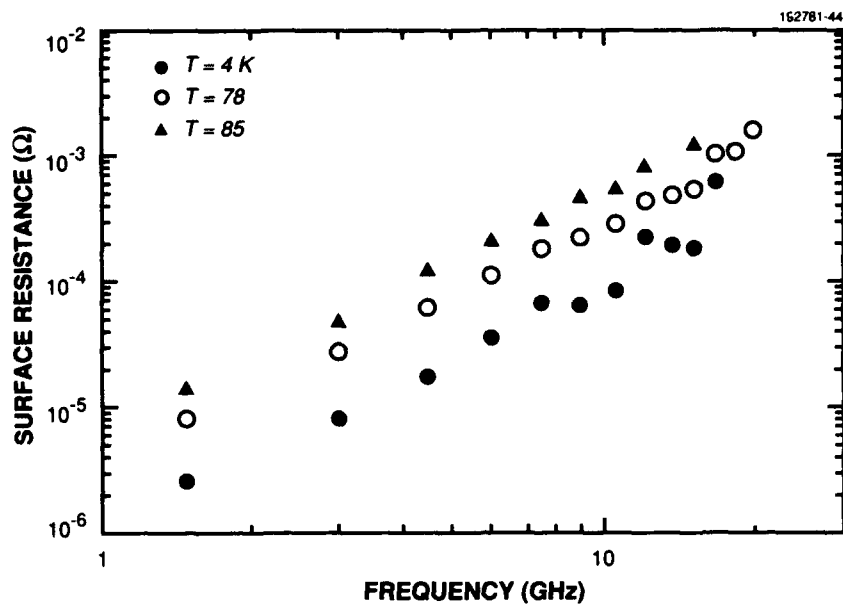
Figure 7-3. Surface resistance vs frequency for three different temperatures as indicated. These results are for the best sputtered film (sample 1 in Table 1).
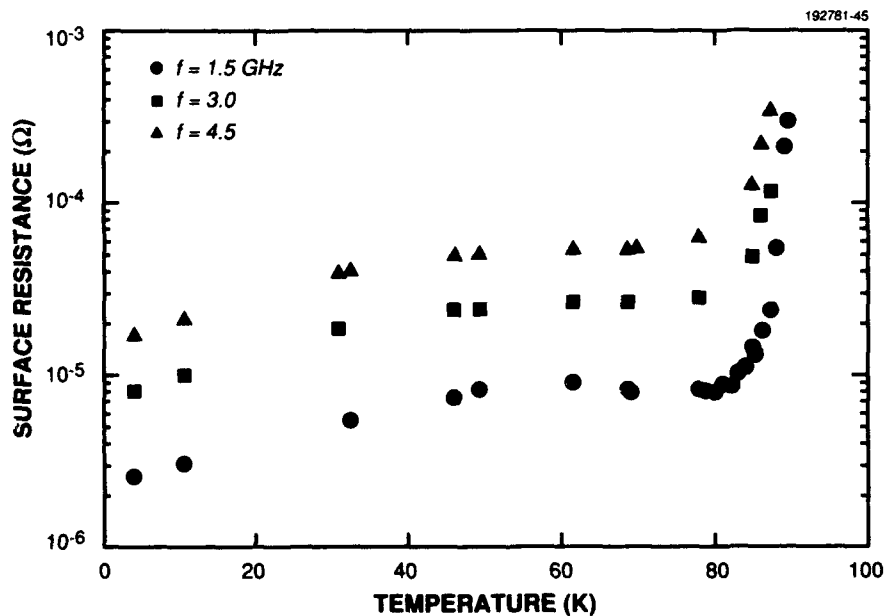
Figure 7-4. Surface resistance vs temperature for the first three modes of the best sputtered film (sample 1 in Table 1). The frequency of each mode is given.

70

To obtain $R_s(H_{rf})$, we measured the Q and insertion loss IL of the resonator as a function of the incident RF power P. We then calculated the total RF current in the stripline at the peaks of the standing-wave maxima at resonance, I_p, by [1]

$$\left| I_p \right| = \sqrt{\frac{r_v(1 - r_v)4Q_cP}{n\pi Z_0}} \quad , \tag{7.2}$$

where r_v is the voltage insertion ratio related to IL by $IL = -20 \log r_v$, Q. is the unloaded Q of the conductor given by $Q_c = Q/(1 - 10^{-IL/20})$, n is the resonant mode number, and Z_0 is the characteristic impedance of the line. From the I_p and the calculated current distribution, the peak RF magnetic field at the edges of the center strip, $H_{rf,p}$, was calculated. As can be seen from the current distribution in Figure 7-1, the field distribution is peaked near the edges like the current density. The value of $R_s(H_{rf,p})$ at each input power level was obtained by the same procedure that was used for the low-field R_s. The small dependence of λ on $H_{rf,p}$ was neglected.

The dependence of R_s on $H_{rf,p}$ for the two $YBa_2Cu_3O_{7-x}$ samples is shown in Figure 7-5. We give data for $f = 1.5$ GHz at 4 and 77 K for both films. At 4 K, for both films, the input power was increased until a sharp rise in R_s was measured. Beyond this point it is meaningless to report values of R_s because
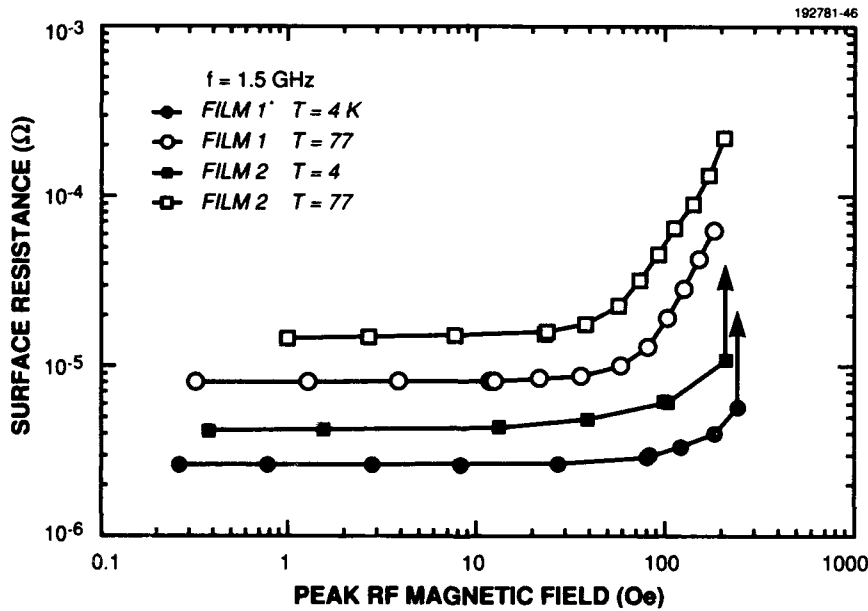
Figure 7-5. Surface resistance vs $H_{rf,p}$, the peak field at the edges of the center strip, for the two $YBa_2Cu_3O_{7-x}$ films (samples 1 and 2 in Table 1) at 4 and 77 K. The frequency in all cases is 1.5 GHz.

the resonance curve is severely distorted and Q is ill defined. At 77 K no sharp increase in R_s was noted up to the maximum available input power of 1 W. At 4 K and below the apparent critical field, and at 77 K over the entire range, the R_s is well approximated by a quadratic dependence on H_{rf},

$$R_s = R_{s0} + \alpha H_{rf}^2 \quad , \tag{7.3}$$

where R_{s0} is the surface resistance at very low fields. In postannealed films and in films sputtered at lower sample temperatures, which we have previously reported [1], we observed a linear dependence of R_s on H_{rf},

$$R_s = R_{s0} + \beta H_{rf} \quad . \tag{7.4}$$

A linear dependence of R_s on H_{rf} has been associated with magnetic flux penetration in Josephson-junction-type weak links between grain boundaries [12]. Such dependence is a signature of a film that is not single crystal in nature but is composed of a collection of weakly connected grains. A quadratic dependence of R_s on H_{rf}, on the other hand, is consistent with the Ginzburg-Landau (GL) theory [8], in which the magnetic field breaks superconducting pairs, increases the proportion of normal electrons, and thus increases the R_s. The weak quadratic field dependence at low temperature of these newer films sputtered at higher substrate temperatures indicates that the films are relatively free of weak links and more nearly single crystal in nature than the earlier examples.

Although the GL theory predicts a quadratic field dependence of R_s, it does not explain our results, since at low temperature the R_s is dominated by the residual resistance caused by extrinsic effects and thus any pair-breaking effects described by the GL theory will be masked entirely by the residual resistance [12]. The GL theory leads to a larger fractional change in R_s at low temperatures, where most electrons are already paired and any breaking of pairs will have a proportionally larger effect, than at 77 K where there are already many unpaired electrons. Our results show the opposite trend, a larger fractional change in R_s at 77 K than at 4 K.

It may be that different mechanisms govern the dependence of R_s on H_{rf} at low and high temperatures. For example, if the sudden increase in R_s observed at high fields at low temperature were due to flux

TABLE 7-2

Best Values of R_s for a $YBa_2Cu_3O_{7-x}$ Film*

Frequency (GHz)	Temperature (K)	R_s (Ω)
1.5	4	2.6×10^{-6}
1.5	77	8.3×10^{-6}
10	4	8.5×10^{-5}
10	77	2.0×10^{-4}
* Sample 1 in Table 7-1.		

becoming unpinned at the edges of the stripline, then at higher temperatures one would expect a more gradual effect (as we have observed) because the flux is not as strongly pinned and thermal activation is sufficient to depin the flux at more moderate values of the fields [13]. Other experiments [2],[12] have observed a quadratic dependence at low fields, but in all cases known to us the quadratic dependence changes over to a linear dependence at very low fields.

The values of R_s reported here at low RF magnetic field are comparable to the best reported in the literature. Table 7-2 summarizes the results at 1.5 and 10 GHz at 4 and 77 K for our best film (sample 1 in Table 7-1). These results are as low as any values previously reported for a patterned film. Our experimental observations of $Z_s(H_{rf})$ in $YBa_2Cu_3O_{7-x}$ epitaxial thin films are as follows: (1) at 4 K, R_s and λ are very weakly dependent on H_{rf} up to a critical field value, beyond which R_s increases very rapidly; and (2) at 77 K, there is a larger quadratic increase of R_s and λ with H_{rf}, with the fractional change in R_s being much larger than in λ. We did not see the saturation of the R_s vs H_{rf} (R_s becoming independent of field) as others have observed [2], even though our measurements were at higher RF magnetic fields.

D. E. Oates   D. M. Sheen*
A. C. Anderson S. M. Ali*

7.2 GENERIC FABRICATION PROCESS FOR MIXED ANALOG/DIGITAL SUPERCONDUCTIVE INTEGRATED CIRCUITS

The development of a fabrication process for low-temperature superconductive integrated circuits that include both analog and digital components has been substantially completed. Our goal has been to design a generic process that is applicable, without modification, to a broad range of analog and digital circuit designs. Such a process has several requirements. First, it must support a wide range of electrical components. Second, the characteristics of these components must be well documented and tightly controlled over a wafer and from wafer to wafer. Third, the component yield must be high enough to make reasonably large circuits. Finally, the process should employ computer design aids to assist the designer and to assure the accuracy of designs.

Our process supports the following electrical structures: Josephson junctions, capacitors with high Q and high specific capacitance, and resistors. Optionally, a thick low-loss deposited dielectric may be incorporated for forming compact 50-Ω delay lines that can achieve delays in the tens of nanoseconds. The process also supports three superconducting niobium layers. These three layers can be used for a number of purposes. They can serve as wiring layers providing excellent flexibility in terms of crossovers. In addition, one layer, usually the one closest to the substrate, can function as a ground plane to reduce the electromagnetic coupling between circuits and to decrease the parasitic series inductance of interconnect wiring. Finally, the three layers can be used to make transformers. The process provides direct contact—that is, with no Josephson junctions in series—between metal layers, making it possible for any layer to carry large currents.

---

*Department of Electrical Engineering and Computer Science and Research Laboratory of Electronics, Massachusetts Institute of Technology.

In our process development we have addressed the uniformity and reproducibility of electrical and physical parameters (the requirements tend to be particularly stringent for analog circuits) as well as the component reliability and yield. The robustness of dielectric layers has been a special concern. In almost all areas the insulation between metal layers constitutes a dual dielectric. The main dielectric is silicon monoxide. The secondary dielectrics are tantalum oxide, which also serves as the capacitor dielectric, and niobium oxide, which also isolates the individual Josephson junctions.

The process is supported by three types of computerized layout verification tools: design rule checking (DRC), electrical rule checking (ERC), and layout vs schematic (LVS) confirmation. Our process definition file includes specifications for single layers (e.g., minimum width and spacing) and for pairs of layers (e.g., minimum spacing, overlap, and enclosure). We have also developed software to enable the designer to see at any stage a cross section of any portion of the circuit layout. These cross-sectional views show the layer deposition, lift-off, and etching during the fabrication process and are indispensable in the verification of the mask layout.

A cross-sectional view of a typical superconductive integrated circuit is shown in Figure 7-6. The circuit fabrication requires ten masking layers and six thin-film deposition steps. The first film to be deposited is the ground-plane metallization, which is a niobium/tantalum bilayer. The tantalum on the top can be converted to tantalum pentoxide using an anodization process. This tantalum pentoxide layer serves as a high-quality dielectric for capacitors, which have a specific capacitance of 4 nF/mm^2 and a Q of ~ 1500 at frequencies between 30 and 90 MHz. It also serves as the first insulator in the dual dielectric between the ground-plane metallization and the niobium/aluminum-oxide/niobium trilayer, which is sandwiched between the ground-plane metallization and the upper niobium wiring layer. Individual Josephson junctions formed in the trilayer are isolated from each other by converting the top niobium layer into niobium pentoxide by an anodization step very similar to that which defines the capacitor dielectric. The Josephson current density J_c can be chosen within the range of 500 to 1000 A/cm^2. Direct contacts to the base-electrode of these junctions are accomplished by etching off the niobium counterelectrode and the aluminum oxide tunnel barrier in an area that had previously been fabricated as a Josephson junction. The maximum supercurrent density that can be carried by these contacts is > 10^6 A/cm^2. All niobium layers are patterned by dry etching in either CF_4 or CCl_2F_2. Evaporated silicon monoxide is used as the primary interlayer dielectric and is patterned either by lift-off or by dry etching using CHF_3.

Figure 7-7 shows the current-voltage characteristic of a string of 50 Josephson junctions connected in series. The junction quality denoted by the figure of merit V_m is quite good, as is the uniformity of the critical currents, with the total spread in the measured critical currents, $\Delta I_c/I_c$, being less than 4%. Other measurements show that the junction critical currents for 5-μm-square junctions across a 2-in. substrate have a standard deviation of 4%. The maximum-to-minimum spread of these critical currents is ~ 12%. Although junction yield on an individual wafer sometimes approaches 98%, occasionally a wafer may have a yield as low as 30%. We are currently investigating the junction failure mechanisms and hope to increase the yield in the near future.
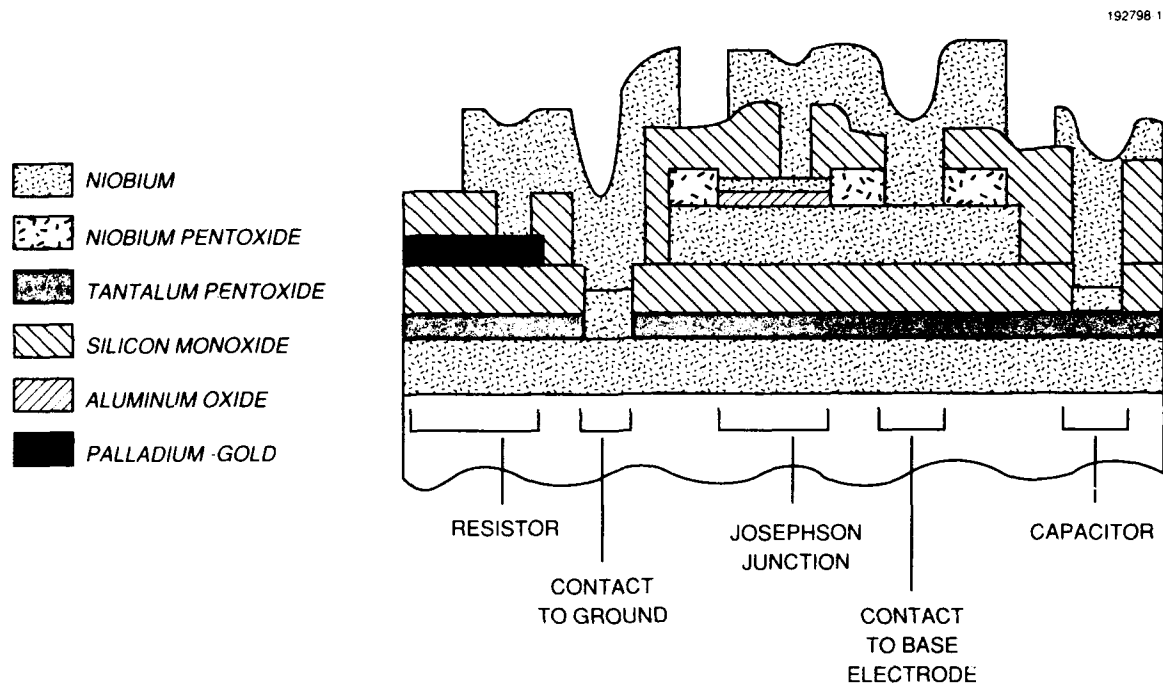
Figure 7-6. Cross-sectional view of a typical superconductive integrated circuit.

NIOBIUM

NIOBIUM PENTOXIDE

TANTALUM PENTOXIDE

SILICON MONOXIDE

ALUMINUM OXIDE

PALLADIUM-GOLD

RESISTOR

CONTACT
TO GROUND

JOSEPHSON
JUNCTION

CONTACT
TO BASE
ELECTRODE

CAPACITOR

200 µA

50 mV

Figure 7-7. Current-voltage characteristic of 50 series-connected Josephson junctions for $J_c \approx 1000$ A/cm^2. $V_m \approx 60$ mV, $\Delta I_c / I_c < 4\%$, and a junction size of 5×5 mm square.

Resistors are defined by lift-off of 120 nm of a palladium-gold alloy. The results are also quite uniform, with a sheet resistance of 3.5 Ω/square and a standard deviation of < 3% across an entire wafer. This uniformity is critical to realizing a high yield of digital integrated circuits and to achieving a high accuracy of the analog components. Finally, as an option, thick (~ 5 μm) films of evaporated silicon monoxide can be utilized as the dielectric for compact transmission lines. Experiments have shown that for frequencies up to 18 GHz, the loss tangent of this material is < 10^{-4}. This allows for the fabrication of 32-ns delay lines in an area 2 cm square.

J. B. Green	E. M. Macedo, Jr.
J. P. Sage	R. G. Minnick
R. R. Boisvert	D. K. Downs
J. M. Denneno	S. A. Ladd
G. L. Fitch	T. J. Weir

REFERENCES

1. D. E. Oates, Alfredo C. Anderson, and P. M. Mankiewich, *J. Superconduct.* **3**, 251 (1990).

2. A. M. Portis, D. W. Cooke, E. R. Gray, P. N. Arendt, C. L. Bohn, J. R. Delayen, C. T. Roche, H. Hein, N. Klein, G. Müller, S. Orbach, and H. Piel, *Appl. Phys. Lett.* **58**, 307 (1991); D. W. Cooke, P. N. Arendt, E. R. Gray, and A. M. Portis, to be published.

3. D. M. Sheen, S. M. Ali, D. E Oates, R. S. Withers, and J. A. Kong, *IEEE Trans. Appl. Superconduct.* **1**, 108 (1991).

4. A. C. Westerheim, L. S. Yu-Jahnes, and Alfredo C. Anderson, *IEEE Trans. Magn.* **27**, 1001 (1991).

5. D. E. Oates and Alfredo C. Anderson, *IEEE Trans. Magn.* **27**, 867 (1991).

6. W. T. Weeks, L. L. Wu, M. F. McAllister, and A. Singh, *IBM J. Res. Dev.* **23**, 652 (1979).

7. S. M. Anglage, B. W. Langly, H. J. Snortland, E. B. Eom, T. H. Geballe, and M. R. Beasley, *J. Superconduct.* **3**, 251 (1990).

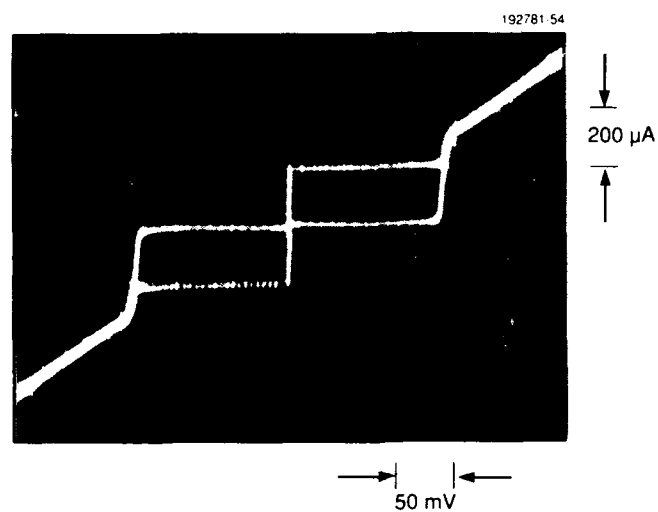8. T. Van Duzer and C. W. Turner, *Principles of Superconductive Devices and Circuits* (Elsevier, New York, 1981).

9. T. L. Hylton and M. R. Beasley, *Phys. Rev. B* **13**, 9042 (1989).

10. N. Newman, K. Char, S. M. Garrison, R. W. Barton, R. C. Taber, C. B. Eom, T. H. Geballe, and D. Wilkens, *Appl. Phys. Lett.* **57**, 520 (1990).

11. N. Klein, G. Müller, H. Piel, B. Roas, L. Schultz, U. Klein, and M. Peiniger, *Appl. Phys. Lett.* **54**, 757 (1989).

12. J. Halbritter, *J. Appl. Phys.* **68**, 6315 (1990).

13. T. Orlando, private communication.

REPORT DOCUMENTATION PAGE

1. AGENCY USE ONLY (Leave blank)	2. REPORT DATE 15 November 1991	3. REPORT TYPE AND DATES COVERED Quarterly Technical Report, 1 August – 31 October 1991

4. TITLE AND SUBTITLE

Solid State Research

5. FUNDING NUMBERS

C — F19628-90-C-0002
PE — 63250F
PR — 221

6. AUTHOR(S)

Alan L. McWhorter

7. PERFORMING ORGANIZATION NAME(S) AND ADDRESS(ES)

Lincoln Laboratory, MIT
P.O. Box 73
Lexington, MA 02173-9108

8. PERFORMING ORGANIZATION REPORT NUMBER

1991:4

9. SPONSORING/MONITORING AGENCY NAME(S) AND ADDRESS(ES)

Air Force Systems Command, USAF
Andrews AFB
Washington, DC 20334-5000

10. SPONSORING/MONITORING AGENCY REPORT NUMBER

ESD-TR-91-260

11. SUPPLEMENTARY NOTES

None

12a. DISTRIBUTION/AVAILABILITY STATEMENT

Approved for public release; distribution is unlimited.

12b. DISTRIBUTION CODE

13. ABSTRACT (Maximum 200 words)

This report covers in detail the research work of the Solid State Division at Lincoln Laboratory for the period 1 August through 31 October 1991. The topics covered are Electrooptical Devices, Quantum Electronics, Materials Research, Submicrometer Technology, High Speed Electronics, Microelectronics, and Analog Device Technology. Funding is provided primarily by the Air Force, with additional support provided by the Army, DARPA, Navy, SDIO, NASA, and DOE.

14. SUBJECT TERMS

electrooptical devices	high speed electronics	optical interferometers	diamond cold cathodes
quantum electronics	microelectronics	nonlinear optics	charge-coupled devices
materials research	analog device technology	laser modulation	superconductive filters
submicrometer technology	lasers	ultraviolet lithography	

15. NUMBER OF PAGES

104

16. PRICE CODE

17. SECURITY CLASSIFICATION OF REPORT Unclassified	18. SECURITY CLASSIFICATION OF THIS PAGE SAR	19. SECURITY CLASSIFICATION OF ABSTRACT SAR	20. LIMITATION OF ABSTRACT SAR